UNIVERSITAT POLITÈCNICA DE CATALUNYA BARCELONATECH

High-peak-power mid-infrared OPCPAs for extreme nonlinear photonics

Ugaitz Elu Etxano

High-peak-power mid-infrared OPCPAs for extreme nonlinear photonics

by

Ugaitz Elu Etxano

Thesis Advisor:
Prof. Dr. Jens Biegert

A thesis submitted in fulfillment of the requirements
for the degree of Doctor of Philosophy
in the
Attoscience and Ultrafast Optics

ICFO – Institut de Ciències Fotòniques
UPC – Universitat Politècnica de Catalunya

Barcelona, February 2022

Thesis committee:

1) Prof. Dr. Majid Ebrahim-Zadeh (The Institute of Photonic Sciences, Spain)
2) Dr. Olivier Chalus (Thales LAS France SAS, France)
3) Dr. David Novoa (University of the Basque Country, Spain)

Abstract

In the last decades, intense carrier-envelope-phase-stable (CEP-stable) and near-single-cycle, coherent mid-infrared sources have become charming for a variety of applications in physics, chemistry and biology. In particular, those mid-infrared sources are of tremendous interest for broadband spectroscopic applications, solid-state light-matter studies, strong-field physics research, and attosecond science. On the one hand, broadband coherent mid-infrared sources are capable of replacing time-consuming scanning techniques to classify organic structures or detect hazardous chemical compounds. On the other hand, high-energy, CEP-stable, near single-cycle mid-infrared sources are key in strong-field physics and attoscience due to the wavelength scaling nature of strong-field electron re-collision-based processes.

Nevertheless, implementing such mid-infrared sources remains challenging due to the lack of user-friendly temporal, spectral and spatial characterisation instruments, efficient and affordable reflection/transmission coatings, and commercially accessible low-loss dispersion compensation optics. Moreover, the absence of suitable laser gain materials reinforces nonlinear down conversion and amplification methods.

One approach to overcoming the current limitations and developing intense ultrafast mid-infrared systems is to use a commercially available high-power near-infrared laser combined with second-order nonlinear processes. The optical parametric amplification (OPA) process is a three-wave mixing nonlinear process that transfers energy from an intense short-wavelength pump-pulse to a weak longer-wavelength seed-pulse. In addition, in the optical parametric chirped-pulse amplification (OPCPA) process, the seed pulses are deliberately stretched beforehand for amplification and then re-compressed. OPCPA can be essential to avoid damage to the nonlinear crystals or tailor the amplified spectrum. OPCPAs are also used when femtosecond pulses are required to be amplified using picosecond pump

lasers. As a result, OPCPA systems offer novel opportunities for producing high-intensity, broadband mid-infrared femtosecond pulses.

The Attosecond and Ultrafast Optics (AUO) group at the Institute of Photonic Sciences (ICFO) in Barcelona has been pioneering the development of mid-infrared OPCPA systems since 2007. Since then, the group has gained valuable experience in mid-infrared beam propagation, optical alignment, detection and characterisation, coating development etc. This thesis uses all the previously acquired knowledge and presents our efforts to push further the performance of two mid-infrared systems developed by the AUO group.

The 160 kHz high-power mid-infrared OPCPA system is designed to overcome the existing limitations in the high-repetition-rate mid-infrared regime. Here is demonstrated the generation of unique 3.2 μm pulses with a single-cycle duration and delivering up to 3.9 GW of peak power. The combination of the CEP stability with the single-cycle duration and the high energies demonstrated makes this system suitable to produce ultrafast radiation in the kilo-electron-volt X-ray regime.

Furthermore, a newly developed mid-infrared nonlinear crystal named BGGSe is proposed for efficient broadband infrared radiation generation. The ultra-broadband source is produced using the BGGSe crystal combined with a unique anti-resonant-reflection photonic crystal fibre (ARR-PCF) that enables tailoring the compression of our 3.2 μm pulses at 160 kHz. Using the BGGSe crystal and the ARR-PCF, we demonstrate the generation of coherent light expanding up to seven octaves, from UV to the THz regime.

The second mid-infrared system presented in this thesis is the high-energy 7 μm OPCPA operated at a 100 Hz repetition rate and developed to generate hard X-rays in the multi-kilo-electron-volt regime. The development of this second OPCPA centred at 7 μm overcomes the considerable challenges in the mid-infrared regime. This thesis demonstrates the amplification of those mid-infrared pulses to 750 μJ and the efficient back-compression to 188 fs.

Moreover, high harmonic generation in solids driven by 7 μm pulses at 100 Hz and 3.2 μm pulses at 160 kHz has been exploited for solid-state studies using the developed OPCPA systems. This thesis highlights the results achieved in the high-temperature YBCO superconductor, where exponential enhancement of harmonics is demonstrated below the critical temperature.

All these demonstrations make those systems a key-enabling technology for the next generation of studies in solid-state physics, extreme nonlinear photonics, strong-field physics and coherent X-ray science.

Acknowledgements

First of all, I would like to thank my supervisor, Prof. Dr. Jens Biegert, for giving me the opportunity to perform my doctoral studies in his research group. It has been an enriching experience with many opportunities to improve professionally in my career. His support and advice guided me through the exciting world of ultrafast physics, pushing me to learn more about physics and, in particular, ultrafast extreme nonlinear photonics. I also would like to thank him for the excellent conferences he organised in Benasque, which included ski lectures.

I would also like to give a special thanks to Mathias Baudisch and Daniel Sanchez, from whom I learnt almost everything about high-power, high-energy mid-infrared systems. They shared with me all their experience in mid-infrared OPCPAs, nonlinear optics, and the small necessary tricks to align such intricate laser systems. I should not forget all the gimmicks shared to approach daily base challenges such as water-cooling chiller failures.

I would also like to thank Tobias Steinle, Luke Maidment, Lenard Vamos, Hugo Pires, and Themis Sidiropolous for all the physics discussions. And a special thanks to Iker Leon for all of his assistance both inside and outside the lab, particularly in the preparation of the largest cheesecakes, chocolate cakes, and, of course, Basque cakes. And of course, thanks to Barbara Buades for all the fantastic sailing boat trips, and Blanca Belsa and Tobias Steinle for all the organised social "Pepito" reunions.

Furthermore, thanks to all my colleagues who worked with me in the AUO group: Nicola di Palo, Aurelien Sanchez, Julius Huijts, Maurizio Reduzzi, Kasra Amini, Adam Summers, Daniel Rivas, Benjamin Wolter, Noslen Suárez, Idoia Martí, Michele Sclafani, Michael Pullen, Stefano Severino, Florian Haberstroh, Michael Enders, Igor Tyulnev, Xinyao Liu, Ying-Hao Chien and Hung-Wei Sun.

I would also like to thank all the collaborators. Thanks to the group of Prof. Dr. Philip Russell in MPL for providing their amazing ARR-PCFs and the group

of Prof. Dr. Scott A. Diddams from NIST in Boulder, where we carried out an exciting project with unforgettable experiences. Thanks to the groups of Prof. Dr. Javier Garcia de Abajo and Prof. Dr. Maciej Lewenstein from ICFO for their theoretical support. I would also like to thank Dr Peter G. Schunemann from BAE, Dr Valentin Petrov from MBI, and Dr Anna Palau from ICMAB-CSIC for providing unique samples, crucial for the results achieved in this thesis. Moreover, I would like to thank Francesco Tani, David Novoa, Felix Köttig and Michael H. Frosz for their valuable help and insights in using their ARR-PCF successfully. Furthermore, I would like to thank Javier Garcia de Abajo for his time and lectures on high harmonics in solids.

Last but not least, I would like to thank the Castefagang: Pamina, Kavitha, Álvaro, José, Eduardo, Caterina, Iker, Hugo..., and my flatmates Sandra and Julio for all of the fantastic plans and dinners they put together. Also, for all the shared trips, even if in half of them we got lost.

Finally, a special thank you goes to my parents and my brother for all their unconditional help and support.

Publications

- Jordi Alcalà, Utso Bhattacharya, Jens Biegert, Marcelo Ciappina, **Ugaitz Elu**, Tobias Graß, Piotr T. Grochowski, Maciej Lewenstein, Anna Palau, Themistoklis P. H. Sidiropoulos, Tobias Steinle, Igor Tyulnev *High harmonic spectroscopy of quantum phase transitions in a high-T_c superconductor,* arXiv preprint arXiv:2201.09515, 2022.

- **Ugaitz Elu**, Luke Maidment, Lenard Vamos, Francesco Tani, David Novoa, Michael H. Frosz, Valeriy Badikov, Dmitrii Badikov, Valentin Petrov, Philip St. J. Russell and Jens Biegert *Extreme temporal compression of ultra-broadband mid-infrared pulses,* Light Filaments: Structures, Challenges and Applications, 2022: 103.

- **Ugaitz Elu**, Luke Maidment, Lenard Vamos, Francesco Tani, David Novoa, Michael H. Frosz, Valeriy Badikov, Dmitrii Badikov, Valentin Petrov, Philip St. J. Russell and Jens Biegert *Seven-octave high-brightness and carrier-envelope-phase-stable light source,* Nature Photonics **15**, 2021.

- **Ugaitz Elu**, Luke Maidment, Lenard Vamos, Tobias Steinle, Florian Haberstroh, Valentin Petrov, Valeriy Badikov, Dmitrii Badikov and Jens Biegert *Few-cycle mid-infrared pulses from $BaGa_2GeSe_6$,* Optics Letters **45**, 2020.

- Abijith S Kowligy, Henry Timmers, Alexander J. Lind, **Ugaitz Elu**, Flavio C. Cruz, Peter G. Schunemann, Jens Biegert and Scott A. Diddams *Infrared electric field sampled frequency comb spectroscopy,* Science Advances **5**, 2019.

- **Ugaitz Elu**, Tobias Steinle, Daniel Sánchez, Luke Maidment, Kevin Zawilski, Peter G. Schunemann, Uwe D. Zeitner, Christophe Simon-Boisson, and Jens Biegert *Table-top high-energy 7μm OPCPA and 260mJ Ho:YLF pump laser,* Optics Letters **44**, 2019.

- **Ugaitz Elu**, Matthias Baudisch, Hugo Pires, Francesco Tani, Michael H. Frosz, Felix Köttig, Alexey Ermolov and Philip St.J. Russell and Jens Biegert

High average power and single-cycle pulses from a mid-IR optical parametric chirped pulse amplifier, Optica **4**, 2017.

Contents

Chapter 1

Introduction

The demonstration of light amplification by stimulated emission of radiation (LASER) in 1960 [1] enabled a new era for the generation of coherent electromagnetic radiation. High intensities can be achieved, in compact schemes, using the radiation generated from a laser, enabling the modification of the optical properties of matter. In 1961, it was demonstrated for the first time the second harmonic generation (SHG) by focusing down the radiation generated from a ruby laser into a crystalline quartz sample [2]. Since those discoveries, bright lasers combined with nonlinear effects have been used to tailor light and develop compact systems emitting coherent, high-intensity, ultrashort pulses [3, 4]. These systems are used for the study of different time-dependent physical processes.

To extend the capabilities of lasers, extreme nonlinear processes, such as high harmonic generation (HHG) in noble gases, are widely used to transform infrared radiation into coherent X-ray radiation [5, 6]. The cut-off energy of the generated HHG scales linearly with the peak intensity of the laser field and quadratically with the centre wavelength. Thus, intense ultrashort infrared pulses are required to exploit these processes successfully. Moreover, close to plasma generation peak intensities (10^{15} W/cm^2) are required to trigger the electron recollision processes that enable the HHG process, thus limiting the scalability in photon energy by increasing the laser peak intensity. HHG driven by lasers centred at a longer wavelength is a plausible option for the generation of coherent ultrashort X-ray radiation with higher photon energies up to the kilo-electron-volt radiation regime [7, 8]. Moreover, it is demonstrated the generation of reproducible attosecond-X-ray pulses, using carrier-envelope phase (CEP) stable, single-cycle (see equation 3.2.1 for details), infrared pulses [7–10].

The dynamics of different physical processes can be studied using ultrashort pulses at different photon energy ranges. Figure 1.1 shows a summary of a few different physical processes that can be investigated using electromagnetic radiation at different photon energies. Hard X-rays (above 5 keV) are typically used amongst other purposes for X-ray crystallography [11], medical radiography [12, 13] and airport security. Photons in the range of hundreds to kilo-electron-volts are used for X-ray diffraction or absorption spectroscopy. The specific K-edge transitions in essential elements for nature such as oxygen (543 eV), nitrogen (410 eV), carbon (284 eV) can be studied [14, 15] in this regime. Ultraviolet radiation can be used to trigger chemical reactions or retrieve band structures using the angle-resolved photoemission in solids. Visible light is typically used for charge transfer studies or to study intraband transitions or excitons. Coherent infrared radiation is an exciting frequency regime showing a wide range of capabilities for solid-state physical studies such as intraband and interband transitions, plasmons, phonons, charge density waves and superconducting materials [16]. The fingerprint absorption region in the mid-infrared regime is used for studying fundamental biological molecules such as proteins and carbohydrates in live cells in a non-invasive manner [17, 18]. Moreover, THz radiation allows studies of low-frequency excitations like molecular rotations, crystal lattice vibrations, and free carrier acceleration.

Thus, combining infrared and THz radiation with visible and ultraviolet light opens a new area for 2D spectroscopy [19]. This technique enables the study of temporal dynamics from sub-femtosecond to picosecond durations of electron-electron, electron-phonon and phonon-phonon interactions. Therefore, the interest in developing compact tabletop sources covering all the above frequency regimes has risen in the last decades. These systems have shown unique capabilities to enable a wide range of studies with unprecedented temporal and spatial resolutions, from quantum light-matter interactions to molecular and chemical dynamics.

This thesis aims to redesign and develop high-energy, bright, CEP-stable, mid-infrared sources for quantum light-matter interaction studies with 2D spectroscopy technic as well as for kilo-electron-volt range radiation generation. For this purpose, frontends based on commercially available lasers are used. The pulses from the frontend laser are then modified via a combination of different nonlinear processes to generate high-energy pulses in the mid-infrared regime to fulfil the requirements described above.

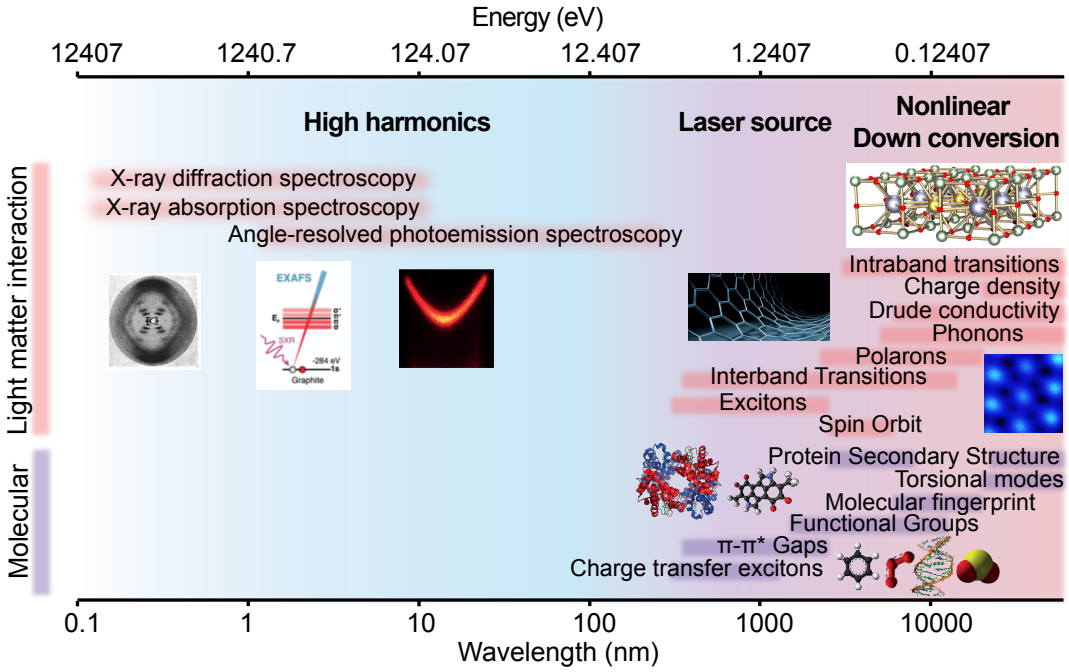

FIGURE 1.1: Possible applications of ultrafast coherent radiation from hard-X-rays to THz for solid-state, condensed phase and molecular phase research.

1.1 High-energy lasers sources

High-energy lasers are typically concluded by an oscillator frontend, where the mode-locked pulses are generated, and a few amplifier stages for the generation of high-energy pulses. Moreover, in the amplifier stages, a well-known technique called chirped pulse amplification (CPA) is typically used to achieve high energies by avoiding possible damages in the active materials [20]. In a CPA system, the pulses are beforehand chirped and later introduced in the amplification stage. After the final amplification stage, the pulses are back compressed.

The most advanced high power lasers are in the visible and near-infrared regime due to the availability of known solid-state materials absorbing and emitting in this regime. One of the most known laser is based on Nd: $Y_3Al_5O_{12}$ (Nd: YAG), which was demonstrated in 1964 [21], just four years after the first laser was built. Nowadays, high-energy lasers are available based on Nd: YAG [22]. Still, due to the higher absorption and emission efficiency of the Nd: YVO4 (Nd: Vanadate) active material, this can be a better choice for high power lasers. Moreover, the emission bandwidth of Nd: YVO_4 is more extensive and thus, enables shorter pulse duration [23]. The typical emission frequency of Nd: YAG and Nd: YVO_4 is at 1064 nm, but a nonlinear crystal (BBO, KTP) can be introduced for frequency doubling into 532 nm. Unfortunately, the emission bandwidth of Nd: YAG and

Nd: YVO_4 is not enough to generate directly single-cycle pulses at 1064 nm and use the laser for straight strong-field physics studies or HHG.

Titanium sapphire (Ti: Sa) lasers were invented in 1982 and widely studied in the following years [24]. They absorb efficiently around 530 nm and have an ultra-broad emission bandwidth from 650 nm up to 1100 nm. Thus, it is typical to use frequency-doubled, continuous wave (CW), Nd: YAG or Nd: YVO_4 high power lasers to pump the Ti: Sa crystal and achieve the generation of high energy femtosecond pulses around 800 nm. Unlike Neodymium based lasers, Ti: Sa lasers can deliver mJ level few-cycle pulses making them suitable to drive directly strong-field processes such us HHG for coherent extreme ultraviolet pulse generation [25].

Ti: Sa lasers are also used for wavelength scaling up to 2 μm via OPA process, enabling the generation of higher photon energies via HHG. The high-energy CEP-stable 2 μm pulses driven by Ti: Sa lasers are demonstrated to be key enabling tools for coherent attosecond Soft-X-ray generation up to 500 eV via HHG process in noble gases [9, 10]. Unfortunately, limitations on phase-matching, quantum efficiency and transmission window of the nonlinear crystals make it unpractical to use Ti: Sa lasers for amplification of broadband high-energy mid-infrared pulses. Instead, Neodymium based lasers emitting around 1 μm are used for amplification of mid-infrared pulses up to 4 μm [26]. As Neodymium based lasers are limited to picosecond time scales, optical parametric chirped pulse amplification (OPCPA) is used to amplify femtosecond mid-infrared pulses efficiently. Similarly to CPA systems, the pulses are firstly stretched in time and then amplified using high energy picosecond lasers.

In the last decades, new technology has been developed based on thin disc lasers. Ytterbium (Yb) is an active material that is very suitable for thin disc lasers. Thin disc lasers based on Yb emit around 1 μm, are able to generate pulse energies higher than Nd based lasers and achieve sub-2-picosecond pulse durations [27]. As the pulse duration of the pump is shorter, driving the OPCPA process for mid-infrared amplification with those lasers make the stretching and compression of the mid-infrared pulses simpler and the OPCPA system more efficient.

During the last years, the development of a new high-energy solid-state laser based on Holmium (Ho), emitting around 2 μm and with picosecond duration, has been demonstrated [28–30]. These new solid-state lasers have shown the capability to drive OPCPAs with unprecedented energies for the amplification of mid-infrared pulses above 5 μm wavelengths [29, 31, 32].

One of the limiting parameters for the generation of high-energy lasers is the repetition rate. Laser cost, space and heat (e.g. thermal lensing, misalignments) management limits the pump power of the solid-state laser, thus limiting the highest repetition rates that are aspired to be used. On the other hand, at low repetition rates where heat is not the main problem, fluence or peak intensity induced damages on mirrors, gratings and crystals, limit the maximum energy achieved in the laser system. Thus, different repetition rates can be chosen depending on the physical process to be studied.

In Figure 1.2 are shown some of the high-energy lasers over the world, with different repetition rates from 10 Hz up to 160 kHz, which are based on Titanium sapphire [32], Neodymium [22, 23], Ytterbium [27] and Holmium [28–30]. With a star in Figure 1.2, the lasers developed in the Attosecond and ultrafast group at ICFO are shown. These lasers are used to amplify pulses at short-infrared and mid-infrared regimes via OPA and OPCPA processes. Among other results, this thesis discusses the development of the 2052 nm, 100 Hz, high energy Ho: YLF laser and the use of the Nd: YVO_4 high repetition rate laser for the development of high power single-cycle 3.2 μm pulses.

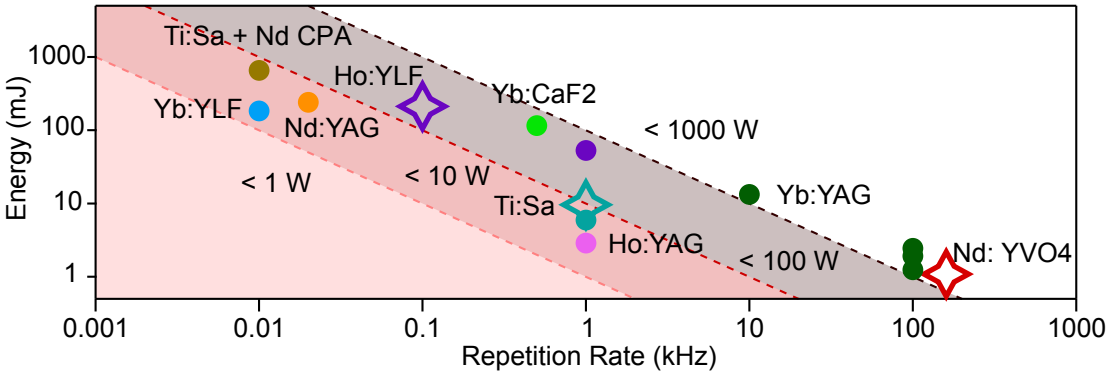

FIGURE 1.2: Some of the high energy laser sources over the world based on active materials such us Titanium sapphire, Neodymium, Ytterbium and Holmium. With a star lasers developed in the Attosecond and ultrafast group at ICFO are represented.

1.2 Mid-Infrared sources

Mid-infrared coherent radiation can be generated by using materials that absorb in the near-infrared regime and emit in the mid-infrared regime or by using nonlinear processes for frequency down-conversion. The number of active materials available that emit in the mid-infrared regime is limited to the lead salt compounds

like PbSnTe and PbxEuSeTe or quantum cascade lasers [33]. Recently, the development of broadband femtosecond radiation has been achieved using Cr: ZnSe and Cr: ZnS around 2.5 μm [34–36]. Unfortunately, the lack of broadband efficient laser materials emitting above 3 μm makes it unpractical to use those options for ultrashort high-energy mid-infrared pulse generation. Thus, the development of systems emitting high-energy broadband pulses above 3 μm still relies on nonlinear processes.

Frequency down-conversion via nonlinear differential frequency generation (DFG) by mixing two near-infrared pulses at different frequencies are typically used for mid-infrared pulse generation. Mid-infrared pulses with direct passive CEP stability can be achieved when both input pulses have a fixed phase relation. When both input pulses are generated from the same oscillator, those pulses show random phase offset but equal pulse to pulse temporal phase fluctuations. During the DFG process, the phase fluctuations are cancelled, achieving constant phase offset.

White-light generation via filamentation in bulk and its side spectral component amplification via OPA can be used to generate the second pulse for seeding the DFG process while maintaining the phase relation [32]. Close to damage threshold peak intensities and plasma generation are needed to generate a white-light continuum, inducing possible power and phase instabilities into the generated pulses. For higher stability, two-colour sources based on Erbium (Er), Thulium (Tm) or Ho doped fibre oscillators can be used for DFG [26, 37–39]. Moreover, ultra-broadband CEP-stable mid-infrared pulses can be achieved via intrapulse DFG (IP-DFG) using a single broadband pulse for frequency down-conversion in a nonlinear crystal [40, 41].

The availability of nonlinear crystals transmitting in the mid-infrared regime that can be pumped with visible or near-infrared lasers is also limited. They generally show high refractive index values and, thus, tremendous losses due to Fresnel reflections. A proper anti-resonant (AR) coating transmitting efficiently near-infrared and mid-infrared pulses is required to keep the efficiencies as high as possible.

In Figure 1.3 are shown the transmission window and the figure of merit of some of the most efficient known mid-infrared nonlinear crystals used for nonlinear down conversion. The figure of merit is calculated like d_{eff}^2/n^3 and is used to predict the conversion efficiency of the down-conversion nonlinear process [42, 43], see the Γ factor in equation 2.2.30 for details. The figure of merit, the transmission

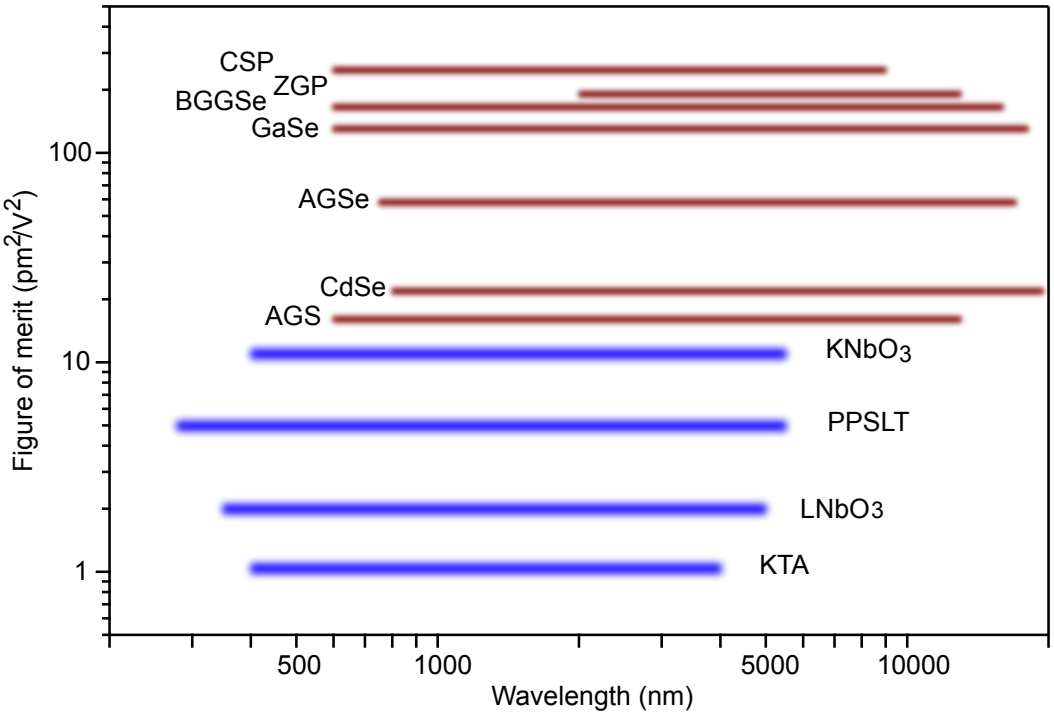

FIGURE 1.3: The figure of merit of some of the most efficient nonlinear crystals in the mid-infrared regime transmitting above (red) and below (green) 5 μm.

window, and the nonlinear crystal's damage threshold are necessary to consider to find the most promising nonlinear crystal. The physical processes that can induce damage are few and depend strongly on the pump wavelength, pulse duration and fluence. Due to the difficulty of quantifying the damage threshold of the crystals, this information is not shown in Figure 1.3.

Bulk and surface damages [44, 45] can be induced by different processes such as peak intensity, peak-power, thermal refractive index changes, transient absorption, multiphoton absorption and self-focusing. Some of these effects become crucial to consider when the nonlinear refractive index values are enormous or when the pump is close to a transmission edge. Thus, the availability and choice of nonlinear crystals in the mid-infrared regime above 4 μm become challenging, and a proper choice is needed to avoid damage and achieve a relatively high generation/amplification efficiency.

For the generation or amplification of pulses in the mid-infrared regime up to 4 μm high power/energy 1 μm lasers are typically used. Some of the most promising nonlinear crystals used for this purpose are Lithium niobate ($LNbO_3$), Potassium niobate ($KNbO_3$), Potassium Titanyl Arsenate (KTA) and periodically poled

stoichiometric lithium tantalate (PPSLT) [46–49]. Magnesium oxide doped periodically poled lithium niobate (MgO: PPLN) is typically used instead of $LNbO_3$ thanks to the advantages of quasi-phase-matching (QPM). In general, PPLN shows narrower phase-matching bandwidth than bulk KTA, $LNbO_3$ or $KNbO_3$. Thus aperiodically poled lithium niobate (aPPLN) samples are used instead, where the phase-matched frequency is tuned over the propagation length through the crystal to achieve broader phase-matching.

However, scaling the pulse energy in $LNbO_3$ is limited by the low damage threshold due to the green radiation-induced infrared transient absorption, which in $LNbO_3$ shows relaxation times of several seconds [50–52] when the crystal is pumped with 1 μm pulses. This effect can be enhanced when using PPLN or aPPLN if the phase-matching for SHG of 1 μm pulses is favourable due to the QPM periodicity. PPSLT has a larger damage threshold in the range of 80–180 $GWcm^2$ and a higher nonlinear coefficient, but the crystal apertures are limited, which at the same time limits the maximum pump energies that can be used. KTA can be pumped with high power/energy 1 μm lasers enabling higher amplification factors, but the phase-matching bandwidth is limited. $KNbO_3$ with a damage threshold of up to 14.4 $GWcm^2$ and a high nonlinear coefficient for broadband mid-infrared generation shows a balanced compromise between the phase-matching acceptance bandwidth and amplification efficiency.

Above 4 μm the most commonly used nonlinear crystals are non-oxide semiconductors such as CdSe, GaSe, $AgGaSe_2$ (AGSe), $AgGaS_2$ (AGS), ZGP and $CdSiP_2$ (CSP) [38, 53–55].

CdSe exhibits non-zero effective nonlinearity only for type 2 phase matching, which restricts its applications. GaSe faces limitations for cleaving polishing and coating. It can only be cleaved along the 001 plane (z-cut), it is extremely soft, and the AR coating is not available. AGSe is chemically unstable in air, and as well as AGS has one of the lowest damage thresholds. CSP has one of the highest figures of merit values, but non-collinear geometry is required to achieve broadband phase-matching, introducing spatial chirp to the generated mid-infrared beam. ZGP, with one of the highest figures of merit and damage thresholds, is typically used for mid-infrared pulse amplification. Unfortunately, the main limitation of ZGP is the narrow transmission window which extends from 2 μm to 13 μm. Thus pump lasers emitting above 2 μm are needed.

The newly developed $BaGa_2GeSe_6$ (BGGSe) shows a high figure of merit; it can be AR coated and is expected to show similar damage thresholds as ZGP [42]. Moreover, BGGSe provides a flat dispersion relation through the mid-infrared regime, implying ultra-broadband phase-matching properties. Moreover, its transmission window expands from the visible regime up to ~20 μm.

1.3 Thesis outline and state of the art of mid-infrared lasers

Figure 1.4 shows some of the state-of-the-art solid-state lasers emitting in 1-2 μm regime and the mid-infrared systems developed by employing those systems via OPCPA and IP-DFG process. Nd and Yb based solid-state lasers are used to pump OPCPAs for amplification of mid-infrared lasers between 3 μm and 4 μm [56–58]. IP-DFG is typically generated using femtosecond 1.55 μm pulses from an Er/Yb fibre amplifier. Still, efficiencies are higher when pumping the IP-DFG nonlinear crystal at a longer wavelength for frequency down-conversion [40]. Thus, Tm doped fibre amplifiers at 1.965 μm can be used to drive the same process more efficiently [39]. Moreover, Ho based solid-state lasers are used to pump OPCPA systems above 4 μm to achieve high-energy femtosecond mid-infrared radiation [28–31].

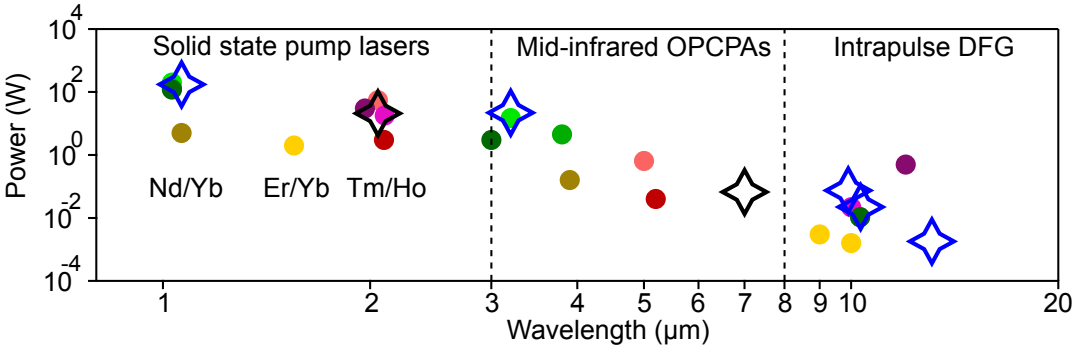

FIGURE 1.4: Summary of few ultrashort femtosecond mid-infrared sources generated via OPCPA and IP-DFG, driven via high power solid-state lasers. Each colour determines a different laser system. With a star are shown the laser systems develop in the Attosecond and ultrafast group at ICFO.

This thesis focuses on developing and improving mid-infrared OPCPAs to achieve high-energy, bright ultrashort femtosecond radiation. For this purpose, Nd: Vanadate and Ho: YLF solid-state pump lasers have been used to develop two different OPCPA systems.

For this purpose, an enumerable amount of nonlinear processes are used in this thesis, from second and third-order processes to high-order effects. Chapter 2 enumerates the most important effects and presents an analytic study of those nonlinear processes.

In Chapter 3 is shown how a Nd: Vanadate laser delivering 1.1 mJ energy pulses at 160 kHz and 10 ps pulse duration is used to pump the high-power 3.2 μm OPCPA achieving record powers at 3.2 μm with single-cycle duration. In this chapter is shown the demonstration of 3.2 μm pulse compression to the single-cycle regime using a unique anti-resonant-reflection photonic crystal fibre (ARR-PCF) developed in collaboration with the group of Prof. Philip Russell in Max Planck Institute for the Science of Light (MPL). Thanks to the properties of this ARR-PCF, the 3.2 μm pulses can be tailored easily in time and bandwidth, enabling efficient and controllable IP-DFG. By using the newly developed BGGSe mid-infrared nonlinear crystal, an ultrabroad and efficient IP-DFG is demonstrated. The huge transmission window of the crystal enables the generation of a spectrum expanding up to 7 octaves, from UV to the THz regime. This chapter also demonstrates that this kind of ARR-PCFs can be used for dispersive-wave (DW) generation in the UV regime pumped by high-power femtosecond mid-infrared pulses.

Chapter 4 presents the development and upgrade of the femtosecond 7 μm high-energy OPCPA. In this chapter is studied the generation of 7 μm pulses via DFG using GaSe and the newly developed BGGSe crystal. Moreover, here is shown the upgrade of the Ho: YLF multi-pass booster amplifier delivering record energies of 260 mJ in a compact tabletop design and the development of the 7 μm OPCPA system pumped by the high-energy Ho: YLF laser. The amplification of the 7 μm pulses up to 750 μJ and compression down to 188 fs using around 10% of the available energy of the Ho: YLF pump laser is demonstrated. Moreover, making use of the femtosecond high-energy 7 μm pulses, solid harmonics are shown in ZnSe achieving all the even and odd harmonics from 2^{nd} to 12^{th}.

In the last decades, different explanations and simulations about high harmonics in solids (HHS) have been studied. One of the conclusions all the studies agree on is that the HHS depends on the crystallographic structure. Thus, information on the band structure is expected to be encrypted on the measured HHS spectrum. In Chapter 5 is presented the HHS process in one of the most known high critical-temperature (Tc) superconductor $YBa_2Cu_3O_7$ (YBCO), driven by the 3.2 μm few-cycle pulses. This chapter shows how the HHS generation changes when the temperature of the YBCO is tuned from room temperature to 80 K with

$T_c = 90$ K. A significant exponential enhancement is measured when the sample reaches the superconducting state.

Finally, in Chapter 6 the summary and future outlook of the presented results are discussed.

Chapter 2

Background in ultrashort pulse propagation

A well-studied use of linear and nonlinear effects is required to generate intense, near-single-cycle, CEP-stable pulses. For instance, a high-energy pulse can be compressed/stretched in time due to nonlinear effects during the propagation in a medium. Moreover, proper dispersion management is required to maintain an ultrashort pulse compressed.

Thus, this chapter aims to describe the basics of linear and nonlinear ultrashort pulse propagation exploited in different experiments mentioned in the following chapters. Moreover, this chapter explains various numerical models vitals for precisely estimating the ultrashort pulse propagation in a nonlinear media.

The propagation of an electromagnetic wave in a medium is described combining the Maxwell–Faraday equation $\nabla \times \mathbf{E} = -\frac{\partial \mathbf{B}}{\partial t}$ with the Ampère–Maxwell law $\nabla \times \mathbf{H} = \mathbf{J} + \frac{\partial \mathbf{D}}{\partial t}$, for $\mathbf{D} = \varepsilon_0 \mathbf{E} + \mathbf{P}$ and $\mathbf{H} = \frac{1}{\mu_0}\mathbf{B}$ as follows:

$$\nabla^2 \mathbf{E}(\mathbf{r}, t) - \mu_0 \varepsilon_0 \frac{\partial^2 \mathbf{E}(\mathbf{r}, t)}{\partial t^2} = \mu_0 \frac{\partial^2 \mathbf{P}(\mathbf{r}, t)}{\partial t^2} + \mu_0 \frac{\partial \mathbf{J}(\mathbf{r}, t)}{\partial t} \tag{2.1}$$

where μ_0 and ε_0 are the permeability and permittivity in vacuum, respectively, $\mathbf{E}(\mathbf{r}, t)$ is the electric field, $\mathbf{P}(\mathbf{r}, t)$ the induced polarisation and $\mathbf{J}(\mathbf{r}, t)$ is the electron-current density. The polarisation term is responsible for dispersion, divergence and nonlinear processes. The electron-current density describes the electron dynamics such as plasma generation, multiphoton absorption and high harmonic generation.

Moreover, when those intense ultrashort pulses are focused into a nonlinear medium, effects such as sum-frequency, difference frequency, parametric amplification, spectral broadening [59, 60] or generation of hundreds of harmonics can be produced [5, 6].

The induced polarisation $\mathbf{P}$ can be expressed in nonlinear optics as a power series of the electric field $\mathbf{E}$ in the time domain. Generally, this expression is written in the frequency domain by assuming an instantaneous response of the medium to the electromagnetic wave:

$$\mathbf{P}(\omega) = \varepsilon_0 \left[\chi^{(1)}\mathbf{E}(\omega) + \chi^{(2)}\mathbf{E}^2(\omega) + \chi^{(3)}\mathbf{E}^3(\omega) + ...\right] \tag{2.2}$$

where $\chi^{(1)}$ is the first-order electric susceptibility, which describes the linear polarisation response of the material. Assuming a uniaxial crystal (or in 1D), the refractive index can be calculated directly from the linear susceptibility through $n = \sqrt{1+\chi^{(1)}}$. The quantities $\chi^{(2)}$ and $\chi^{(3)}$ are known as the second and third-order nonlinear optical susceptibilities, respectively. The estimation of the values for $\chi^{(2)}$ and $\chi^{(3)}$ is widely discussed in the Nonlinear Optics book from Robert W. Boyd [59].

The solutions for the equation 2.1 can be written in plane waves for $\mathbf{E}(\mathbf{r},t)$, $\mathbf{P}(\mathbf{r},t)$ and $\mathbf{J}(\mathbf{r},t)$ as follows:

$$\mathbf{E}(\mathbf{r},t) = \mathbf{E}_0(\mathbf{r},t)\, e^{i(\mathbf{k}_0\mathbf{r}-\omega_0 t)} \tag{2.3}$$

$$\mathbf{P}(\mathbf{r},t) = \mathbf{P}_0(\mathbf{r},t)\, e^{i(\mathbf{k}_0\mathbf{r}-\omega_0 t)} \tag{2.4}$$

$$\mathbf{J}(\mathbf{r},t) = \mathbf{J}_0(\mathbf{r},t)\, e^{i(\mathbf{k}_0\mathbf{r}-\omega_0 t)} \tag{2.5}$$

where $\mathbf{k}_0$ and ω_0 are the wave-vector and centre frequency in vacuum, respectively. Moreover, by assuming that the envelope of the electromagnetic pulse varies slowly in time compared to the field oscillations and replacing the plane waves in equation 2.1, the wave-equation is reduced from a second-order differential equation in space and time to a first-order differential equation. This approximation is known as the slowly varying envelope approximation (SVEA) $|\nabla^2\mathbf{E}_0| \ll |\mathbf{k}_0\nabla\mathbf{E}_0|$ and $\left|\frac{\partial^2\mathbf{E}_0}{\partial t^2}\right| \ll \left|\omega_0\frac{\partial\mathbf{E}_0}{\partial t}\right|$. By assuming an electromagnetic wave propagating in z with

radial symmetry in the transversal directions (x and y), and computing a Fourier transformation from the time domain to the frequency domain, the wave-equation can be simplified to a first-order differential equation:

$$\frac{\partial E_0(\omega,z)}{\partial z} - ik_z E_0(\omega,z) = i\frac{\omega^2}{2\varepsilon_0 k_z c^2} P_0(\omega,z) - \frac{\omega}{2\varepsilon_0 k_z c^2} J_0(\omega,z) \tag{2.6}$$

where k_z is the wave-vector in the propagation direction. The above equation is also known as the unidirectional pulse propagation equation (UPPE), which is widely used for pulse propagation in nonlinear media for the study of second and third-order processes as well as higher-order nonlinear processes [61].

While effects that involve absorption and emission of light need extra care due to the strong heating effects of the medium, nonlinear effects are typically carried in the spectral regime where the medium highly transmits the involved pulses. Thus, the equations presented in this chapter are deduced by neglecting the absorption effects in the medium.

2.1 Linear propagation of ultrashort pulses

The linear propagation of ultrashort pulses can be described from the general wave equation in the frequency domain and simplified by taking $J = 0$ and $P(\omega,z) = \varepsilon_0 \chi^{(1)}(\omega) E(\omega,z)$:

$$\frac{\partial^2 E(\omega,z)}{\partial z^2} = -\frac{n^2\omega^2}{c^2} E(\omega,z) \tag{2.1.1}$$

being the plane wave solution the following expression:

$$E(\omega,z) = E_0(\omega,0)\, e^{-ik(\omega)z} \tag{2.1.2}$$

where $k(\omega) = k_0 n(\omega) = \frac{n(\omega)}{c}$ is the wave-vector in the medium defined by the refractive index $n(\omega)$. When broadband ultrashort pulses are propagated in a medium, the frequency dependency of the refractive index, as well as its higher-order terms, need to be taken into account. Thus, a Taylor expansion of the wave-vector is performed to calculate group velocity and dispersion effects on the broadband ultrashort pulses [60].

$$k(\omega) = k(\omega_0) + \frac{\mathrm{d}k(\omega)}{\mathrm{d}\omega}\Big|_{\omega_0}(\omega-\omega_0) + \frac{1}{2}\frac{\mathrm{d}^2k(\omega)}{\mathrm{d}\omega^2}\Big|_{\omega_0}(\omega-\omega_0)^2 + \frac{1}{6}\frac{\mathrm{d}^3k(\omega)}{\mathrm{d}\omega^3}\Big|_{\omega_0}(\omega-\omega_0)^3 + \ldots \quad (2.1.3)$$

where ω_0 is the centre frequency of the ultrashort pulse. While the first derivative introduces a phase shift in the electric field, the second derivative defines the group velocity (GV) in the medium at ω_0. If the GV varies significantly inside the same pulse, there will be frequencies delayed in time at the end of the propagation, and the pulse will be stretched. This variation is defined by the third derivative, also known as the group velocity dispersion (GVD).

The compression or stretching effect that a medium with a length L produces in an ultrashort pulse can be estimated typically by calculating the group delay dispersion (GDD) and third-order dispersion (TOD) induced by the medium.

$$GDD(\omega_0, L) = \frac{\mathrm{d}^2k(\omega)}{\mathrm{d}\omega^2}\Big|_{\omega_0}L = \left(2\frac{\mathrm{d}n(\omega)}{\mathrm{d}\omega}\Big|_{\omega_0} + \omega_0\frac{\mathrm{d}^2n(\omega)}{\mathrm{d}\omega^2}\Big|_{\omega_0}\right)\frac{L}{c} \quad (2.1.4)$$

$$TOD(\omega_0, L) = \frac{\mathrm{d}^3k(\omega)}{\mathrm{d}\omega^3}\Big|_{\omega_0}L = \left(3\frac{\mathrm{d}^2n(\omega)}{\mathrm{d}\omega^2}\Big|_{\omega_0} + \omega_0\frac{\mathrm{d}^3n(\omega)}{\mathrm{d}\omega^3}\Big|_{\omega_0}\right)\frac{L}{c} \quad (2.1.5)$$

where $n(\omega)$ is the refractive index in the frequency domain. Implementing the quantities of GDD and TOD in the equation 2.1.2 we can predict with reasonable accuracy how the envelope of an ultrashort pulse varies at the output of a bulk medium with thickness L:

$$E(\omega, L) \propto E_0(\omega, 0)\, e^{-i\left(\frac{1}{2}GDD(\omega-\omega_0)^2 + \frac{1}{6}TOD(\omega-\omega_0)^3\right)} \quad (2.1.6)$$

While in the near-infrared and mid-infrared frequencies, materials with positive and negative GDD can be found, all the bulk materials introduce positive TOD. Thus, while GDD can be compensated using different materials, TOD keeps accumulating. Consequently, TOD can become the limiting factor for pulse compression for ultrabroad pulses when GDD is minimised.

2.2 Second-order nonlinear processes

Sum frequency generation (SFG), DFG, OPA and electro-optic effect are known to be second-order nonlinear effects that can be achieved by focusing intense light into a non-centrosymmetric medium. Second-order nonlinear processes involve the interaction of three electromagnetic waves in a nonlinear medium.

$$\frac{\partial^2 E(\omega_i, z)}{\partial z^2} = -\frac{n_i^2 \omega_i^2}{c^2} E(\omega_i, z) - \mu_0 \omega_i^2 P^{(2)}(\omega_i, z) \tag{2.2.1}$$

where the second-order nonlinear polarisation can be described as follows:

$$P^{(2)}(\omega_k, z) = \varepsilon_0 \chi^{(2)} E(\omega_i, z) E(\omega_j, z) \tag{2.2.2}$$

where $\omega_k = |\omega_i \pm \omega_j|$. Thus, if we drive the nonlinear crystal with two waves with frequencies ω_1 and ω_2, the polarisation induced can be described as follows:

$$P^{(2)}(\omega_3) = P^{(2)}(\omega_1 + \omega_2) + P^{(2)}(\omega_1 - \omega_2) \tag{2.2.3}$$

where the first term describes the SFG effect, and the second term represents the DFG process. SHG and electro-optic rectification processes will be generated, if $\omega_1 = \omega_2$, instead of SFG and DFG, respectively. While all these processes are allowed in the nonlinear interaction, generally, the crystal orientation determines the enhanced process due to phase-matching conditions.

In SFG, the input pulses' frequencies and phases are summed to generate the third wave. On the other hand, in DFG, the frequencies and the phases are subtracted. If the two input pulses for the DFG are generated from the same oscillator, then the phases of the input pulses are expected to be related ($\phi_1(t) = \phi_2(t) + \delta$). Thus, the time dependency of the generated pulse phase will be cancelled in the DFG process, and it will be CEP-stable [66]:

$$\phi_3(t) = \phi_1(t) - \phi_2(t) = \delta \tag{2.2.4}$$

where δ is just a constant phase produced due to the difference in propagation length of the two input pulses. The phase of the DFG field will not vary from pulse to pulse, achieving a frequency comb with no offset $\Delta\phi(t) = 0$ [60, 62].

Moreover, the CEP value δ, can be easily altered by slightly changing the path lengths between the two input pulses in the DFG process. Unfortunately, any mechanical or optical AC perturbation that destroys the reproducibility of the pulse train can introduce degradation of the frequency comb or CEP stability.

Any second nonlinear process assuming the SVEA can be calculated using the following three-wave coupled equations:

$$\frac{\mathrm{d}E\left(\omega_1,z\right)}{\mathrm{d}z}=2i\frac{\omega_1 d_{eff}}{n_1 c}E_2^*\left(\omega_2,z\right)E_3\left(\omega_3,z\right)e^{i\Delta kz} \tag{2.2.5}$$

$$\frac{\mathrm{d}E\left(\omega_2,z\right)}{\mathrm{d}z}=2i\frac{\omega_2 d_{eff}}{n_2 c}E_1^*\left(\omega_1,z\right)E_3\left(\omega_3,z\right)e^{i\Delta kz} \tag{2.2.6}$$

$$\frac{\mathrm{d}E\left(\omega_3,z\right)}{\mathrm{d}z}=2i\frac{\omega_3 d_{eff}}{n_3 c}E_1\left(\omega_1,z\right)E_2\left(\omega_2,z\right)e^{-i\Delta kz} \tag{2.2.7}$$

where $\Delta k=k_3-k_1-k_2$ and $d_{eff}=\frac{\chi^{(2)}}{2}$.

2.2.1 Sum frequency generation

The first-order differential equations described above can be easily solved by assuming that driving fields do not vary during the propagation $E_{1,2}\left(z\right)=E_{1,2}\left(0\right)$, also called the undepleted approximation. This approximation is valid when the nonlinear process is generated gently, without achieving the nonlinear process's saturation and when the material's dispersion can be neglected. Then, the three first-order differential equations are reduced to the following single first-order differential equation:

$$\frac{\mathrm{d}E\left(\omega_3,z\right)}{\mathrm{d}z}=2i\frac{\omega_3 d_{eff}}{n_3 c}E_1\left(\omega_1,0\right)E_2\left(\omega_2,0\right)e^{-i\Delta kz} \tag{2.2.8}$$

and the solution for a propagation length of L can be written as:

$$E\left(\omega_3,L\right)=2\frac{\omega_3 d_{eff}}{n_3 c}E_1\left(\omega_1,0\right)E_2\left(\omega_2,0\right)\left(\frac{e^{-i\Delta kL}-1}{\Delta k}\right) \tag{2.2.9}$$

where $\left(\frac{e^{-i\Delta kL}-1}{\Delta k}\right) = -L\,\mathrm{sinc}\left(\frac{\Delta kL}{2}\right)e^{i\frac{\Delta kL}{2}}$. If we neglect the frequency-dependency of Δk and d_{eff}, the total electric-field radiated can be obtained by calculating the convolution of $E_1(\omega_1, 0)$ and $E_2(\omega_2, 0)$ as follows:

$$E_{SFG}(\omega, L) = 2\frac{\omega d_{eff}}{nc}\left(\frac{e^{-i\Delta kL}-1}{\Delta k}\right)\int_{\omega}^{\infty} E_1(\omega_1)\,E_2(\omega-\omega_1)\,\mathrm{d}\omega_1 \tag{2.2.10}$$

The time-average intensity in a medium can be calculated by $I = 2n\varepsilon_0 c\,|E|^2$ [59]. Thus, the SFG intensity in the undepleted approximation can be estimated from the following equation:

$$I_{SFG}(L) = 8\varepsilon_0\frac{\omega^2 d_{eff}^2}{nc^3}I_1 I_2 L^2\,\mathrm{sinc}^2\left(\frac{\Delta kL}{2}\right) \tag{2.2.11}$$

Furthermore, if we assume a perfect phase-matching condition ($\Delta k = 0$), the intensity of the SFG increases parabolically with the propagation length in the nonlinear medium.

$$I_{SFG}(L) = 8\varepsilon_0\frac{\omega^2 d_{eff}^2}{nc^3}I_1 I_2 L^2 \tag{2.2.12}$$

If the process is not phase-matched $\Delta k = \pi$, then a nonlinear signal that varies with a sinusoidal function is achieved $I_{SFG}(L) \propto \mathrm{sinc}^2\left(\frac{\pi L}{2}\right)$. In Figure 2.1 (c) are shown the SFG processes for $\Delta k = 0$ (red) and $\Delta k = \pi$ (shadowed grey).

2.2.2 Phase-matching

From the above calculation, we can deduce that when the phases of the three waves inside the medium propagate together, phase-matching is achieved, and second-order processes can be efficiently generated.

This condition can be fulfilled using birefringent crystals. In those crystals, waves with the same frequency but different polarisations are propagated inside the medium with different refractive index values. Similarly, birefringent crystals enable different frequencies to be propagated at the same speed for a given crystal orientation. The most used birefringent crystals for phase-matching are the uniaxial crystals.

Figure 2.1 (a) and (b) show the phase matching diagram representation of a hypothetical uniaxial crystal in the real and reciprocal spaces, respectively. In uniaxial crystals, we can find a direction where all the perpendicular directions are optically equivalent. This direction is called the optical axis. Light propagating in the optical axis direction, $\theta = 0°$, is propagated with the ordinary refractive index n_o. On the other hand, light polarised parallel to the optical axis, $\theta = 90°$, is propagated with the extraordinary refractive index n_e.

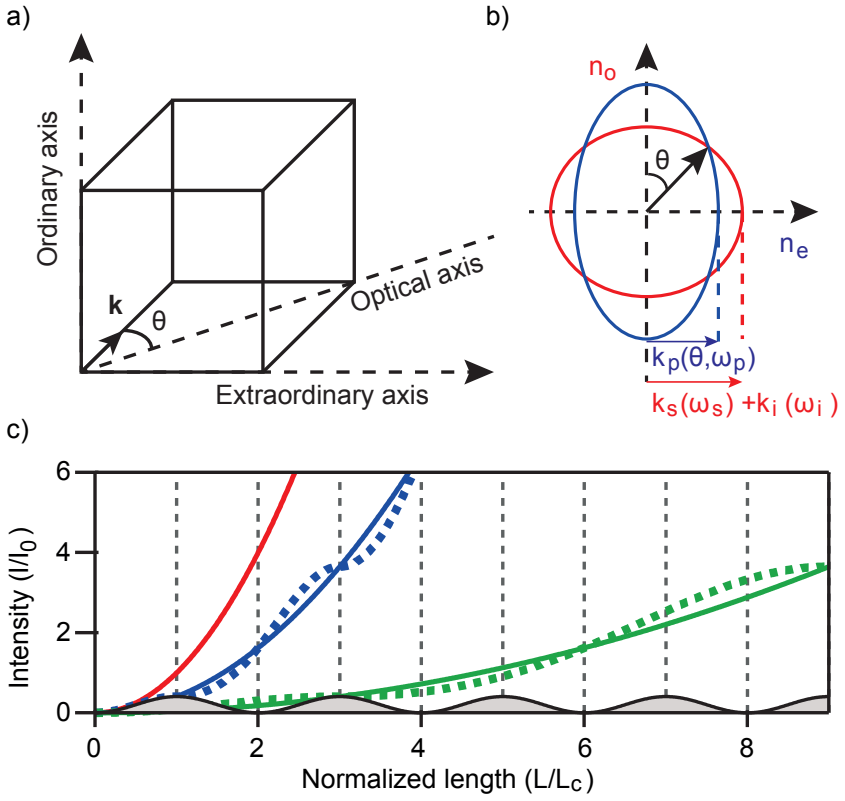

FIGURE 2.1: Phase matching diagram a) in real space and b) in the reciprocal space. c) Normalized intensity propagation for $\Delta k = 0$ (in red), $\Delta k = \pi$ (in grey) and the quasi-phase-matching calculations for $m = 1$ (blue) and $m = 3$ (green).

The refractive index of linear light propagating in a different angle than parallel or perpendicular to the optical axis can be calculated as follows:

$$\left(\frac{1}{n_e(\lambda,\theta)}\right)^2 = \left(\frac{\cos\theta}{n_o(\lambda)}\right)^2 + \left(\frac{\sin\theta}{n_e(\lambda)}\right)^2 \tag{2.2.13}$$

or by solving the equation for $n_e(\lambda,\theta)$:

$$n_e(\lambda,\theta) = n_o(\lambda)\sqrt{\frac{1+(\tan\theta)^2}{1+\left(\frac{n_o(\lambda)}{n_e(\lambda)}\tan\theta\right)^2}} \tag{2.2.14}$$

In some very well known nonlinear crystals like BBO, $LNbO_3$ or GaSe the ordinary refractive index is higher than the extraordinary refractive index ($n_o(\lambda) > n_e(\lambda)$). Those crystals are called negative uniaxial crystals. On the other hand, crystals such as BGGSe and ZGP are positive uniaxial crystals and show higher values of the extraordinary refractive index than the ordinary refractive index ($n_o(\lambda) < n_e(\lambda)$).

For phase-matching, type 1 or type 2 phase-matching conditions are distinguished depending on the chosen polarisations for the different waves interacting in the nonlinear process. For consistency, in this thesis, the three interacting-wave in the second-order nonlinear process are called pump-wave, signal-wave and idler-wave. The pump-wavelength is the shortest and the idler-wavelength the longest ($\lambda_{pump} < \lambda_{signal} < \lambda_{idler}$).

For type 1 phase-matching in a negative uniaxial crystal, the signal- and idler-waves must propagate with the ordinary refractive index. On the other hand, the pump-wave is required to be perpendicularly polarised, propagating in the extraordinary direction at θ angle with respect to the optical axis ($e \leftarrow o + o$).

$$\frac{1}{\lambda_p n_e(\lambda_p,\theta)} = \frac{1}{\lambda_s n_o(\lambda_s)} + \frac{1}{\lambda_i n_o(\lambda_i)} \tag{2.2.15}$$

where λ_p, λ_s and λ_i are the centre wavelength of the pump, signal and idler waves, respectively.

For type 2 phase-matching in a negative uniaxial crystal, the pump wave is polarised in the extraordinary direction as well as one of the other two waves. Moreover, the third wave is polarised in the ordinary direction ($e \leftarrow e+o$ or $e \leftarrow o+e$). Typically, the nonlinearity of the medium, at the phase-matching θ angle, determines which wave, signal or idler, is preferable to be polarised in the extraordinary direction.

$$\frac{1}{\lambda_p n_e(\lambda_p,\theta)} = \frac{1}{\lambda_s n_e(\lambda_s,\theta)} + \frac{1}{\lambda_i n_o(\lambda_i)} \tag{2.2.16}$$

or,

$$\frac{1}{\lambda_p n_e\left(\lambda_p,\theta\right)}=\frac{1}{\lambda_s n_o\left(\lambda_s\right)}+\frac{1}{\lambda_i n_e\left(\lambda_i,\theta\right)} \tag{2.2.17}$$

2.2.3 Quasi phase-matching

Another way of achieving phase-matching is via quasi-phase-matching (QPM). In QPM, the phases of the three waves interacting in the second-order nonlinear processes are not matched by using the directional properties of a birefringent crystal but periodically modulating a highly nonlinear crystal. Thus the three waves can have the same polarisation simplifying the optical design. In this case, electro-optic crystals such as $LiNbO_3$ are typically used to grow periodically poled or oriented patterned samples.

From Figure 2.1 (c) we can deduce that when the thickness of the nonlinear crystal is $l_c=\frac{\pi}{m\Delta k}$ (where $m=1,3,5\ldots$), the generated nonlinear signal has a local maximum independent of Δk. This length is called the coherence length.

The signs of $\chi^{(2)}$ and d_{eff} are flipped by rotating the nonlinear crystal axis by π. Thus, phase-matching can be achieved by rotating the nonlinear crystal axis every ml_c. The amplification achieved in the undepleted approximation for the QPM case can be estimated by solving the equation 2.2.8:

$$E\left(\omega_3,L\right)=2\frac{\omega_3 d_{eff}}{n_3 c}E_1\left(\omega_1,0\right)E_2\left(\omega_2,0\right)\sum_{n=0}^{N-1}\left(-1\right)^2\int_{\Lambda n}^{\Lambda(n+1)}e^{i\Delta kz}\mathrm{d}z \tag{2.2.18}$$

where Λ is the spacing in the periodically poled nonlinear crystal. Replacing Λ by the coherence length, we achieve a similar propagation dependent relation obtained in equation 2.2.9, but with an attenuation factor $\left(\frac{2}{\pi m}\right)^2$.

$$I_{SFG}\left(L\right)=8\varepsilon_0\frac{\omega^2 d_{eff}^2}{nc^3}I_1 I_2 L^2\left(\frac{2}{\pi m}\right)^2 \tag{2.2.19}$$

Thus, to achieve the maximum nonlinear signal from a quasi-phase-matched process, it is desirable to pole the crystal periodically every $l_c=\frac{\pi}{\Delta k}$. For instance, the phase-mismatch between the 3.2 μm and 1064 nm pulses in $LiNbO_3$ can be calculated as $\Delta k=k_p-k_s-k_i=2\pi\left(\frac{n_p}{\lambda_p}-\frac{n_s}{\lambda_s}-\frac{n_i}{\lambda_i}\right)$, where $\lambda_p=1064$ nm,

$\lambda_s = 1600$ nm and $\lambda_i = 3200$ nm. Thus, the required QPM period in PPLN is ~ 30 μm, with an estimated coherence length of $l_c = \frac{\pi}{\Delta k} \approx 15$ μm.

2.2.4 Broadband phase-matching in non-collinear angle

Until now we have assumed $\Delta k = 2\pi \left(\frac{n_p}{\lambda_p} - \frac{n_s}{\lambda_s} - \frac{n_i}{\lambda_i} \right)$ neglecting the possible variations of k over a given $\Delta\omega$ bandwidth. This condition is fulfilled for narrowband pulses, but generally not when broadband pulses are involved in the nonlinear process. Similarly to the Taylor expansion conducted for broadband pulse wave-vectors in equation 2.1.3, we can determine the wave-vector mismatch for broadband pulses as follows:

$$\Delta k(\omega) = \Delta k(\omega_0) + \frac{\partial \Delta k(\omega)}{\partial \omega}\Big|_{\omega_0} (\omega - \omega_0) + \frac{1}{2}\frac{\partial^2 \Delta k(\omega)}{\partial \omega^2}\Big|_{\omega_0} (\omega - \omega_0)^2 + \ldots \quad (2.2.20)$$

where $\frac{\partial k(\omega)}{\partial \omega}\Big|_{\omega_0} = v_{\omega_0}^{-1}$ and $\frac{\partial^2 k(\omega)}{\partial \omega^2}\Big|_{\omega_0} = g_{\omega_0}$ are the GV and GVD respectively centred at ω_0.

For broadband phase-matching not only the first term in equation 2.2.20 has to be fulfilled but also higher-order terms. In collinear geometry, the second-order term would be only close to zero when $v_p \approx v_s \approx v_i$ or for narrowband pumps when $v_s \approx v_i$. In general, it is challenging to find a nonlinear material that fulfils this condition [42]. Only in type 1 degenerative case ($\omega_s = \omega_i$) can be achieved $v_s = v_i$.

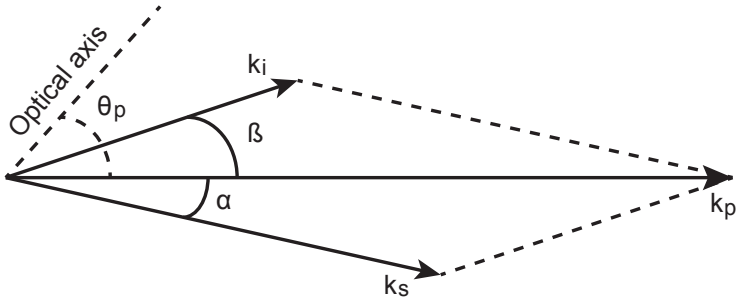

FIGURE 2.2: Non-collinear geometry diagram of the three interacting wave-vectors in the nonlinear process.

Another option to achieve broadband phase-matching is to use non-collinear geometry. In Figure 2.2 is shown the diagram for non-collinear geometry. The new

phase-matching conditions can be deduced from the diagram and re-write the equations as follows:

$$\Delta k = k_p - k_s \cos\alpha - k_i \cos\beta \tag{2.2.21}$$

$$k_s \sin\alpha = k_i \sin\beta \tag{2.2.22}$$

The pump-wave is generally narrowband in OPCPA processes. Therefore, we can neglect the frequency dependency of k_p and achieve broadband phase-matching by assuming $\Delta k\left(\omega_0\right) = 0$ and $\frac{\partial \Delta k(\omega)}{\partial \omega}\Big|_{\omega_0} = 0$, which can be fulfilled using the right non-collinear angle. Typically, the required α and β angles for broadband phase-matching are small [63]. Thus the equation 2.2.22 can be further simplified to $\alpha \approx \frac{k_i}{k_s}\beta$.

$$\Delta k\left(\omega_0\right) = k_p\left(\omega_p\right) - k_s\left(\omega_s\right)\cos\alpha - k_i\left(\omega_i\right)\cos\beta = 0 \tag{2.2.23}$$

$$\frac{\partial \Delta k}{\partial \omega_{s,i}} = \frac{1}{v_{i,s}\cos\left(\alpha+\beta\right)} - \frac{1}{v_{s,i}} \tag{2.2.24}$$

where $v_{i,s}^{-1} = \frac{\partial k(\omega)}{\partial \omega}\Big|_{\omega_{i,s}}$ are the GVs at the centre wavelength of the idler and signal waves respectively. Thus, if equation 2.2.23 and 2.2.24 are fulfilled, the phase-matching bandwidth will be limited by the next term $\frac{\partial^2 \Delta k}{\partial \omega^2} \neq 0$.

$$\frac{\partial^2 \Delta k}{\partial \omega_{s,i}^2} = \frac{1}{v_{s,i}}\tan\left(\alpha+\beta\right)\tan\beta\left(\frac{\lambda_s}{2\pi n_s v_s} + \frac{\lambda_i}{2\pi n_i v_i}\right) - g_s - g_i \tag{2.2.25}$$

where g_i and g_s are the GVDs at the centre wavelength of idler and signal waves, respectively. If we assume that the accumulated phase-mismatch over the crystal length L is not greater than π, then by solving $\Delta k \approx \left(\frac{\partial^2 \Delta k}{\partial \omega_{s,i}^2}\Delta\omega^2\right) L = \pi$, we can estimate the maximum phase-matching bandwidth allowed by the nonlinear crystal:

$$\Delta\lambda_{s,i} = \frac{\lambda^2}{c}\sqrt{\frac{1}{2\pi L\left(\frac{\partial^2 \Delta k}{\partial \omega_{s,i}^2}\right)}} \tag{2.2.26}$$

The phase-matching acceptance bandwidth is higher at thinner crystals. This effect is widely exploited in ultrafast broadband pulse characterisation techniques such as SHG Frequency resolved optical gating (SHG-FROG). Consequently, ultra-thin $L < 30$ μm nonlinear crystals are used to characterise the ultra-broadband pulses.

The equation 2.2.26 can be used together with the nonlinear crystal's figure-of-merit value (see Figure 1.3) to choose the optimum nonlinear crystals for the second-order nonlinear process. For instance, if we compare the phase-matching bandwidths of $LNbO_3$ and $KNbO_3$, for our 3.2 μm OPCPA, the expected acceptance bandwidths for 2 mm long crystals are $\Delta\lambda_i = 524$ nm ($\theta_p = 50.98°$ and $\alpha = 2.98°$) and $\Delta\lambda_i = 609$ nm ($\theta_p = 41.6°$ and $\alpha = 2.58°$), respectively. Considering that the figure-of-merit value is also higher in $KNbO_3$ (see Figure 1.3), $KNbO_3$ is a good candidate for efficient pulse amplification of the 3.2 μm idler waves [49, 64, 65].

2.2.5 OPA

In the first part of this section, equations for the SFG process have been deduced fulfilling the $\omega_3 = \omega_2 + \omega_1$.frequency relation. Similarly, frequency relations for DFG and OPA processes can be defined as $\omega_1 = \omega_3 - \omega_2$ where $\omega_1 < \omega_2 < \omega_3$, or using the pump/signal/idler notation $\omega_i = \omega_p - \omega_s$. To avoid confusions, we will re-define also the coupled three-wave equations for ω_p, ω_s and ω_i:

$$\frac{\mathrm{d}E_i(z)}{\mathrm{d}z} = 2i\frac{\omega_i d_{eff}}{n_i c} E_s^*(z) E_p(z) e^{i\Delta kz} \tag{2.2.27}$$

$$\frac{\mathrm{d}E_s(z)}{\mathrm{d}z} = 2i\frac{\omega_s d_{eff}}{n_s c} E_i^*(z) E_p(z) e^{i\Delta kz} \tag{2.2.28}$$

$$\frac{\mathrm{d}E_p(z)}{\mathrm{d}z} = 2i\frac{\omega_p d_{eff}}{n_p c} E_s(z) E_i(z) e^{-i\Delta kz} \tag{2.2.29}$$

An analytical equation can be deduced for the OPA process, assuming that the pump remains constant (undepleted) during the amplification process. The undepleted approximation reduces, in this case, the equation system from three differential equations to two equations:

$$\frac{\mathrm{d}^2 E_{s,i}(z)}{\mathrm{d}z^2} + i\Delta k \frac{\mathrm{d}E_{s,i}(z)}{\mathrm{d}z} = 2\Gamma^2 E_{s,i}(z) \tag{2.2.30}$$

where $\Gamma^2 = \frac{2\omega_s \omega_i d_{eff}^2}{n_p n_s n_i \varepsilon_0 c^3} I_p$, being I_p the undepleted pump intensity. The figure-of-merit is determined from Γ^2 and includes all the terms in Γ^2 that depend on the nonlinear crystal properties: $figure\text{-}of\text{-}merit = \frac{d_{eff}^2}{n(\omega_p)n(\omega_s)n(\omega_i)}$.

Moreover, suppose we assume that the signal-wave is zero at the beginning of the nonlinear process. In that case, we can solve the second-order differential equation for the following initial conditions: $E_i(0) = E_i$, $\frac{\mathrm{d}E_i(0)}{\mathrm{d}z} = 0$ and $E_s(0) = 0$.

$$E_i(z) = E_i(0)\left(\cosh(gz) + i\frac{\Delta k}{g}\sinh(gz)\right) e^{-i\frac{\Delta k}{2}z} \tag{2.2.31}$$

$$E_s(z) = -2c_1 \sinh(gz)\, e^{-i\frac{\Delta k}{2}z} \tag{2.2.32}$$

where $g^2 = \Gamma^2 - \left(\frac{\Delta k}{2}\right)^2$ and c_1 is a constant that can be calculated, introducing back the solutions in the coupled-wave-equation:

$$|c_1|^2 = \frac{1}{2}\frac{1}{n_s \varepsilon_0 c}\frac{\omega_s}{\omega_i}\frac{\Gamma^2}{g^2}\left(\frac{g^2\cosh(gz) + \Delta k^2 \sinh(gz)}{4g^2\cosh(gz)\,\Delta k^2 \sinh(gz)}\right) \tag{2.2.33}$$

The solutions can be simplified further assuming $g2$, $\Gamma^2 \gg \Delta k^2$:

$$I_i(z) = I_i(0)\cosh^2(\Gamma z) \tag{2.2.34}$$

$$I_s(z) = \frac{\omega_s}{\omega_i} I_i(0)\sinh^2(\Gamma z) \tag{2.2.35}$$

where the relation $\frac{\omega_s}{\omega_i}$ determines how much of one wave is amplified with respect to the other. This relation is also defined by the Manley-Rowe relations [66], which can be deduced from the coupled three-wave equations assuming that the sum of the involved wave intensities needs to be conserved $I(z) = I_p(z) + I_s(z) + I_i(z)$.

$$\frac{\mathrm{d}}{\mathrm{d}z}\left(\frac{I_s(z)}{\omega_s}\right) = \frac{\mathrm{d}}{\mathrm{d}z}\left(\frac{I_i(z)}{\omega_i}\right) = -\frac{\mathrm{d}}{\mathrm{d}z}\left(\frac{I_p(z)}{\omega_p}\right) \tag{2.2.36}$$

One implication for OPA systems is that higher pump frequencies imply a larger difference in the amplification ratio between the signal and idler waves. Thus, pump lasers with longer wavelengths are required to amplify long-wavelength mid-infrared idler waves efficiently.

From equation 2.2.36 and assuming $I_{s,i}(0) \ll I_p(0)$ and $I_s(0) = 0$ we can achieve the following relations:

$$P_i(z) = \frac{\omega_i}{\omega_s}\left(P_p(0) - P_p(z)\right) \tag{2.2.37}$$

$$P_s(z) = \frac{\omega_s}{\omega_i} P_i(z) \tag{2.2.38}$$

where $P_{p,s,i}(z)$ are the pump, signal and idler powers in the OPA respectively and$P_p(0)$ is the input pump power. For instance, one of our 3.2 μm OPCPA stages is pumped with 100 W at 1064 nm. Thus, if we assume that the pump power is fully converted into the idler and signal waves, a maximum amplification of 33 W would be transferred to the idler at 3.2 μm (33% of the pump power). The results are less favourable in our 7 μm OPCPA pumped with the 2052 nm pulses, with a maximum pump to the idler efficiency of $\sim$ 29%.

Typically, pump to signal + idler conversion efficiency is limited to around 50% due to mode matching (beam size difference), temporal amplitude matching (mainly in OPCPAs), phase-matching and temporal/spatial walk-off (the second one in non-collinear geometries). Extra constraints such as limited peak intensities to avoid damage, self-focusing, SPM or beam/phase deterioration need to be considered. For instance, in our 3.2 μm OPCPA, the last two OPA stages deliver a maximum signal + idler conversion efficiency of 30% to 35%, while in our 7 μm OPCPA these values are around 15% to 20%.

The DFG process is described by the equation 2.2.30 using $E_i(0) = 0$ and $E_p(0)_s(0)$ as the initial conditions. When a single-broad pulse is used to drive the DFG process, the pump and signal waves are comprised of the same broad pulse. Thus, the frequencies inside the pulse are combined to generate the idler wave. This process is called intrapulse-DFG (IP-DFG) [40, 67, 68]. In general, the narrower the input pulse longer is the centre wavelength of the generated idler pulse. When ultra-broadband pulses are used, the generated idler-wave is shifted to bluer frequencies. When the phase-matching of the IP-DFG process is described by the

equation 2.2.15 or equation 2.2.17, pump and signal waves need to be perpendicularly polarised to each other. Thus, to fulfil this condition, the polarisation of the input pulse is rotated to 45°.

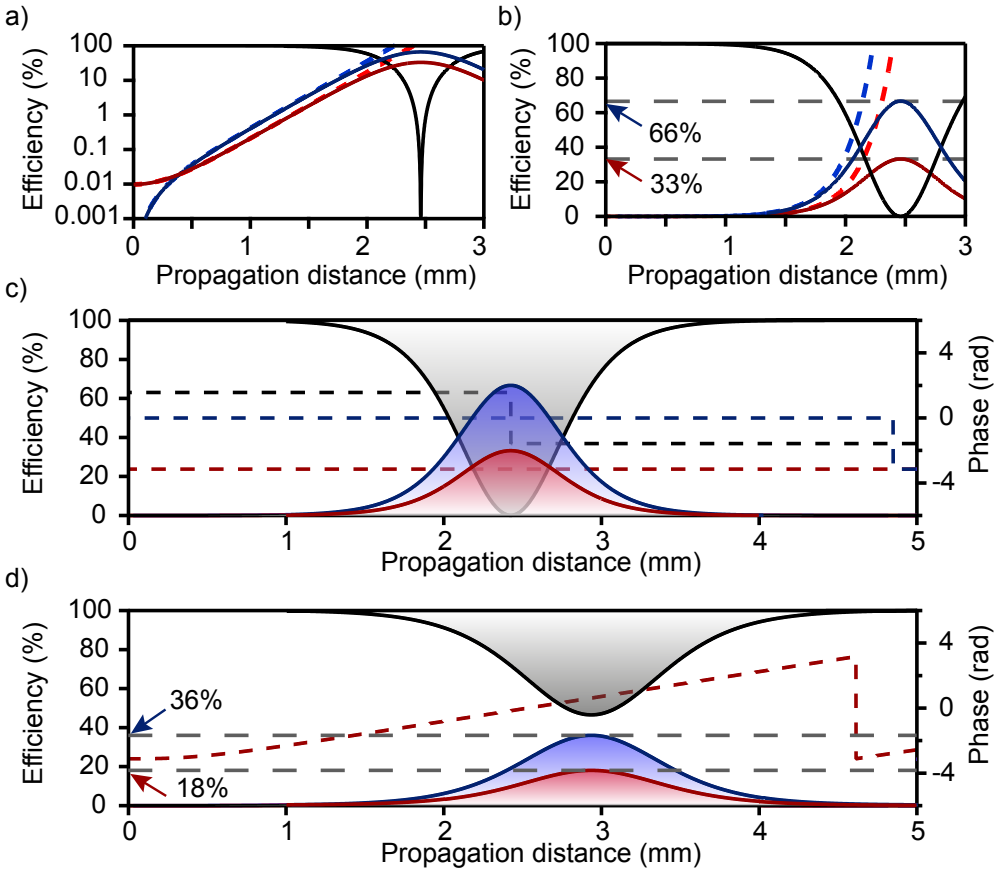

FIGURE 2.3: The efficiency of OPA in log scale a) and in linear scale b) of the coupled three-wave for $\Delta k = 0$. The dashed lines show the solution of the undepleted pump analytical solution, while the solid lines show the depleted pump numerical solution. c) Amplitude efficiency (shadowed curves) and phase propagation (dashed lines) for $\Delta k = 0$. d) Amplitude efficiency (shadowed curves) and idler phase propagation (dashed line) for $\Delta k > 0$, by shifting $\theta = 0.25°$ from the perfect phase-matching angle. The black lines represent the propagation behaviour of the pump wave (1064 nm), in blue is shown the signal wave (1600 nm) and in red the idler wave (3200 nm). The grey dashed line shows the maximum amplification expected for signal and idler when $\Delta k = 0$ in b) and $\Delta k > 0$ in d).

Among the undesired effects when driving the OPA process, we need to take special care to avoid the optical parametric generation (OPG), or parametric superfluorescence [69–71]. This effect can be produced when the temporal and spatial miss-matches are significant or when the nonlinear crystal is over-pumped. In the OPG process, the amplification process is carried out in the absence of the seed wave. Instead of amplifying the seed wave, quantum fluctuations or the background noise is amplified. At the nonlinear crystal output, a wave with similar

frequency, direction, and power as our seed wave is generated. Unfortunately, these waves are unstable and do not conserve phase or coherence from the seed wave.

Figure 2.3 shows the limitations of the analytical models described above. The amplification efficiency is calculated for a 3.2 μm idler beam, pumped by 1064 nm pulses, through a $KNbO_3$ nonlinear crystal and for type 1 phase-matching. $KNbO_3$ is a biaxial crystal with $n_z > n_y > n_x$ and maximum d_{eff} in xz plane [64, 65]. Thus, by cutting the $KNbO_3$ nonlinear crystal at $\phi = 0°$ and $\theta = 40°$, the required phase-matching is achieved. The ordinary refractive index is defined perpendicular to the xz plane $n_o(\lambda) = n_y(\lambda)$. Moreover, Moreover, the extraordinary refractive index at $\phi = 0°$ is determined by the x direction $n_e(\lambda) = n_x(\lambda)$.

In Figure 2.3 (a), is presented with solid lines, the pump depleted numerical solution of the coupled three-wave equation. Moreover, the analytical solution in the undepleted pump approximation is shown with dashed lines. In both cases, we have assumed $\Delta k = 0$ ($\theta = 39.07°$ and $\phi = 0°$) and a perfect temporal and spatial matching. The analytical and numerical solutions agree for the propagation distances where pump-power is maintained constant. The agreement breaks down when amplification efficiencies are higher than $5-10\%$, and the pump-power starts decreasing. Figure 2.3 (b) in linear scale shows the fulfilled Manley-Rowe relations mentioned above.

Figure 2.3 (c) and (d) show the OPA efficiency and phase for a perfect phase-matching wave propagation (c) and when a small phase-mismatch is introduced (d). For the phase-mismatch simulation, the θ angle is varied 0.25° from the perfect phase-matching angle. The idler phase stays constant for $\Delta k = 0$, and the pump is fully converted. For $\Delta k > 0$, only around 50% of the pump is converted, the nonlinear process is delayed, and the idler phase varies during the amplification. Thus, the analytical solutions mentioned above can be useful when the OPA process's efficiency is low. This condition is fulfilled to some degree in the first OPA stages but unfortunately is not valid for the last stages where the decrease in the pump power is significant.

The high prices and low damage threshold of mid-infrared nonlinear crystals make challenging the design of a mid-infrared OPCPA and encourage the need for a 3D numerical model that counts all the physical processes and mismatches. Effects such as the deterioration of the beam profile, OPG, broadband phase-mismatch and temporal-mismatch are required to be taken into account to choose the right nonlinear crystal and pulse parameters.

The mid-infrared DFG, IP-DFG and OPCPA processes shown in this thesis are pre-simulated using a code developed at Forsvarets Forsknings Institutt called Sisyfos. Sisyfos is a program library for the simulation of optical parametric frequency conversion, lasers, and beam propagation in nonlinear or turbulent media [72].

2.2.6 Linear electro-optic effect

Another interesting nonlinear effect is the electro-optic effect, which is a particular case of the DFG process where $\omega_p = \omega_s$ and $\omega_i = 0$. Thus from equation 2.2, we can define the induced polarisation as follows:

$$P(\omega_p) = P^{(1)}(\omega_p) + P^{(2)}(\omega_p) = \left(n_0 + \varepsilon_0 \chi^{(2)} E(0)\right) E(\omega_p) \tag{2.2.39}$$

where $n = n_0 + \varepsilon_0 \chi^{(2)} E(0)$ is the effective refractive index that changes in the direction of $E(0)$. When a DC electric field, in a given direction, is applied to a nonlinear crystal (perpendicular to the propagation direction), a change in the refractive index is induced in that direction, and birefringence in the nonlinear crystal is introduced. The polarisation of the $E(\omega_p)$ is rotated during the propagation in the medium due to the induced birefringence. This effect is also known as the Pockels effect. It is widely used in electro-optic modulators for pulse pickers (to reduce the repetition rate) or regenerative amplifiers (to control the number of passes).

The same effect is also used widely in THz spectroscopy to directly measure the THz single-cycle fields using the so-called electro-optics sampling (EOS) technique. In this case, the THz field is the quasi-DC field that introduces the birefringence in the nonlinear medium $P^{(2)} \propto \varepsilon_0 \chi^{(2)} E(\Omega_{THz})$ [73, 74].

The change in the polarisation of a sampling pulse induced by the $E(\Omega_{THz})$ field can be measured using a pump-probe scheme. The temporal trace is directly retrieved from the EOS measurement as the change in polarisation is linearly dependent on the THz field $E(\Omega_{THz})$. For this purpose, much shorter in time and higher frequency sampling pulses are in general required to fulfil: $\omega_{sampling} \gg \Omega_{THz}$ and $\omega_{EOS} = \omega_{Sampling}$.

The frequency-dependent response function of the EOS signal can be estimated by assuming $E_{EOS}(\omega) = E_{Sampling}(\omega)$ and solving the coupled three-wave equation

for DFG. Really thin nonlinear crystals are typically used for EOS to achieve broadband phase-matching. Consequently, we may neglect losses inside the EOS crystal and use the non-depleted solution to achieve the following response function equation:

$$R(\Omega) = \int_{\Omega}^{\infty} \frac{2\omega}{nc} d_{eff} \left(\frac{e^{-i\Delta k L} - 1}{\Delta k} \right) E^{*}_{Sampling}(\omega)\, E_{Sampling}(\omega - \Omega)\, \mathrm{d}\omega \quad (2.2.40)$$

where $E_{Sampling}(\omega)$ is the complex field of the used sampling pulse [74]. Thus we can easily estimate the THz frequencies where the EOS is sensitive by characterising the ultrashort visible/near-infrared sampling pulse. The EOS signal in the frequency domain will be given by the product between the THz field and the response function $S_{EOS}(\Omega) = E_{THz}(\Omega)\, R(\Omega)$. Moreover, the EOS temporal trace measured in the pump-probe scheme will be the Fourier transform of $S_{EOS}(\Omega)$:

$$S_{EOS}(t) = \int_{-\infty}^{\infty} E_{THz}(\Omega)\, R(\Omega)\, e^{i\Omega t} \mathrm{d}\Omega \quad (2.2.41)$$

If $\Delta k = 0$ and $E_{Sampling}(\omega)$ spectrally super-broad and temporally compressed, then the response function $R(\Omega)$ will be constant over the THz frequencies and thus $S_{EOS}(t) \approx E_{THz}(t)$. These last conditions might be fulfilled for THz fields but not directly for mid-infrared pulses.

In the last decade, EOS technique has been extended to retrieve mid-infrared and down to 2 μm fields [40, 41, 68, 75, 76]. As the generation of ultrashort pulses in the ultraviolet is limited due to the absence of suitable sources and the high dispersion of materials in that frequency range, near-infrared pulses are still used as a sampling pulse of those mid-infrared fields. In this case, the conditions described above are not fulfilled as $\omega_{EOS} \neq \omega_{Sampling}$ and thus $E_{EOS} \neq E_{Sampling}$. If the sampling pulse is broad enough and a frequency overlap exists between the sampling spectrum and the EOS spectrum (SFG spectrum), then $E_{EOS}(\omega) = F(\omega)\, E_{Sampling}(\omega)$, where $F(\omega)$ can be a spectral filter that filters the frequencies that do not overlap between $E_{EOS}(\omega)$ and $E_{Sampling}(\omega)$. Then we can re-write the new response function as follows:

$$R(\Omega) = \int_{\Omega}^{\infty} r(\omega)\, E^{*}_{Sampling}(\omega)\, E_{Sampling}(\omega - \Omega)\, \mathrm{d}\omega \quad (2.2.42)$$

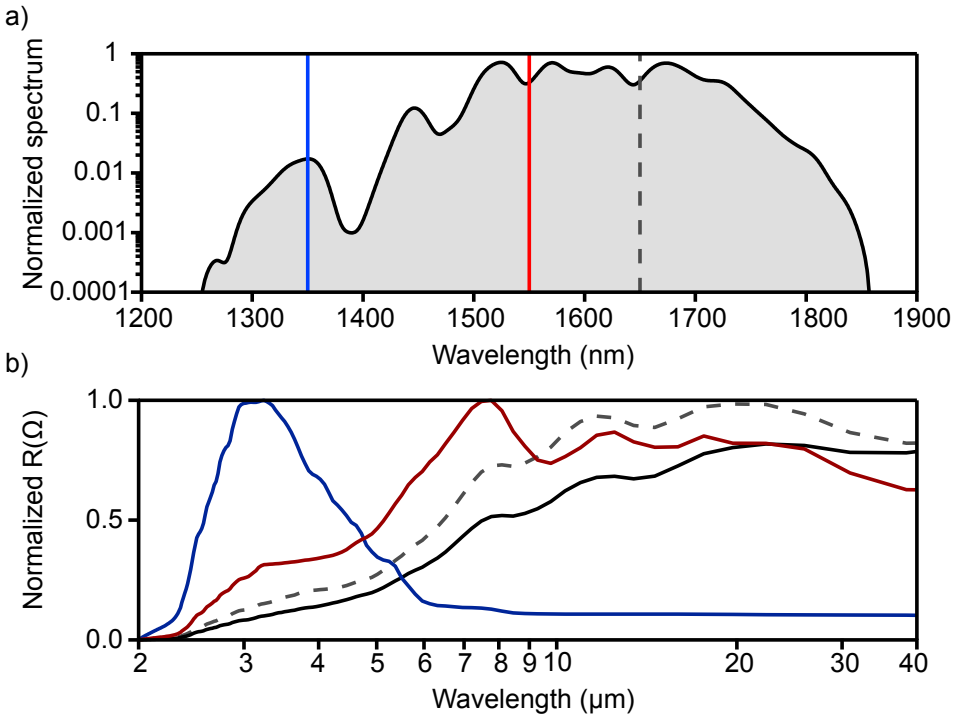

FIGURE 2.4: a) Normalised spectral density of the measured sampling pulses centred at 1550 nm (shadowed black curve) and different short-pass spectral filters. The cut-off frequency of a typical InGaAs detector is shown In dashed grey. Short-pass filters with cut-off frequencies at 1550 nm and 1350 nm are presented in red and blue, respectively. b) Normalised response function for the sampling spectral bandwidth (black curve). In dashed grey is shown the $R(\Omega)$ taking into account the spectral sensitivity of an InGaAs detector. Moreover, in red and blue are shown the response functions when short-pass filters at 1550 nm and 1350 nm are used, respectively.

where $r(\omega) = \frac{2\omega d_{eff}}{nc}\left(\frac{e^{-i\Delta kL}-1}{\Delta k}\right)F(\omega)$. The function $r(\omega)$ can include all the frequency-dependent detection responses, absorption and phase-mismatches that can be significant in the EOS measurement [76].

Figure 2.4 compares the EOS response function $R(\Omega)$ when no-filter is added $r(\omega) = 1$ (solid black line) and different short-pass filters are included. A short-pass filter's proper choice is desirable to shift the EOS detection frequency from THz to the mid-infrared regime when relatively long (21 fs) 1550 nm near-infrared probe pulses are used. When $r(\omega) = 1$, the maximum sensitivity of the EOS signal is centred at $\Omega = 0$,. When a short-pass filter is inserted, the EOS maximum sensitivity frequency is shifted to higher frequencies. For instance, inserting a short-pass filter with cut-off frequency at $\lambda = 1350$ nm the EOS maximum sensitivity frequency is moved to $\lambda = 3000$ nm (blue curve in Figure 2.4).

Experimentally, the spectral dependency of the detector is enough to shift the

EOS response to shorter wavelengths. For instance, while the solid black line in Figure 2.4 (b) shows the EOS response for $r(\omega) = 1$, the dashed grey curve is calculated by taking into account the InGaAs detector sensitivity range.

2.3 Third-order nonlinear processes

Third-harmonic generation (THG), SPM or self-focusing are some of the third-order nonlinear effects produced in some of the following experiments. Third-order nonlinear processes can be generated both in centrosymmetric and non-centrosymmetric crystals. Thus, any medium with a high nonlinear index can be used to generate those effects.

The induced polarisation in the nonlinear medium for THG, SPM or self-focusing effects can be written as follows:

$$P^{(3)}(t) = \varepsilon_0 \chi^{(3)} E^3(t) \tag{2.3.1}$$

or in the frequency domain, if a single-wave with ω_1 frequency is used to drive the nonlinear process:

$$P^{(3)}(\omega_1) = P^{(3)}(3\omega_1) + P^{(3)}(\omega_1) \tag{2.3.2}$$

The first term describes the THG with $P^{(3)}(3\omega_1) = \varepsilon_0 \chi^{(3)} E(\omega_1) E(\omega_1) E(\omega_1)$, while the second term is related to the Kerr effect $P^{(3)}(\omega_1) = \varepsilon_0 \chi^{(3)} E(\omega_1) E^*(\omega_1) E(\omega_1)$. We can define the nonlinear refractive index as $n_2 = \frac{3}{4\pi^2 \varepsilon_0 c} \chi^{(3)}$ and describe the third-order Kerr effects as:

$$P^{(3)}(\omega_1) = n_2 I(\omega_1) E(\omega_1) \tag{2.3.3}$$

In high-power lasers, it is desirable to avoid third-order nonlinear processes, as phase deteriorations or damages in the nonlinear crystals can be induced. The peak intensity threshold to trigger these effects can be estimated from the so-called $B_{integral}$, which describes the total nonlinear phase accumulated during the beam propagation:

$$B_{integral} = \frac{2\pi}{\lambda} \int_0^{\infty} n_2 I\left(z\right) \mathrm{d}z \tag{2.3.4}$$

Thus, the value of the $B_{integral}$ keeps accumulating over all the optics in the beam path. When $B_{integral} > \pi$, it is likely to produce the Kerr effect, inducing the generation of SPM and self-focusing processes. In high-energy lasers, where these effects must be avoided, the $B_{integral}$ is advised to maintain it below 0.1π. In general, most of the optics in the beam path can be neglected for calculating the $B_{integral}$. Only optics where n_2 is high, the peak-intensity considerable, or medium length significant are considered. Moreover, typically the peak intensity inside the crystal is assumed to be constant. Thus, a simplified version of equation 2.3.4 can be re-written as follows:

$$B_{integral} = \frac{2\pi}{\lambda} \sum_{i=1}^{N} n_2^{(i)} I_i L_i \tag{2.3.5}$$

where N is the amount of optics in the beam path that contribute significantly to the $B_{integral}$, $n_2^{(i)}$ is the nonlinear refractive index, I_i is the intensity, and L_i is the length.

2.3.1 Self-phase modulation

The Kerr effect induces an intensity-dependent refractive index change which is responsible for SPM and self-focusing processes. From equation

$$n = n_0 + n_2 I \tag{2.3.6}$$

If the refractive index's change is instantaneous and induced by an ultrashort pulse, the pulse itself will be affected by the refractive index change. From equation 2.3 the overall accumulated phase by the electric-field due to the Kerr effect can be re-defined as follows:

$$\varphi\left(t, z\right) = \frac{2\pi}{\lambda_0} \left[n_0 + n_2 I\left(t\right)\right] z - \omega_0 t \tag{2.3.7}$$

If we assume a Gaussian envelope for our ultrashort pulses $I(t) = I_0 e^{-\left(\frac{t}{\tau_p}\right)^2}$ where τ_p is the pulse width, a clear time-dependent frequency shift induced by a second-order temporal phase is achieved.

$$\omega(t)\, t = \frac{\mathrm{d}\varphi(t)}{\mathrm{d}t} t = -\omega_0 t - \frac{4\pi n_2 I_0}{\lambda_0 \tau_p^2} L t^2 e^{-\left(\frac{t}{\tau_p}\right)^2} \tag{2.3.8}$$

where $\omega(t)$ is also known as instantaneous frequency, L is the propagation length, and I_0 is the peak intensity of the pulses.

While the linear dispersion is defined analytically in the frequency domain as the second-order phase $E(\omega, z) \propto E_0(\omega)\, e^{-i\frac{GDD(z)}{2}(\omega-\omega_0)^2}$, the SPM process is defined in the time domain as a second-order phase $E(t, z) \propto E_0(t)\, e^{-i\frac{4\pi n_2 I_0}{\lambda_0 \tau_p^2} z t^2}$. Thus, the linear dispersion and SPM phase are correlated by a Fourier transformation. The pulse broadening and the accumulated overall (linear + nonlinear) dispersion can be estimated as follows: i) introduce chirp in the frequency domain defined by equations 2.1.2 and 2.1.3, ii) calculate the Fourier Transform and introduce the SPM phase in the time domain as described in equation 2.3.7, and iii) compute the inverse Fourier Transform. While numerically, this procedure is repeated every small propagation step, analytically, we can estimate in a single step the broadened bandwidth and overall chirp as follows:

$$E(\omega, L) \propto E_0 e^{-\left(\frac{1}{\Delta\omega_0^2} + i\frac{GDD_0(L)}{2}\right)(\omega-\omega_0)^2} \tag{2.3.9}$$

where $\Delta\omega_0$ is the initial pulse bandwidth, and GDD_0 is the dispersion. If we calculate the Fourier transform, we get the stretched pulse in the time domain:

$$E(t) \propto E_0 e^{-\omega_0 t} e^{-\frac{t^2}{4}\left(\frac{1}{\Delta\omega_0^2} + i\frac{GDD_0(L)}{2}\right)^{-1}} \tag{2.3.10}$$

where the real part of the second exponential is related to the temporal pulse duration $\Delta t(z) = \sqrt{Re\left[\left(\frac{1}{\Delta\omega_0^2} + i\frac{GDD_0(L)}{2}\right)^{-1}\right]}$, and the imaginary part describes the nonlinear phase contribution induced by the medium dispersion. Now, we can add the nonlinear SPM phase defined in equation 2.3.8.

$$E(t, z) \propto E_0 e^{-\omega_0 t} e^{-\left[\frac{1}{4}\left(\frac{1}{\Delta\omega_0^2} + i\frac{GDD_0(L)}{2}\right)^{-1} + \frac{4\pi n_2 I_0}{\lambda_0 \tau_p^2} z\right] t^2} \tag{2.3.11}$$

and implementing the Fourier transformation, we can calculate the new propagated field in the frequency domain to estimate the final bandwidth and chirp:

$$E(\omega, z) \propto E_0 e^{-\left(\frac{1}{\Delta\omega_1^2(z)}+iC(z)\right)(\omega-\omega_0)^2} \tag{2.3.12}$$

where $\Delta\omega_1(z) = \Delta\omega_0\sqrt{1+4Kz\left[GDD_0(L)+K\left(GDD_0^2(L)+\frac{4}{\Delta\omega_0^4}\right)z\right]}$ is the bandwidth generated from SPM and being $K = \frac{4\pi n_2 I_0}{\lambda_0 \tau_p^2}$. Figure 2.5 shows the broadening estimated for a hypothetical 100 fs 3.2 μm pulse after being pre-chirped by different materials. While a positively pre-chirped pulse (through a 1 mm Silicon wafer with $GDD_0 = 486\ fs^2$) induces a continuously broadening effect (see solid red line), a negatively pre-chirped pulse (through a 1 mm YAG wafer in blue $GDD_0 = -460\ fs^2$) causes a narrowing effect at the initial states of the SPM process. Therefore, the broadening is delayed for the negatively pre-chirped scenario [77].

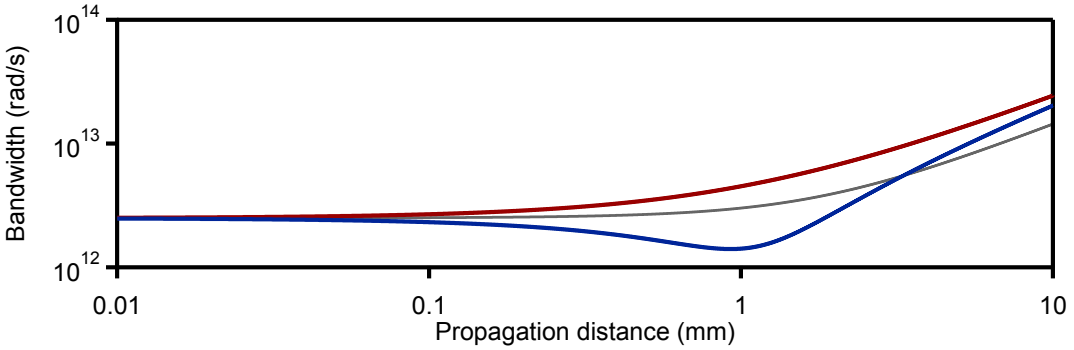

FIGURE 2.5: SPM induced evolution of the spectral bandwidth of a hypothetical 3.2 μm 100 fs pulse with negatively pre-chirped input pulse (blue), positively chirped input pulse (red) and no chirped (thin grey line).

Moreover, $C(z) = \dfrac{GDD_0(L)+2K\left(GDD_0^2(L)+\frac{4}{\Delta\omega_0^4}\right)z}{2+8Kz\left[GDD_0(L)+K\left(GDD_0^2(L)+\frac{4}{\Delta\omega_0^4}\right)z\right]} + GDD(z)$ is the accumulated chirp from the dispersive medium and the SPM process.

If the dispersion introduced by the material is negative, this dispersion can counteract the chirp introduced by the SPM process. Proper management of the crystal and pulse parameters can cancel the two dispersion terms. Consequently, the pulse gets broadened in the frequency domain and compressed in the time domain. Therefore, SPM in an anomalous dispersive medium (negative GDD) can be exploited to generate self-compressed pulses.

2.3.2 Filamentation

A non-uniform beam distribution in space introduces an inhomogeneous varying refractive index in the nonlinear medium. For instance, if we assume a Gaussian beam in space, the intensity in the middle of the beam will be higher. Thus, the refractive index change will be higher in the middle of the beam than in the surrounding areas. The non-uniform refractive index induced in the medium produces the self-focusing effect making the beam collapse. Luckily, before the beam entirely collapses, plasma is generated due to the high intensities achieved, and a defocusing effect is produced. The beam fluctuates between self-focusing and plasma defocusing effects achieving a quasi-static filament. Consequently, the beam is maintained focused through longer distances than estimated in the linear beam propagation by the Rayleigh length:

$$Z_r = \frac{\pi w_0}{\lambda M^2} \tag{2.3.13}$$

where Z_r is the Rayleigh length, w_0 is the laser beam waist radius, and $M2$ is the factor that approximates a real beam to a Gaussian beam [78–82].

The threshold to generate the self-focusing effects is determined by the critical peak-power. The critical-peak-power can be estimated assuming that the divergence induced by the linear beam propagation $\theta_{diff} \approx \sqrt{\alpha}\frac{\lambda}{\pi n_0 w_0}$, and the self-focusing convergence $\theta_{sf} \approx \sqrt{\frac{2n_2 I_{cr}}{n_0}}$, are comparable [60]:

$$P_{cr} = \frac{\pi w_0^2 I_{cr}}{2} \approx \alpha \frac{\lambda^2}{4\pi n_0 n_2} \tag{2.3.14}$$

where $\alpha \approx 1.86$ for a Gaussian beam [83]. The self-focusing effect depends not only on the intensity of the pulse but also on the beam size [59, 60, 83]. Thus, the critical-peak-power parameter is more suitable than the critical-peak-intensity value to estimate the self-focusing threshold.

In the filamentation process, plasma-induced defocusing effects and multiphoton photon absorption (MPA) effects must be considered. These effects can be estimated using the equation 2.6 and defining the current-density as follows:

$$\frac{\mathrm{d}J(t)}{\mathrm{d}t} = \frac{e^2}{m_e}\rho(t)E(t) - J(t)/\tau_c \tag{2.3.15}$$

where τ_c is the electron collision time and $\rho(t)$ is the electron-density. The UPPE equation given in 2.6 can be solved together with equation 2.3.15 and the following kinetic equation for plasma concentration:

$$\frac{\partial \rho}{\partial t} = \frac{\sigma}{U_g} I\rho + \frac{\sigma_K}{K\hbar\omega_0} I^K - a\rho^2 \tag{2.3.16}$$

To solve the above differential equations, we may assume $J(0) = 0$ and $\rho = \rho_{at}$ where ρ_{at} is the initial valence ban electron-density.

The first term in equation 2.3.16 describes the avalanche ionisation with $\sigma = \frac{2e^2}{m_e n_0 \varepsilon_0 c} \frac{1/\tau_c}{(1/\tau_c)^2+\omega_0^2}$ being the cross-section for the inverse bremsstrahlung [84], m_e the electron mass, e the electron charge, ω_0 is the centre frequency of the pulse, U_g the bandgap energy in solids (or ionisation potential for gases) and I the laser pulse intensity. The second term is related to the MPA, where K is the multiphoton ionisation (MPI) order and σ_K the MPI cross-section. In general, the cross-section decreases while the multiphoton order increases. Thus, in general, only the first multiphoton order that can be induced at a given laser frequency is taken into account. For instance, if we pump silicon ($U_g = 1.12$ eV) with 3.2 μm pulses ($E = 0.39$ eV), then the three-photon absorption will be the most pronounced multiphoton process. Consequently, the second term in equation 2.3.16 will be written as $\frac{\sigma_3}{3\hbar\omega_0} I^3$.

The third term in 2.3.16 describes the electron-hole recombination process, being a the recombination rate. The recombination rate is inversely proportional to the recombination time τ_r, generally much longer than τ_c. Thus, the third term can be neglected if a femtosecond pulse induces the ionisation process instantaneously. This assumption can be valid with kHz repetition rate lasers but problematic for lasers with MHz repetition rates where the time between pulses is < 10 μs.

Moreover, due to the high nonlinearity required to measure these parameters, the uncertainty of the values found in the literature can be significant. Parameters such as the nonlinear refractive index n_2 and multiphoton cross-sections can vary from literature to literature. These parameters can be used to predict the filamentation process qualitatively. Still, a fine-tuning of these parameters are typically required to achieve a quantitative match between simulations and experiments.

UPPE for solids

A UPPE-based numerical modelling code called gUPPElab is used to choose the right material and thickness for the filamentation process, or ultrashort pulse broadening in a solid core fibre [61, 85–87]. The code for the numerical modelling is a generalisation of equation 2.6, where the current-density has been replaced by $J = \frac{\partial P}{\partial t}$:

$$\frac{\partial E_{k_x,k_y}(\omega,z)}{\partial z} = ik_z E_{k_x,k_y}(\omega,z) + i\frac{\omega^2}{2\varepsilon_0 k_z c^2}\left(1+\frac{1}{\omega}\frac{\partial}{\partial t}\right)P_{k_x,k_y}(\omega,z) \tag{2.3.17}$$

where $k_z = \sqrt{\frac{\varepsilon(\omega)\omega^2}{c^2} - k_x^2 - k_y^2}$ is the longitudinal wave-vector, k_x and k_y are the transversal wave-vectors, and P is the nonlinear polarisation described by the following equation:

$$P_{k_x,k_y}(t) = \left[2n_2 I + \chi_{pl}(\rho) + i\frac{1}{k_z}\beta_K I^{K-1}\right]E_{k_x,k_y} \tag{2.3.18}$$

where $\chi_{pl}(\rho) = \frac{e^2}{m_e\varepsilon_0}\frac{1}{\omega_0^2 - i\omega_0/\tau_c}\rho$ is the plasma-induced susceptibility and $\beta^K = K\hbar\omega_0\sigma_K$ is the MPA cross-section. In the literature, we may find the MPI cross-section $[\sigma_K] = \frac{1}{s}\left(m^{2K-3}/W^K\right)$ or the MPA cross-section $[\beta_K] = \left(m^{2K-3}/W^{K-1}\right)$.

While the first term describes the Kerr effect, the second term introduces the plasma defocusing effect. Moreover, the third term is responsible for MPI induced losses. The equation 2.3.17 can be solved together with equation 2.3.16 and 2.3.18 to estimate filamentation in transparent bulk media.

Table 2.1 shows some of the parameters found in the literature to simulate filamentation in some of the most commonly used bulk materials such as YAG, Silicon, Sapphire and Fused silica. While Sapphire has a low nonlinear coefficient and high bandgap, Silicon has an extremely high nonlinear coefficient and low bandgap energy. The generated SPM and self-focusing effects are stronger at a larger nonlinear coefficient. Moreover, the generated plasma defocusing effects and MPI losses are weaker at higher bandgap values. Thus, we expect to achieve the weakest filamentation effects in Sapphire and the strongest effects in Silicon.

The features of the UPPE equations described above are shown in full 3D radial simulations in Figure 2.6. Filamentation in Sapphire, YAG, and Silicon has been

TABLE 2.1: Nonlinear and electron dynamic parameters for simulation of a filament and SPM in YAG, Si, Sapphire and fused silica.

	n_2 $(10^{-20}\ m^2/W)$	U_g (eV)	τ_c (fs)	ρ_{at} $(10^{28}\ m^{-3})$	σ_K $\left(\frac{1}{s}\left(m^{2K-3}/W^K\right)\right)$	K	Source
YAG	6.2	6.5	3	7	$4\ 10^{-83}$ (@ 0.8 μm)	5	[88]
YAG	6.2	6.5	3	7	$3\ 10^{-154}$ (@ 2.3 μm)	11	[89]
YAG	6.2	6.5	3	7	$2\ 10^{-181}$ (@ 3.2 μm)	11	*
Si	150	1.12	3.3	5	$3\ 10^{-7}$ (@ 2 μm)	3	[90]
Si	150	1.12	3.3	5	$9\ 10^{-39}$ (@ 3.2 μm)	3	*
Sapphire	3.2	9.9	1.2	28	$6\ 10^{-94}$ (@ 1 μm)	8	[91]
Sapphire	3.2	9.9	1.2	28	$2\ 10^{-245}$ (@ 3.2 μm)	15	*
Fused Silica	2.3	8.9	0.4	32	$1\ 10^{-83}$ (@ 0.8 μm)	5	[88]

* MPI coefficient values used in our simulations at 3.2 μm.

simulated using the parameters from Table 2.1 and pumped by 100 fs 3.2 μm intense pulses.

The cleanest process is predicted using the Sapphire medium. The filamentation process is weak, and the medium thickness's choice becomes not crucial.

YAG's nonlinear coefficient is double of Sapphire's, and the bandgap is still far from 3.2 μm. Thus, more substantial broadening and shorter pulse durations than in Sapphire are achieved. On the other hand, the proper crystal thickness choice becomes more crucial as the filamentation process is more sensitive than in Sapphire.

The zero-dispersion of Sapphire and YAG is at $\lambda_0 = 1.3$ μm and $\lambda_0 = 1.6$ μm, respectively. Thus, the filamentation process in Sapphire and YAG is carried out in the anomalous dispersion regime, where self-compression can occur. On the other hand, the zero-dispersion of Silicon is around $\lambda_0 = 19$ μm. Consequently,

the SPM process is carried out in the normal dispersion regime, inducing a pulse stretching effect.

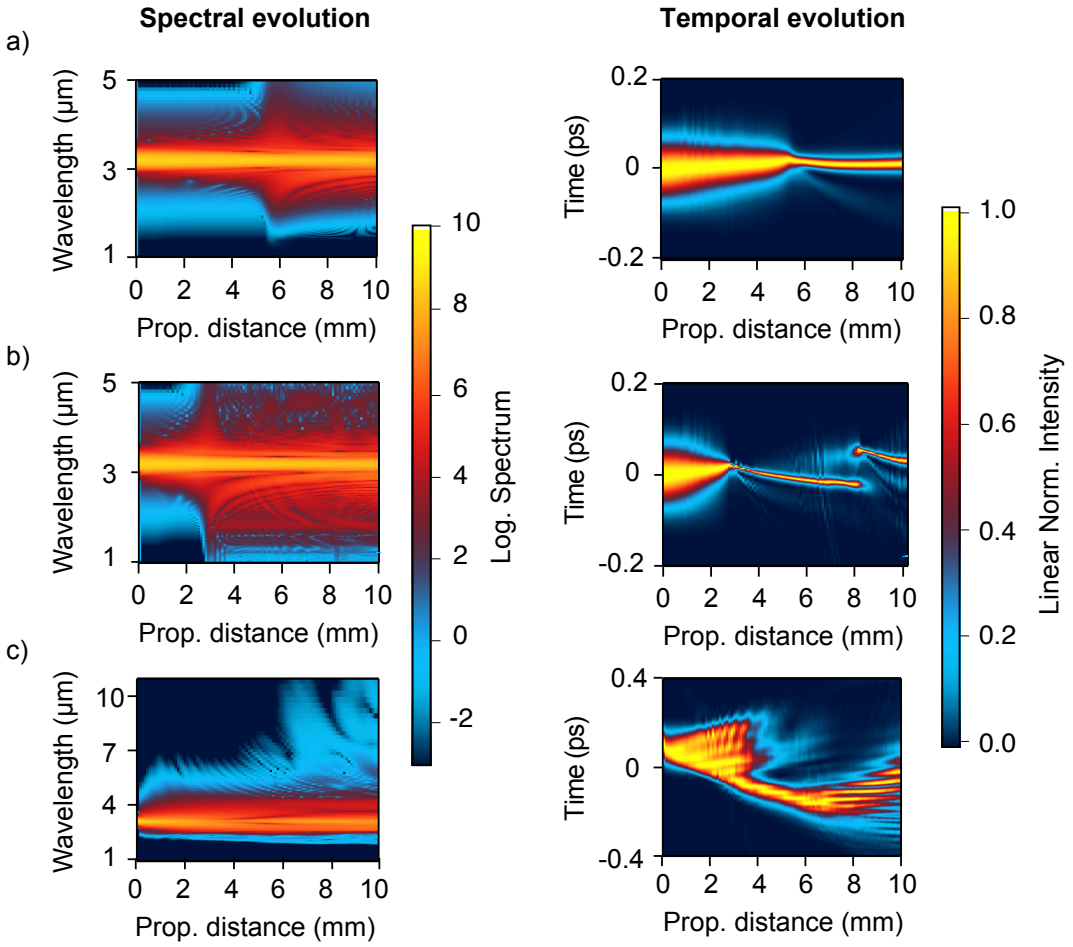

FIGURE 2.6: Complete 3D radial SPM and filamentation simulations for Sapphire (a), YAG (b) and Silicon (c) pumped by 3.22 μm 100 fs pulses. On the left side is shown the spectral evolution up to 10 mm of propagation distances through the filament. On the right side is shown the temporal evolution through the filament for the same propagation distances.

In Figure 2.7 is plotted the estimation of plasma generation during the filament (a), peak intensity variation (b), the pulse energy and transmission efficiency loss due to MPI effects (c), and the beam size through the medium (d).

In Silicon, the strong three-photon absorption effect compensates for the nonlinear effect from the beginning of the process, reducing the driving pulse's energy quickly. Only when the peak intensity is reduced significantly is the third-order nonlinear process triggered and filament generated.

The simulations on Sapphire are carried out for a few different MPI coefficients to simulate the variability on plasma generation, pulse peak-intensity predictions, energy loss and beam size during the filamentation process.

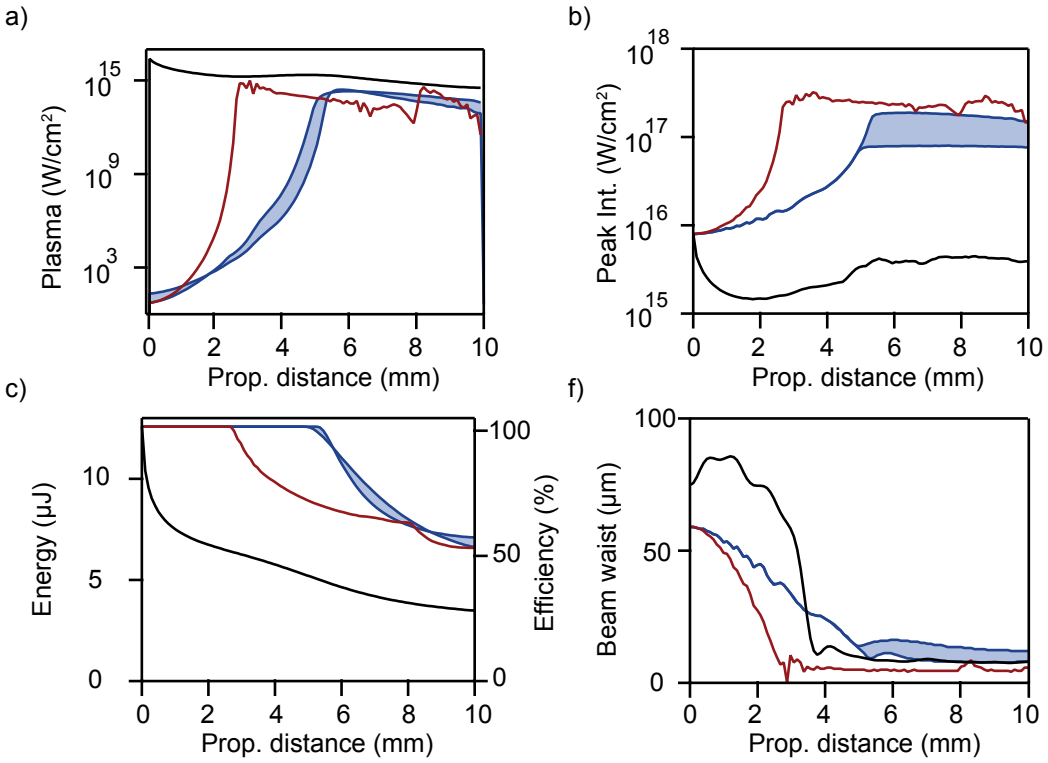

FIGURE 2.7: Nonlinear propagation predictions on plasma generation (a), pulse peak intensity (b), pulse energy (c) and beam waist radius (d) for Sapphire (blue line), YAG (red line) and Silicon (black line).

In conclusion, low bandgap and high peak intensities can induce transmission losses of up to 90% in the filament. Moreover, using a medium with negative dispersion can enable direct self-compression of the ultrashort pulses. Therefore, a medium with high bandgap energy and negative dispersion is required to achieve ultrashort pulses.

UPPE for gas-filled hollow-core fibre

Noble gases fulfil most of the requirements mentioned above to achieve intense ultrashort pulses. They show high ionisation potentials, the nonlinear coefficient varies with the pressure, and in the case of hollow-core fibres, the length can be tuned by tuning the fibre length. Moreover, while gases introduce positive dispersion in the visible and infrared regime, a proper design of the photonic crystals can tune the sign of the introduced effective dispersion [58, 92, 93].

The simulations for the nonlinear dynamics inside a noble gas-filled hollow-core fibre that are shown and used in this thesis were developed and compiled by our collaborators from MPL in Erlangen.

The nonlinear dynamics of an ultrashort mid-infrared pulse propagating in an ARR-PCF filled with a monatomic gas is simulated using the single-mode, UPPE [87, 94].

$$\frac{\partial E_0(\omega,z)}{\partial z} = ik_z\left(\beta(\omega) - \frac{\omega}{v_p} + i\frac{\alpha(\omega)}{2}\right)E_0(\omega,z) + i\frac{\omega^2}{2\varepsilon_0 k_z c^2}P_{NL}(\omega,z) \quad (2.3.19)$$

where $\beta(\omega)$ is the propagation constant of the fundamental LP_{01}-like core mode [95], v_p is the group velocity of the pump pulse and α is the frequency-dependent linear attenuation coefficient [96].

In equation 2.3.19 it has been taken into account $\frac{\partial P}{\partial t} = J$, introducing the plasma generation effects inside the P_{NL} term. Thus, without any further assumption, the nonlinear polarisation in the time domain can be defined as:

$$P_{NL}(z,t) = \varepsilon_0\chi^{(3)}|E(z,t)|^2 E(z,t) + \frac{I_p}{E(z,t)}\frac{\partial\rho(z,t)}{\partial t} + \frac{e^2}{m_e}\int_{-\infty}^{t}\rho(z,t')E(z,t')\,\mathrm{d}t' \quad (2.3.20)$$

where $chi^{(3)}$ is a pressure-dependent third-order susceptibility [97], I_p is the ionization potential of the corresponding gas, and ρ is the free electron density [98]. While the first term accounts for any instantaneous third-order nonlinear process, the second and third terms describe the contribution from MPI and plasma generation. In general, plasma effects driven by mid-infrared pulses can be weaker than in near-infrared or visible, thus being able to neglect plasma-related attenuation effects.

2.4 High harmonic generation in solids

Theory and experiments in high harmonics in solids (HHS) are still an exciting area of investigation due to the strong dependence on the crystallographic structure and the energy band structure [99–102]. This section introduces a classical and

quantum description of the HHS process to understand better the HHS results presented in Chapter 6.

The anharmonicity of the band enables generating harmonics in a solid. The electrons in the band oscillate with an anharmonic behaviour radiating at various harmonic orders of the fundamental frequency. In semiconductors, it is typical that when the sample is pumped with mid-infrared pulses, the electrons oscillate directly in the valence band via intra-band transitions or within the band. When shorter-wavelengths are used, inter-band transitions are more probable via multiphoton absorption and HHS produced between bands.

In the classical picture, we have assumed that HHS is generated only via intra-band transitions. Moreover, for simplification, the calculations assume a 1D periodic structure.

2.4.1 Classical view

The electron momentum in a crystal can be defined as $P = \hbar k$ where k is the position-independent electron wave-vector [103]. From a classical point of view, the electron acceleration and force can be described as $a(t) = -\frac{e}{m_e}E(t)$ and $\dot{P}(t) = -eE(t)$ respectively. Within the acceleration theorem [104], we assume that the electrons inside the crystal follow the momentum restricted by the crystal. Therefore, we can combine the electron momentum defined by the crystal with the electron acceleration induced by the electric field as follows:

$$\hbar k = -e \int_{-\infty}^{\infty} E(t)\,\mathrm{d}t \tag{2.4.1}$$

where k is the crystal momentum. Suppose we assume a monochromatic electric-field such as $E(t) = E_0 \cos(\omega_0 t)$ being E_0 the amplitude of the field and ω_0 the frequency. In that case, the wave-vector can be calculated for the initial condition $k(0) = 0$ as follows:

$$k(t) = -\frac{e}{\hbar} \int_{-\infty}^{\infty} E(t)\,\mathrm{d}t = \frac{eE_0}{\hbar\omega_0} \sin(\omega_0 t) \tag{2.4.2}$$

Moreover, the radiation generated can be described as $I_{rad}(t) \propto |a_{group}(t)|^2$ or in the frequency domain as $I_{rad}(\omega) \propto \left| \int_{-\infty}^{\infty} a_{group}(t)\, e^{-i\omega t} \mathrm{d}t \right|^2$. The equation can be

simplified using the integration by parts theorem (assuming $v_{group}(t) \to 0$ when $t \to \pm\infty$):

$$I_{rad}(\omega) \propto \left| i\omega \int_{-\infty}^{\infty} v_{group}(t)\, e^{-i\omega t} \mathrm{d}t \right|^2 = \left| i\omega v_{group}(\omega) \right|^2 \tag{2.4.3}$$

where $v_{group}(k) = \frac{\mathrm{d}\varepsilon(k)}{\mathrm{d}k}$ is the electron group velocity and $\varepsilon(k)$ the crystal energy band which describes the electron dispersion.

Cosine type energy bands

The energy band can be described as the sum of cosine bands if the electron contribution only from the s-level (in the tight-binding model) is considered [103].

$$\varepsilon(\boldsymbol{k}) = \varepsilon_s - \beta - \sum_{n,n}^{N} \gamma(\boldsymbol{R}) \cos(\boldsymbol{kR}) \tag{2.4.4}$$

where ε_s is the energy of the s-level, β is a constant and $\gamma(\boldsymbol{R})$ is the coupling between an atom and its nearest atom. In $1D$, the band structure could be further simplified to $\varepsilon(k) = \varepsilon_s - \beta - \Delta\cos(ka)$ where Δ is the amplitude of the bandgap and a the periodic distance between different atoms in the crystal. Thus, the electron group velocity can be directly defined as:

$$v_{group}(k) = \frac{\Delta a}{\hbar} \sin(ka) \tag{2.4.5}$$

The wave-vector in equation 2.4.5 can be replaced by equation 2.4.2 to define the electron group velocity dependent on the driving electric-field:

$$v_{group}(t) = \frac{\Delta a}{\hbar} \sin\left(\frac{\Omega_B}{\omega_0} \sin(\omega_0 t) \right) \tag{2.4.6}$$

where $\Omega_B = \frac{eE_0 a}{\hbar}$ can be defined as the Bloch frequency, which indicates the frequency of the electron oscillations. Thus, the generated radiation in the time domain acquires the following type of expression:

$$I_{rad}(t) \propto \left| \sin\left(\frac{\Omega_B}{\omega_0} \sin(\omega_0 t) \right) \right|^2 \tag{2.4.7}$$

When the electric field is small $\frac{\Omega_B}{\omega_0} \ll 1$, the first sin function can be approximated to $\frac{\Omega_B}{\omega_0}$, achieving the expected harmonic oscillation at the ω_0 centre frequency $I_{rad}(t) \propto \left|\frac{\Omega_B}{\omega_0} \sin(\omega_0 t)\right|^2$. When the amplitude of the electric field is increased such that $\frac{\Omega_B}{\omega_0} \approx 1$, then the expression $\left|\sin\left(\frac{\Omega_B}{\omega_0} \sin(\omega_0 t)\right)\right|^2$ can not be approximated but can be re-written as the sum of Bessel functions $\sum_{n=0}^{\infty} J_{2n+1}\left(\frac{\Omega_B}{\omega_0}\right) sin((2n+1)\omega_0 t)$. Thus, the possibility to generate even harmonics gets lost as we have chosen symmetric cosine type of bands. By replacing equation 2.4.6 in 2.4.3, the maximum radiated intensity of the odd harmonics $|\sin((2n+1)\omega_0 t)| = 1$ can be described as follows:

$$I_{rad}(N\omega_0) \propto \left|N\omega_0 J_N\left(\frac{\Omega_B}{\omega_0}\right)\right|^2 \tag{2.4.8}$$

Finally, when $\frac{\Omega_B}{\omega_0} \gg 1$, the second sin function, in equation 2.4.7, can be approximated to $\sin(\omega_0 t) \approx \omega_0 t$ and thus, harmonic radiation emitted at the Bloch frequency is achieved $I_{rad}(t) \propto |\sin(\Omega_B t)|^2$ [104].

2.4.2 Quantum view

From a quantum point of view, the first step is to find the Hamiltonian that describes the coupling between crystal momentum and electromagnetic-field.

The periodic potential in the crystal can be expressed as the sum of exponentials as follows:

$$V(\boldsymbol{r}) = \sum_{\boldsymbol{K}}^{\infty} V_{\boldsymbol{K}} e^{i\boldsymbol{K}\boldsymbol{r}} \tag{2.4.9}$$

where $\boldsymbol{K}$ is the vector of the reciprocal crystal lattice, $\boldsymbol{r}$ is the vector in the real crystalographic space and $V_{\boldsymbol{K}}$ is the coefficient that defines the periodic potential. In 1D, the equation 2.4.9 can be simplified to$V(x) = \sum_l^{\infty} V_l e^{iK_l x}$ where $K_l = \frac{2\pi l}{a}$ being a the distance between atoms in the 1D periodic structure. Moreover, the momentum induced by the periodic structure and the laser field can be written as follows:

$$P(x) = -i\hbar\partial x + \frac{e}{c}A(t) \tag{2.4.10}$$

where $A(t)$ is the vector-potential of the laser field. Thus, the Hamiltonian for the HHS process can be written by taking into account the periodic potential induced by the ions in the crystal (described in equation 2.4.9) and the total momentum described in 2.4.10:

$$H(x,t) = \frac{P^2}{2m_e} + V(x) = \frac{\left(-i\hbar\partial x + \frac{e}{c}A(t)\right)^2}{2m_e} + V(x) \tag{2.4.11}$$

Furthermore, the same Hamiltonian can be written in the reciprocal space:

$$H_{l,l'}(k,t) = \frac{\hbar^2}{2m_e}\left[\left(k + \frac{2\pi l}{a}\right) + \frac{e}{\hbar^2 c}A(t)\right]^2 + V_{l,l'} \tag{2.4.12}$$

which can be divided into two terms:

$$H_0 = \frac{\hbar^2}{2m_e}\left(k + \frac{2\pi l}{a}\right)^2 \delta_{l,l'} + V_{l,l'} \tag{2.4.13}$$

$$H_1 = \frac{e\hbar}{m_e c}A(t)\left(k + \frac{2\pi l}{a}\right)\delta_{l,l'} + \frac{e^2}{m_e c^2}A^2(t) \tag{2.4.14}$$

While H_0 describes the field free crystal energies, H_1 describes the coupling between the laser field and the crystal momentum. The first term of the Hamiltonian H_0 can be written as a matrix. The eigenvalues $E^0_{k,j}$ and eigenvectors $\Psi^0_{k,j,l}$ can be estimated diagonalising the $H_0 = H_{k,j}$ matrix. Then, the time-dependent wave-functions can be calculated from $E^0_{k,j}$ and $\Psi^0_{k,j,l}$ using the time-dependent perturbative theory:

$$\Psi_{k,j}(t,x) = \sum_{k',j'}^{\infty} \alpha^{k,j}_{k',j'}(t)\, e^{-i\left(E^0_{k',j'}\right)t/\hbar} \sum_{l}^{\infty} \Psi^0_{k',j',l} e^{i\left(k+\frac{2\pi l}{a}\right)x} \tag{2.4.15}$$

where $\alpha^{k,j}_{k',j'}$ can be calculated numerically by solving the following differential equation:

$$\dot{\alpha}_{k,j,j'}(t) = \sum_{j''}^{\infty}\sum_{l}^{\infty}\left\langle \Psi^0_{k,j',l}\left|H_1\right|\Psi^0_{k,j'',l}\right\rangle \alpha_{k,j,j''}(t) \left(\Psi^0_{k,j',l}\right)^* \Psi^0_{k,j'',l} e^{-i\left(E^0_{k,j''}-E^0_{k,j'}\right)t/\hbar} \quad (2.4.16)$$

and by substituting H_1 by the Hamiltonian described in equation 2.4.14:

$$\dot{\alpha}_{k,j,j'}(t) = \sum_{j''}^{\infty}\left[\frac{e^2}{2\hbar m_e}A^2(t)\,\delta_{j',j''} + \sum_{l}^{\infty}\frac{e}{m_e}A(t)\left(k+\frac{2\pi l}{a}\right)\right] \alpha_{k,j,j''}(t)\left(\Psi^0_{k,j',l}\right)^*\Psi^0_{k,j'',l}e^{-i\left(E^0_{k,j''}-E^0_{k,j'}\right)t/\hbar} \quad (2.4.17)$$

where j is the index for different bands and l is the contribution of $(l)^{th}$ neighbouring atoms. The induced electron-current can be calculated in the following way:

$$J(t) = \sum_{k,j}^{\infty} i\frac{e\hbar}{m_{eff}}\left\langle \Psi_{k,j}(t,x)\left|\partial x\right|\Psi_{k,j}(t,x)\right\rangle \quad (2.4.18)$$

Thus, by combining equations 2.4.10 and 2.4.12, the expression for the electron-current density is achieved based on the static eigenvalues and eigenvectors:

$$J(t) = -\sum_{k,j}^{\infty}\frac{e\hbar}{m_{eff}}\sum_{j',j''}^{\infty}\left(\alpha_{k,j,j'}(t)\right)^*\alpha_{k,j,j''}(t) \sum_{l}^{\infty}\left(\Psi^0_{k,j',l}\right)^*\Psi^0_{k,j'',l}\left(k+\frac{2\pi l}{a}\right) \quad (2.4.19)$$

The static energy bands ($E^0_{k,j}$) and wave-functions ($\Psi^0_{k,j,l}$) can be calculated by using codes, like QuantumEspresso [105], that uses density functional theory (DFT). The energy bands and wave-functions of semiconductors (ZnSe, Si, Ge etc.) can be calculated with high precision using more straightforward methods such as Tight-Binding, Orthogonalized Plane-wave method (OPW), or Pseudopotential theory [103].

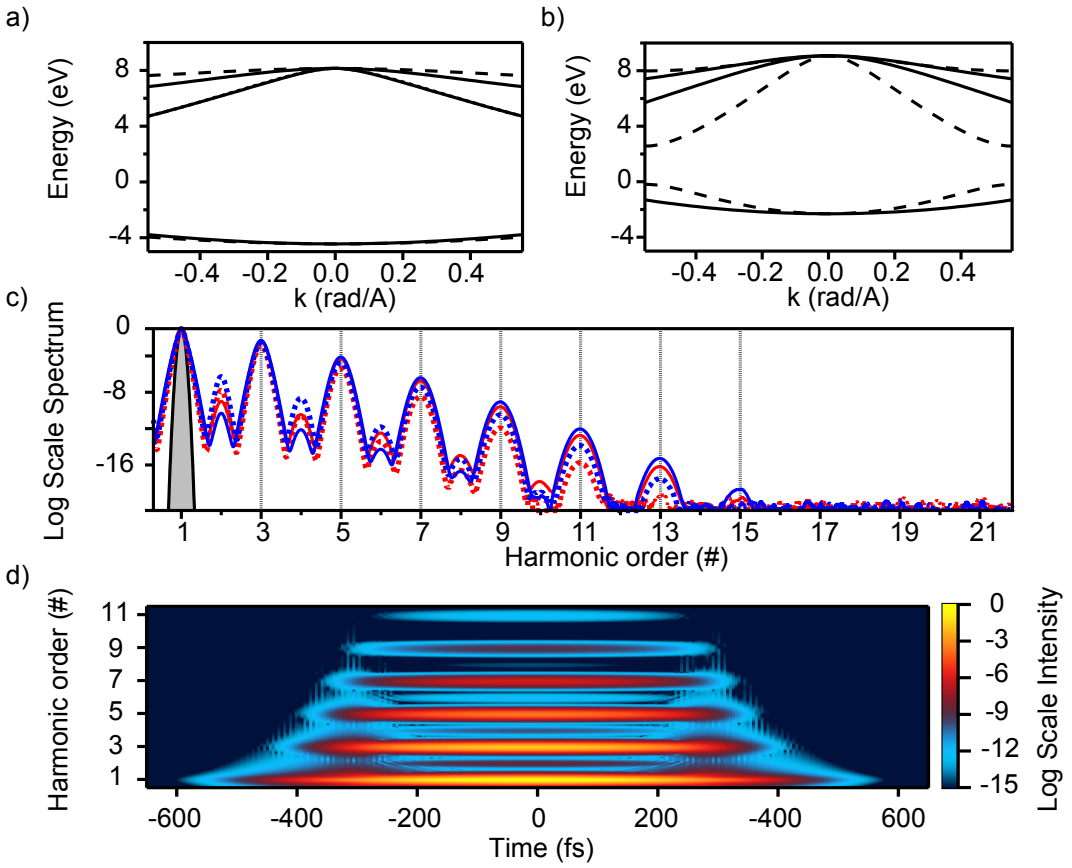

FIGURE 2.8: Band structure for ZnSe a) and Si b) for 100 (ΓX) in solid lines and 111 (ΓL) dashed lines. c) The simulated harmonic generation in ZnSe (red lines) and Si (blue lines) assuming a linearly polarised 100 fs mid-infrared pulse for 100 (solid lines) and 111 (dashed lines) cuts. The shadowed grey curve is the fundamental signal. d) Simulation of the high harmonic spectrogram for 100-cut ZnSe samples.

Finally, the harmonic spectrum generated driven by a laser field can be estimated using the following relation:

$$S(\omega) \propto \left| \omega \int_{-\infty}^{\infty} J(t)\, e^{-i\omega t} \mathrm{d}t \right|^2 \tag{2.4.20}$$

These equations enable the calculation of the high harmonics starting from a time-independent analysis for the energy bands and wave-functions in a laser field-free environment. The reason is that the DFT can be a time-consuming calculation for complicated solids.

Figure 2.8 shows the simulation of the high harmonics in ZnSe and Si pumped by a hypothetical 3.2 μm 100 fs pulses. The energy bands, displayed in (a) and

(b), and wave-functions are estimated using the pseudopotential theory, while the harmonics are calculated using the equations 2.4.19 and 2.4.20.

These simulations compare the HHS process in ZnSe and Si, for 100 (solid lines) and 111 (dashed lines) orientations, see Figure 2.8 (c). Even harmonics are shown to be enhanced by breaking the crystal symmetry using 111 orientation or rotating theta angle in 100-cut ZnSe (see appendix C) [106]. Moreover, the HHS spectrogram in (d) illustrates how the highest harmonics are generated only where the highest driving field amplitude is.

While for a qualitative understanding of harmonics, the equations above should be enough, for a quantitative calculation and propagation of the harmonics, the calculated electron-current density in equation 2.4.19 should be introduced in the wave propagation equation such as the one defined in equation 2.6.

Chapter 3

High-repetition-rate, bright, mid-infrared CEP-stable source

One of the coherent CEP-stable, broadband light sources developed during this thesis is the few-GW, near single-cycle, high-repetition-rate, mid-infrared OPCPA centred at 3.2 μm. The first version of the 3.2 μm high repetition rate OPCPA was published in 2009 [107] with specs reaching microjoule level energies (12.5 MW) at 100 kHz. The OPCPA was designed to be pumped by a 9 ps Nd: YVO_4 laser from Coherent, Inc. delivering 10 W at 100 kHz. Moreover, the system was sketched to be seeded by 3 μm pulses at 100 MHz generated via DFG from an electronically synchronised two-colour Erbium-doped fibre laser (Toptica Photonics AG) [26].

With the upgrade of the pump laser to 160 kHz and 60 W [108], and later to 100 W [23, 109], more OPCPA stages were added. Hundreds of MW peak powers were achieved, enabling filamentation in bulk [110] and strong-field studies [111, 112] driven by the mid-infrared laser. The first ultra-broadband mid-infrared supercontinuum generation [110] and self-compression [113] were achieved thanks to this upgrade. The broadband continuum generated via filamentation was also used to demonstrate the CEP stability of the OPCPA output. The visible part of the continuum was used via $f-2f$ interferometric measurement to characterise the fluctuations of the CEP [108].

Compared with standard high-energy systems running at $\sim$ 1 kHz, this system was built to counteract the unfavourable probability of the electron recombination process at long-wavelengths, required in most of the strong-field experiments. A clear example is the laser-induced electron diffraction (LIED) [114] which was

demonstrated to enable imaging of bond breaking in a single polyatomic molecule with 6 pm spatial and 0.6 fs temporal resolution [115], using this OPCPA.

When I started the PhD in 2016, my colleague and co-worker Matthias Baudisch had developed the last version of this OPCPA [116]. In this version, they had boosted the output energy up to 20 μJ (360 MW) at 160 kHz. Successful experiments in strong-field physics were demonstrated focusing the $\sim$ 100 MW mid-infrared pulses tightly.

On the other hand, higher peak powers were still required for coherent X-ray generation, and mid-infrared single-cycle generation for efficient isolated attosecond pulse generation remained unresolved. While filamentation was proved to enable self-compression in the mid-infrared regime, the reduced flexibility provided by the compression method limited to achieve shorter mid-infrared pulses. Furthermore, the generated plasma in the filamentation process induces above 50% losses, restricting the final pulse energy available for the experiments again.

At the beginning of my PhD, the main two unresolved requirements were the low efficiency of the OPCPA and the challenge to achieve an efficient generation of near-single cycle mid-infrared pulses. The OPCPA efficiency was mainly limited by the high losses the compression scheme at the system's back-end was introducing. The grating compressor used for the back-compression of the amplified pulses had an overall efficiency of $\sim$ 50%. The low efficiency of the gratings in the mid-infrared regime is due to the difficulty to find dielectric coatings providing broadband high transmissions/reflections with high damage thresholds in this regime. Thus, gold or aluminium coated gratings are generally used in the mid-infrared regime. The second limitation for an efficient OPCPA development was the low pump to idler conversion efficiency provided by the typically used PPLN crystal in this frequency range.

In this chapter, I expose how we overcame the limitations induced by the final compression grating, increased the conversion efficiency of the OPCPA stages and achieved efficient mid-infrared pulse compression to the single-cycle durations. The chapter is divided into three sections. In the first section, I expose my first year of PhD where Mathias Baudisch, Hugo Pires and I rebuilt the 3.2 μm OPCPA which was redesigned by Mathias and Hugo. The goal of the new design was to overcome the power limitations making use of the knowledge acquired in mid-infrared systems and nonlinear crystals during the last years [17, 49]. One of the main improvements we introduced was the implementation of a reflection-grating-based chirp-inverter in the middle of the OPCPA. The chirp-inverter enabled 1) back

compression in bulk with $> 90\%$ efficiency, 2) complete control on the stretching factor of the seed pulses.

The second improvement we implemented was to exchange PPLN based collinear OPA stages by bulk nonlinear crystals with non-collinear geometries in the last booster stages. For the first tentative, one of the previous booster stages was replaced by a bulk $KNbO_3$ crystal. This replacement reduced the green light generation and allowed the OPCPA stage to be pumped with higher pump peak intensities, achieving compressed powers up to 7 W (44 μJ) and 540 MW [117]. We also tried to compress the achieved high-power 3.2 μm pulses via the filamentation process using different nonlinear materials. Unfortunately, the best results were achieved using < 10 μJ pulse energies, losses above 70% were experienced, and pulse durations below 3-cycles were found to be inaccessible (or challenging). For more details, the investigations carried out in bulk self-compression are shown in the appendix B.

Later, following the results from [49], we replaced both final high-power stages by $KNbO_3$ bulk nonlinear crystals, increasing the efficiency of the last stages from 6.2% to 18.2% and achieving peak powers up to 1.35 GW [58].

In the second section, I show our results on efficient mid-infrared pulse compression to the single-cycle durations [58]. Firstly, I explain the properties of the novel ARR-PCF developed by the group of Prof. Dr Philip Russell in MPL. An exhaustive study of pulse compression in the ARR-PCF was conducted due to the lack of accurate mid-infrared medium parameters. This section shows the tests we tried to compress the pulses by filling the ARR-PCF with Helium, Neon and Argon. Thanks to the extremely high guiding properties provided by the ARR-PCF, we managed to overcome the second requirement to generate isolated attosecond pulses.

In the last section, I show the capabilities of the new soliton self-compression scheme using an optimised ARR-PCF at the output of the OPCPA. Here is demonstrated the generation of a dispersive wave (DW) in the UV range produced from the 3.2 μm pulses inside the ARR-PCF. Moreover, thanks to the tunability provided by the soliton generation scheme, here is shown an efficient generation of pulses with spectral content from 5 μm to 40 μm achieved via intra-pulse DFG (IP-DFG). The generation and characterisation of those pulses are shown for different mid-infrared nonlinear crystals, with a particular interest in the results

achieved in the newly developed BGGSe. Finally, I expose in this section a compact and straightforward scheme I have developed to generate a coherent multi-octave source expanding from 340 nm to 40 μm.

3.1 High-repetition-rate 3.2-μm OPCPA

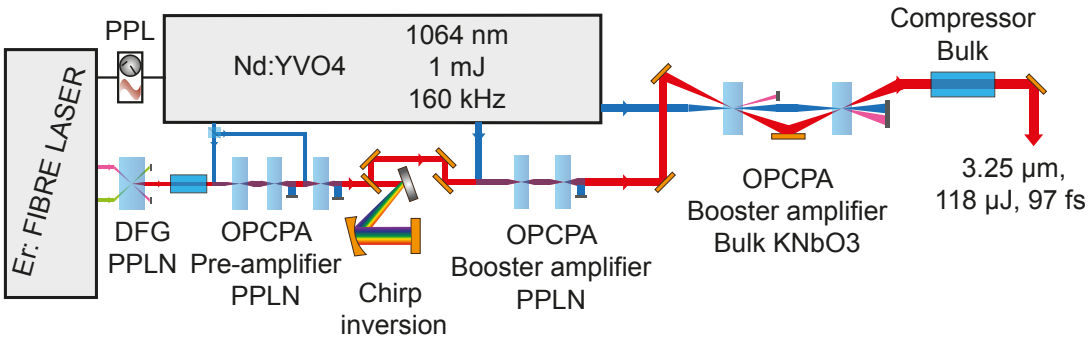

FIGURE 3.1: High power 3.2 μm OPCPA scheme. The mid-infrared pulses are generated from a two-colour fibre front-end combined with a DFG stage. The seed is synchronised with the pump via an electronic PPL system. Afterwards, the mid-infrared pulses are stretched and consecutively amplified in a pre-amplifier and booster amplifiers with an intermediate chirp-inversion stage. Finally, the 3.2 μm pulses are compressed in an AR-coated bulk sapphire rod.

Figure 3.1 shows the conceptual layout of the 3.2 μm OPCPA. Moreover, Table 3.1 shows the list of the nonlinear crystals used in the amplification stages. The CEP-stable mid-infrared pulses are generated from a two-colour Erbium-doped fibre laser via DFG process in a 1-mm-thin periodically poled lithium niobate (PPLN) crystal. Afterwards, the mid-infrared pulses are propagated through a 50-mm-long sapphire rod, stretching the pulses to 3 ps (negatively chirped), and pre-amplified in a chain of three consecutive PPLN based OPCPA stages up to 2.6 μJ. The pre-amplification stage has an overall pump to the idler conversion efficiency of 2.8%. A chirp-inverter is implemented to swap the direction of the chirp from negative to positive and further stretch the 3.2 μm pulses up to 7 ps. Longer seed pulses imply better temporal overlap between 3.2 μm pulses and the 1064 nm pump pulses, enabling higher amplification efficiencies in the booster amplifier. The first two amplification stages in the booster are again based on PPLN crystals achieving amplifications up to 18 μJ. The overall conversion efficiency is increased from 2.8% to 7.2% by increasing the seed pulse durations from 3 ps to 7 ps. The efficiency is still more remarkable in the final double non-collinear stage, which is based on $KNbO_3$ nonlinear crystals and exhibits a pump to the idler conversion efficiencies to 18.2% are achieved. Thus, the final power produced from the chain of

TABLE 3.1: Characteristics of the nonlinear crystals used in the OPCPA stages.

	Crystal	Coating	Length (mm)	Cutting angle	Aperture (mm^2)	Output energy	gain	Efficiency (%)
DFG	*MgO: Fan-out PPLN	AR: (1064 + 1600 +3200) nm	1	-	8.8x1	7 pJ		
OPA 1	*MgO: Fan-out PPLN	AR: (1064 + 1600 +3200) nm	1.4	-	8.8x1	25 nJ	$> 10^3$	0.08
OPA 2	*MgO: aPPLN	AR: (1064 + 1600 +3200) nm	5	-	3x2	500 nJ	20	1.5/1.6**
OPA 3	*MgO: aPPLN	AR: (1064 + 1600 +3200) nm	5	-	4x2	2.6 μJ	5.2	3.4/2.8**
Chirp-inverter						1.3 μJ		
OPA 4	*MgO: Fan-out PPLN	AR: (1064 + 1600 +3200) nm	1.4	-	8.8x2	10 μJ	7.7	2.8/2.5**
OPA 5	*MgO: Fan-out PPLN	AR: (1064 + 1600 +3200) nm	2	-	8.8x2	18 μJ	1.8	2.8/4.4**
OPA 6	Bulk $KNbO_3$	AR: (1064 + 1600 +3200) nm	1.82	40.5°	5x5	77 μJ	4.3	9.4/7.5**
OPA 7	Bulk $KNbO_3$	AR: (1064 + 1600 +3200) nm	2.33	40.5°	5x5	131 μJ	1.7	12.3/12.7**

* 5% magnesium oxide doped.

** The accumulative efficiency is calculated from the overall amplification and all the pump power used.

these seven stages is of 21 W (131 μJ). Moreover, the 3.2 μm pulses are efficiently compressed to 97 fs with compressed powers of 18.9 W (118 μJ) thanks to the high transmission efficiency of the anti-resonant (AR) coated 100 mm sapphire rod.

Table 3.1 shows the characteristics of the nonlinear crystals used in the OPCPA. The pump to the idler conversion efficiency in the OPCPA stages is conducted to compare the achieved efficiency using PPLN (around 3%) with the much higher efficiencies achieved using the nonlinear bulk $KNbO_3$ crystals. Moreover, with a star is shown the accumulative efficiency, which gives a view of the effectiveness of the stage. In general, the goal would be that the accumulative efficiency increases from stage to stage, ensuring that the pump is efficiently used. In our case, this is not fulfilled in OPCPA 4 due to the losses in the chirp-inversion scheme.

In the following subsections, I give a more detailed view of each part of the OPCPA: pump and seed lasers, synchronisation between both lasers, the pre-amplifier OPCPA, chirp-inverter, booster amplifier and the final compression and characterisation of the 3.2 μm pulses.

3.1.1 Erbium two-colour fibre seed laser

The two-colour Erbium fibre system is based on an Erbium-doped oscillator and a few Erbium and Ytterbium-doped fibre amplifiers running at 100 MHz from Toptica Photonics AG. After the 1550 nm pulses are generated and amplified, the pulses are split inside the system. While one arm is further amplified, the second arm is coupled to a solid-core photonic crystal fibre where a dispersive wave (DW) centred at 1050 nm is generated. The DW is compressed in a pair of prisms and separated from its supercontinuum in the Fourier plane. Finally, the 1050 nm pulses are further amplified in a ytterbium-doped fibre. The system delivers 220 mW at 1550 nm and few-milliWatts at 1050 nm with sub-100 fs pulse durations. Therefore, the phase of both colours is related and can be described using the equation 2.2.4. Thus, the CEP of the pulses generated via DFG between those two pulses is stable.

3.1.2 Nd: YVO_4, 160 kHz pump laser

The Nd: YVO_4 pump laser runs at 50 MHz. After the oscillator, the repetition rate of the 1064 nm pulses is reduced to 160 kHz using a Pockels cell and further amplified up to 40 W using three Nd: YVO_4 power amplifiers. The output is divided into three lines, one with 15 W and two with 12.5 W. The 15 W pump pulses are used to amplify the first three OPCPA stages in the pre-amplification section. One of the other two lines is further amplified to 50 W in a single Nd: YVO_4 power amplifier, and the last line is boosted up to 110 W in a chain of consecutive three Nd: YVO_4 power amplifiers. The second line delivering 50 W is used to amplify the first two OPCPA stages after the chirp-inverter, and the last line is used to pump the bulk non-collinear OPCPA stages based on the $KNbO_3$ crystals. Thus the overall available pump power for amplification reaches the 175 W (1.1 mJ).

At these power levels, proper management of heat is required. Thus, the pump laser is included in a water-cooled housing, ensuring high stability and low long term beam pointing drifts. This way, the power pump fluctuations are measured

to be around 0.3%, which later will enable high pulse-to-pulse stabilities for the 3.2 μm pulses.

3.1.3 Synchronisation of the pump and seed lasers

The temporal overlap between the 160 kHz pump pulses and the 100 MHz seed pulses is ensured via electronic phase-lock loop (PPL) synchronisation [118]. The pump laser is used as the master oscillator ($f_1 = 50$ MHz), and the cavity length of the Erbium oscillator ($f_2 = 100$ MHz) is tuned continuously to keep the frequency offset between both lasers close to zero ($\Delta f = f_2 - 2f_1$). For this purpose, the signal from the pump laser at 50 MHz is measured using a standard silicon photodiode. The electronic signal from the photodiode is frequency-doubled to 100 MHz. The f_2 signal is synchronised with the $2f_1$ signal using the electronic PPL synchronisation device. Thus, all the pulses from both laser oscillators are generated almost simultaneously, achieving temporal jitters between pump and seed pulses below 300 fs. As the pulse duration of the pump is 9 ps, these temporal fluctuations are around 3%.

While around 3% of temporal jitter was enough to keep the power fluctuations at the output of the OPCPA around 1%, for the most sensitive experiments (HHG, strong-field ionisation, multidimensional spectroscopy), better stability would be desirable. Thus, an optical synchronisation loop was inserted at the end of the pre-amplification stage. We monitor the temporal jitters translated in the OPCPA to the spectral fluctuations by exploiting the residual 1.6 μm signal taken from the third OPCPA stage and via SHG in 1 mm thick BBO. The spectrum of the 1.6 μm second harmonic is measured using a fast silicon-based grating spectrometer. While the spectrum shifts left or right, the seed pulses shift forward or backwards with respect to the pump pulses. As well as the signal spectrum fluctuates, the idler (3.2 μm seed) spectrum also fluctuates similarly but in the opposite spectral direction. The improvement of the spectral fluctuations of the signal via optical synchronisation improves the spectral fluctuations, and thus temporal, and power fluctuations of our CEP-stable 3.2 μm idler pulses are also improved. The optical synchronisation is possible thanks to the chirp introduced into the seed pulses for amplification in the OPCPA stages. The frequencies inside the seed pulses are spread in time; thus, depending on the temporal overlap between seed and pump pulses, different regions of the spectrum are amplified in the OPCPA process. This optical synchronisation enables reducing the pulse-to-pulse fluctuations down to 0.33% (see Figure 3.5 (c)).

3.1.4 Pre-amplifier OPCPA

The stretched (negative chirp) seed pulses are amplified in the pre-amplification section pumped by the mentioned 15 W coming out from the first pump line. The pre-amplification is carried out in three OPCPA stages. The first stage consists of an AR-coated 1.4-mm-long PPLN, and the rest are based on 5-mm-long AR-coated aPPLN crystals (HC Photonics). In the first amplification stage, the repetition rate of the 3.2 μm pulses is reduced from 100 MHz to 160 kHz as only one from 625 mid-infrared pulses is amplified. This stage is pumped by 5 W and provides a gain of $3.6 \cdot 10^3$ achieving powers up to 4 mW (25 nJ) at 3.2 μm.

As explained in chapter two and from Manley-Rowe relations, we can estimate that the power generated at the signal wavelength (1.6 μm) will be double. Thus, the output power of the pump after the first OPCPA stage is predicted to be around 4.988 W. In this first stage, the power of the pump pulses remain unvaried, and it is expected that they stay undeteriorated. Therefore, the pump pulses are recycled from the first OPA stage for the second stage. While building more OPCPA stages could suggest that a more complicated system is developed, the reality is that the recycling stages can compensate for the possible mismatches produced in the previous sections. Recycling the pump can improve the system's stability, allow gradual amplification and enable tailoring of the amplified spectrum.

The second stage is based on a 5 mm long aPPLN crystal, which is much longer than the 1.4 mm PPLN crystal used in the first stage. While the second stage gain ($\sim$ 20) is much lower than in the first stage, the pump to the idler conversion efficiency is higher (1.6%). Following the equation 2.2.26 the phase-matching bandwidth allowed by a 5 mm PPLN would be $\sim$ 1.9 times lower than the bandwidth allowed by the 1.4 mm PPLN used in the first OPCPA stage. Thus, an aPPLN crystal is used to achieve higher amplification efficiencies and maintain the phase-matching bandwidth.

The third OPCPA stage in the pre-amplification section is pumped with the remaining 10 W from the first pump line. The power of the 3.2 μm pulses is amplified up to 415 mW (2.6 μJ) using a second aPPLN crystal. While the OPCPA gain is now four times lower than in the second OPCPA, the conversion efficiency is $\sim$ 2.6 times higher.

The spectral evolution throughout the pre-amplification section is shown in Figure 3.2 The generated mid-infrared spectrum via DFG (shadowed grey) spans from 2.9 μm to 3.8 μm. The maximum peak of the DFG spectrum is around

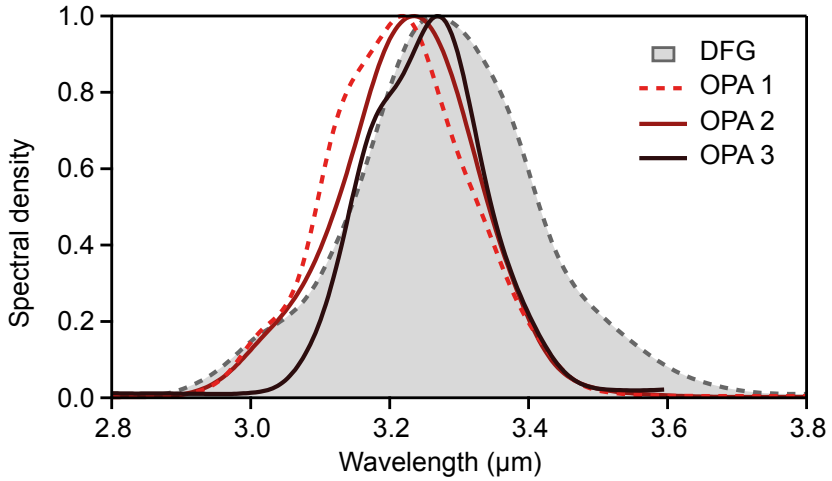

FIGURE 3.2: Spectral density of the generated 3.2 μm pulses via DFG and its evolution through the pre-amplification stages. In shadowed grey is shown the DFG spectrum. In dashed light-red is the OPA 1 spectrum. In solid curves are shown the spectrum from OPA 2 (red), and OPA 3 (dark-red).

3.28 μm and has a Voigt-type shape due to the interaction between the 1050 nm DW (Gaussian-shape) and the 1550 nm pulses (Lorentzian-shape). In the pre-amplification process, the bandwidth of the amplified spectrum is narrowed, and a more gaussian shape of the mid-infrared spectrum is achieved. Although aPPLN crystals are used for broader pulse amplification, the Gaussian temporal profile of the pump and the required chirp introduced to the seed pulses narrows the spectrum close to the maximum seed peak frequency.

3.1.5 Chirp-inverter

The efficiency of $\sim$ 2.8% achieved in the pre-amplification section can be improved by increasing the seed pulse duration. Historically, tunning the stretching factor of the seed pulses has been performed, replacing the length of the bulk rod. Unfortunately, longer are the seed pulses in the pre-amplifier, more are the frequencies inside the seed pulses separated; thus, narrower are the amplified pulses. The chirp-inverter installed after the pre-amplifier enables tuning the seed duration gradually while optimising the ratio between amplified power and spectral bandwidth. We optimised the seed duration to achieve the highest peak powers by comparing the amplified 3.2 μm energy at the end of the OPCPA with the transform-limited (TL) duration of the amplified pulses (see Figure 3.3).

The chirp-inversion stage is based on a Martinez-type stretcher with four passes in an aluminium coated reflection grating with 200 lines/mm and 17.5° of blaze

angle. An aluminium-coated cylindrical mirror with $f = 200$ mm is used for the imaging system on the Martinez stretcher. The cylindrical mirror is used instead of a typical spherical mirror to reduce the high-order phase distortions [119]. A flat gold-coated mirror is placed in the focal plane of the spatially chirped beam for back reflection to the cylindrical mirror and the grating. A dielectric high-reflection (HR) mirror with a D shape is used to make a second pass in the Martinez (to remove the spatial chirp). The Martinez stretcher has an overall efficiency of $\sim 48\%$, which reduces the available seed power for the next OPCPA stage to ~ 200 mW.

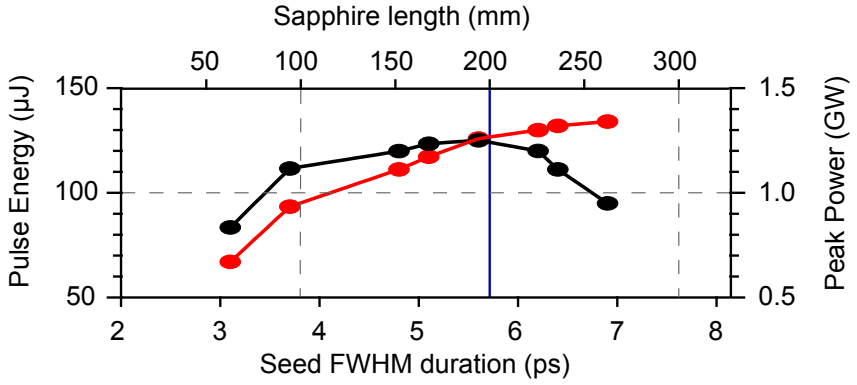

FIGURE 3.3: Amplified pulse energy (red) and achievable peak powers (black) as a function of the 3.2 μm stretched pulse duration after the OPA 7. The seed duration is tuned in the chirp-inverter. The top axis estimates the required sapphire rod length for back 3.2 μm compression.

Figure 3.3 shows the performed study to find optimum chirp-inverter settings. While the amplified energy increases continuously with the seed stretching factor, the peak power is optimised when the 3.2 μm pulses are stretched to $\sim$ 6 ps. The final pulse duration chosen in the chirp-inverter was determined by the round trips in the 50 mm long or 100 mm long sapphire rod, which was required for back compressing the 3.2 μm pulses. The top axis of Figure 3.3 shows the needed sapphire rod length to back compress the 3.2 μm pulses. The blue line represents the stretching factor of the 3.2 μm pulses chosen for our booster amplifier.

3.1.6 Booster-amplifier OPCPA

After the chirp-inverter, the $\sim$ 6 ps, 3.2 μm, 200 mW pulses are further amplified in a chain of four extra OPCPA stages. The first two stages are based on AR-coated PPLN crystals and pumped by the second pump line (50 W). While the pump is recycled from one stage to the other, these two stages increase the 3.2 μm

energy to 10 μJ and 18 μJ, respectively. Moreover, a slight non-collinear angle is introduced in these stages to avoid using mid-infrared dichroic optics and reduce the losses in the OPCPA system to the maximum.

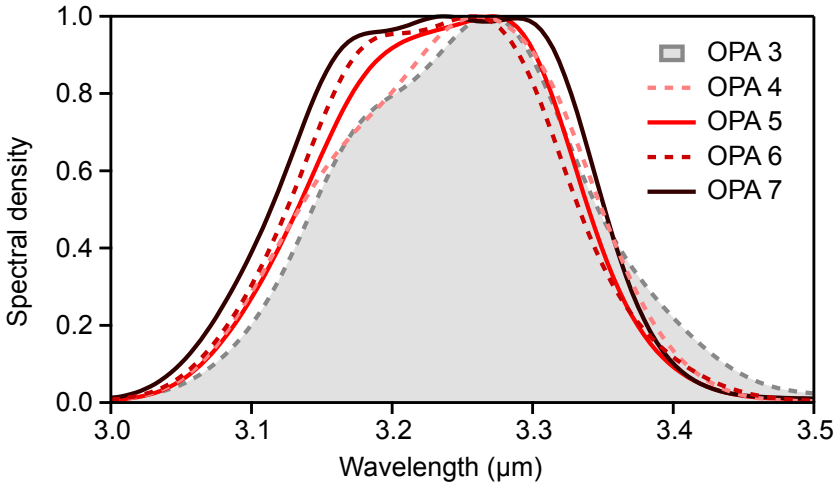

FIGURE 3.4: The spectrum measured of the mid-infrared seed for the booster-amplifier in shadowed grey together with the spectra from each booster OPCPA stages. With dashed lines are shown the stages pumped with undeteriorated pump pulses and in solid curves the spectrum measured from the recycling stages.

The last two booster stages are based on $KNbO_3$ bulk nonlinear crystals, and the third 100 W pump line pumps them. For broadband phase-matching, a non-collinear internal angle β between the pump and the idler of $\sim 5.2°$ is used (see *"Broadband phase-matching in non-collinear angle"* for details). The external non-collinear angle can be calculated using Snell's law: $\theta_{ext.} = \sinh\left[n_{bulk} \sin\left(\theta_{int.}\right)\right]$. Thus, the external non-collinear angle used in the OPCPA system for the last two booster stages is $\sim 10.7°$. The exceptional properties of $KNbO_3$ enable unprecedented amplifications to 77 μJ in the first OPCPA stage and to 131 μJ in the last stage.

The booster stages are designed such that thinner nonlinear crystals are used where the pump is undeteriorated (OPA 4 and OPA 6), and thicker crystals are used in the pump recycling stages (OPA 5 and OPA 7). This way, possible pump deteriorations are compensated using slightly longer nonlinear crystals. Consequently, 1.4 mm thick AR-coated PPLN is used in the OPA 4 and a 2 mm thick AR-coated sample in the following stage. For the AR-coated $KNbO_3$ based last OPCPA stages, a 1.82 mm thick nonlinear crystal is used in the OPA 6 stage, and a thicker 2.33 mm $KNbO_3$ is used in the final stage.

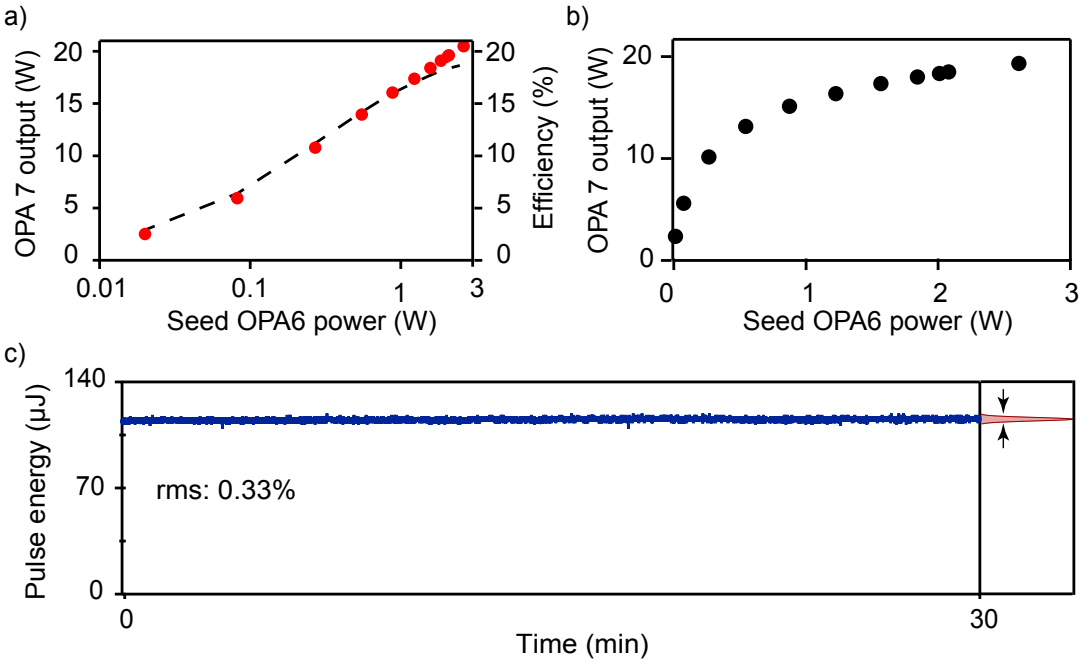

FIGURE 3.5: a) Output power from the OPCPA as a function of the seed power for OPA 6 (red dots). The overall efficiency of these last two stages is shown in dashed black lines. b) The saturation curve of OPA 6 + OPA 7 in linear scale. c) The pulse-to-pulse stability measurement over 30 minutes of the OPCPA output.

Figure 3.4 shows the amplified spectrum, stage by stage. In shadowed grey is presented the seed spectrum used for the booster amplifier generated in the third OPCPA stage. With dashed lines are shown the amplified spectra of the OPCPA stages where undeteriorated pumps are used (OPA 4 and OPA 6). With solid lines are displayed the spectra achieved from the recycling stages (OPA 5 and OPA 7). Moreover, as those stages are run in saturation, a broader amplified spectrum is achieved in every subsequent stage. That is why the spectral shape of the 3.2 μm pulses is converted from Gaussian to super-Gaussian.

Figure 3.5 shows the saturation of the last two KNbO3 based booster stages. As it is shown in Figure 3.5 (a) above 5 W of mid-infrared amplification is achieved by seeding the last stages with 100 mW of power (with less power than what is delivered from OPA 3). As it is shown in Figure 3.5 (b), above 1-2 W seed powers, the power saturation is achieved, and the rise of the output power is slowed down. In conclusion, more power than what is achieved in OPA 3 is required to make the best use of the pump power, which translates in extra stages (OPA 4 and OPA 5). Moreover, the saturation achieved in the booster stages enables the exceptional stabilities shown in Figure 3.5 (c).

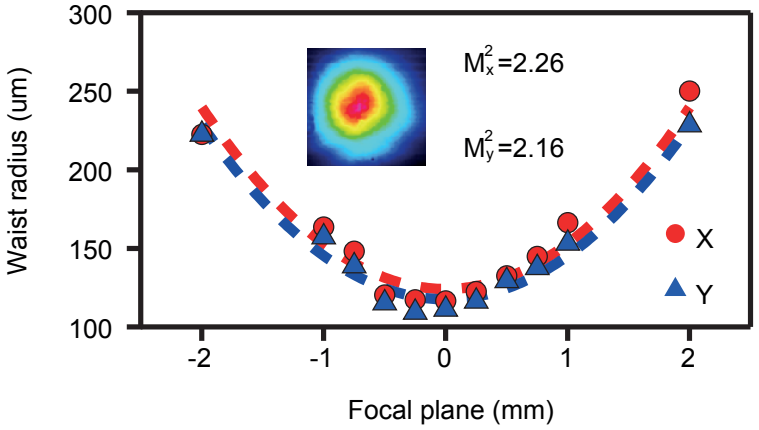

FIGURE 3.6: Beam quality measurement from the high power 21 W, 3.2 μm beam. The inset shows the output beam profile and the M^2 value for the vertical and horizontal directions.

Thanks to the high saturation provided by the last two booster stages, the 3.2 μm seed pulse fluctuation becomes negligible. Thus, the main contributions to the mid-infrared pulse instabilities are the pump variations ($\sim$ 0.3%) and the temporal jitter induced by the synchronisation between pump and seed lasers. The second effect is minimised by adding an optical synchronisation loop to the already existing electronic PPL synchronisation. Consequently, at full OPCPA power, the pulse-to-pulse fluctuations are reduced to 0.33%, measured over 30 minutes.

In Figure 3.6 is displayed the beam quality measurement of the 21 W, 3.2 μm beam at the output of the OPCPA. To focus the mid-infrared beam using an $f = 100$ mm off-axis gold-coated parabolic mirror is used. In the previous version, the last two stages were based on KNBO3 + PPLN and had a beam quality of $M^2 \approx 1.28$ [117]. The huge saturation level achieved converts the beam profile from Gaussian to super-Gaussian in this high power OPCPA version. Depending on the order of the super-Gaussian shape, the M^2 value also increases [82]. Thus, this mid-infrared OPCPA delivers super-Gaussian beam profiles with $M^2 \approx 2.20$.

3.1.7 Pulse compression in bulk

Thanks to the chirp-inversion stage, the amplified 3.2 μm pulses at the output of the OPCPA are back compressed in bulk. While the Martinez compressor has losses of 52% in bulk, the losses are reduced to the Fresnel reflections determined by the material. For instance, a Sapphire crystal shows Fresnel reflections of 6.8% per surface at 3.2 μm wavelength. Accordingly, in the case of a double pass scheme in an uncoated Sapphire rod, the losses would be reduced from 52% to

25%. To achieve efficient compression of our amplified 3.2 μm pulses, a 100 mm long Sapphire rod with AR-coating is used in a double-pass scheme. The silicon-based AR-coating reduces the losses per surface to 1.3%. Moreover, a concave $f = 1000$ mm aluminium mirror is used to collimate the 3.2 μm beam after the OPCPA and between the first and second pass of the Sapphire rod, achieving a final compression with an overall efficiency of 90%.

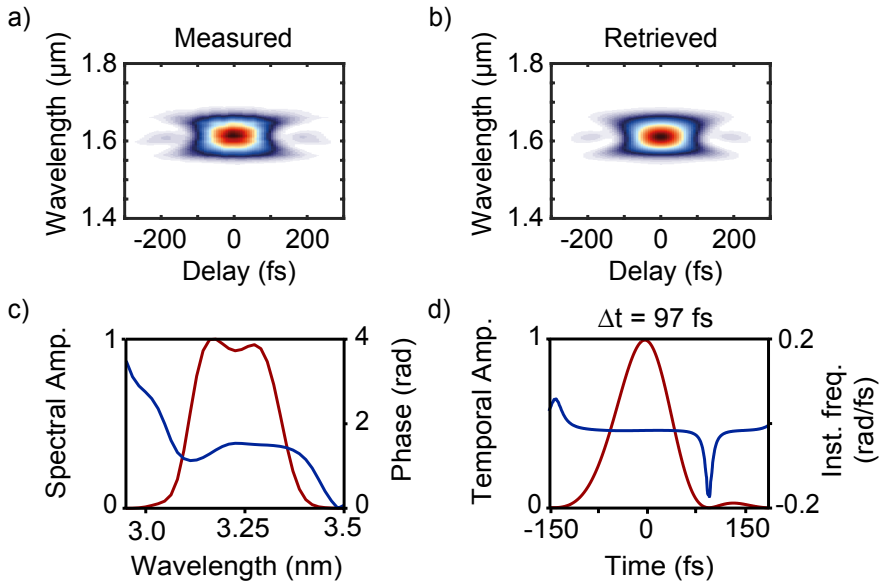

FIGURE 3.7: a) Measured SHG-FROG of the compressed 3.2 μm pulses. b) Retrieved SHG-FROG trace from which (c) spectral amplitude and phase and (d) temporal amplitude and instantaneous frequency are retrieved.

Figure 3.7 shows the pulse characterisation of the compressed 3.2 μm pulses. Pulse compression down to 97 fs is demonstrated being 95 fs the TL duration allowed by the amplified spectrum. The pulse characterisation is carried out using an SHG-FROG set-up using a 400 μm thick AGS nonlinear crystal (see appendix A for details). The FROG traces in Figure 3.7 (a) and (b) describe a pulse with a negligible amount of second-order chirp and a residual third-order chirp (cross-shape of the SHG-FROG trace). The compression bulk rod introduces the remaining third-order chirp, which could be only reduced by tuning the grating angle in the chirp-inversion stage. While third-order chirp could be reduced, the efficiency in the chirp-inversion stage would also decrease. Thus, the minimal third-order chirp is left in the 3.2 μm pulses.

3.2 Single-cycle mid-infrared pulse generation

As mentioned in the introduction chapter, near single-cycle pulses are required to achieve isolated attosecond pulses via HHG, instead of an X-ray burst every around 0.75 optical-cycles [7, 8]. Moreover, it is generally assumed that the strong-field processes are triggered only by field amplitudes above half of the maximum pulse intensities. Thus, the number of optical cycles is typically calculated for electric-field oscillations with amplitudes above half of the maximum pulse intensities:

$$\#\ optical\text{-}cycles = \frac{\Delta t_{FWHM}}{\lambda_c} c \tag{3.2.1}$$

where Δt_{FWHM} is the pulse duration of the pulses at λ_c, λ_c is the centre frequency of the ultrafast pulses, and c is the speed of light in vacuum. While the number of optical cycles of a propagating electric field is required to be more than one-optical-cycle, the above definition enables the generation of soliton transients with sub-cycle durations [68, 120]. This section demonstrates the generation of near-single-cycle pulses via soliton self-compression in a novel ARR-PCF.

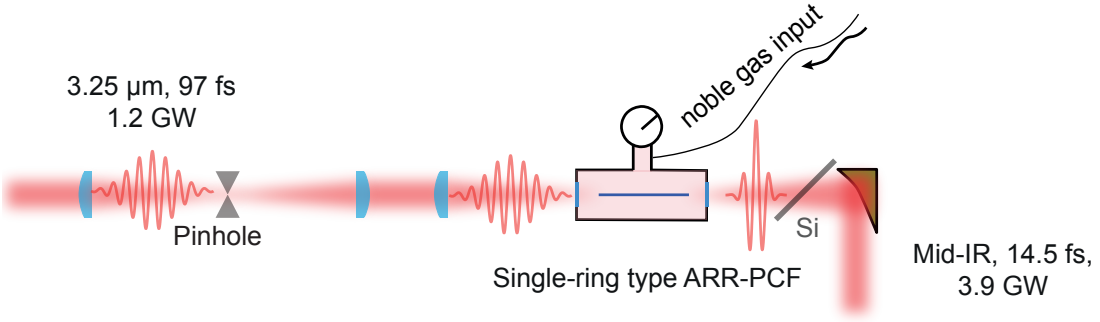

FIGURE 3.8: Schematic set-up of the soliton pulse compression in the ARR-PCF. The high-power mid-infrared beam is firstly introduced in a spatial filter and afterwards free-space-coupled into the ARR-PCF. The ARR-PCF is placed inside the high-pressure gas cell and clamped by two aluminium roof pieces. The input and output windows are based on 3 mm thick uncoated CaF_2 windows. The broadband compressed mid-infrared beam is collimated using an off-axis parabolic mirror.

Figure 3.8 shows the schematic design of the gas-cell, where the ARR-PCF sits and where the 3.2 μm, 97 fs pulses are coupled with coupling efficiencies above 90%. In the first design, a diamond based spatial filter was used as we did not know whether the ARR-PCF could be damaged due to possible spatial fluctuations and the high mid-infrared power. While spatial fluctuations were characterised to be minimal, the spatial filter was still maintained as the ARR-PCF is made of

fused silica thin rings with high absorptions above 2.7 μm. The spatial filter was based on an imaging system with plano-convex AR-coated lenses. The diamond pinhole was introduced in the focal plane to clean the 3.2 μm beam from possible imperfections. This scheme reduced the available mid-infrared power to 12 W (75 μJ) but prevented possible damages on the PCF surface. Afterwards, the beam in the pinhole plane was imaged into the input ARR-PCF surface. In the newer version shown in the following section *"Tunable bright multi-octave CEP-stable coherent source"*, the spatial filter is removed to increase the efficiency of the system, as both the pointing stability and beam quality of the OPCPA are excellent to couple without any risk the mid-infrared beam directly into the ARR-PCF.

The 3.2 μm beam is free-space coupled in the ARR-PCF using an AR-coated CaF_2 $f = 75$ mm plano-convex lens. The entrance and output windows of the gas-cell are based on 3 mm thick uncoated CaF_2 windows with an aperture size in the gas-cell of 10 mm. While the dispersion introduced by the plano-convex lenses and the input window can be neglected, the dispersion introduced by the output window $GDD^{CaF_2}_{(3mm)} \sim -400fs^2$, is enough to stretch the generated single-cycle pulses. Thus, a thin 0.5 mm silicon wafer $GDD^{Si}_{(0.5mm)} \sim 250fs^2$ at Brewster angle is used. A second silicon wafer could be used to reduce further the second-order dispersion. Still, due to the high third-order dispersion introduced by the silicon wafer, the final pulse duration would not be shortened.

Finally, the single-cycle mid-infrared pulses are collimated using an $f = 100$ mm gold-coated off-axis parabolic mirror.

3.2.1 ARR-PCF properties

The loss of a conventional gas-filled capillary scales as λ^2/a^3, where a is the fibre core radius. On the other hand, the characteristic length for SPM scales as $L_{SPM} = \lambda/(2\pi n_2 I_0)$ (shown in equation 2.3.4). Thus, the longer the centre wavelength of the pulse, the longer the capillary length required to achieve broadband pulses via SPM, but also larger the losses. Instead of increasing the fibre length, higher peak intensities can be used to achieve similar broadenings, obtained by decreasing the core size. Unfortunately, using smaller core sizes increases the losses again inside the capillary [121, 122]. Moreover, typically the capillaries are made from fused silica rods, which show high absorptions above 2.7 μm. Thus, until now, the use of a gas-filled hollow-core waveguide was not an option in the mid-infrared regime.

Figure 3.9 (a) shows a new type of ARR-PCF [122–125] developed to overcome the limitations mentioned above. The ARR-PCF consists of a single-ring based anti-resonant capillaries with $\sim$ 1.2 μm wall thickness, surrounded by an 88-μm central hollow core. In Figure 3.9 (b) in red is shown the measured losses of the new ARR-PCF in the mid-infrared regime. As can be seeing the newly designed ARR-PCF provides a loss-free window around 3.2 μm.

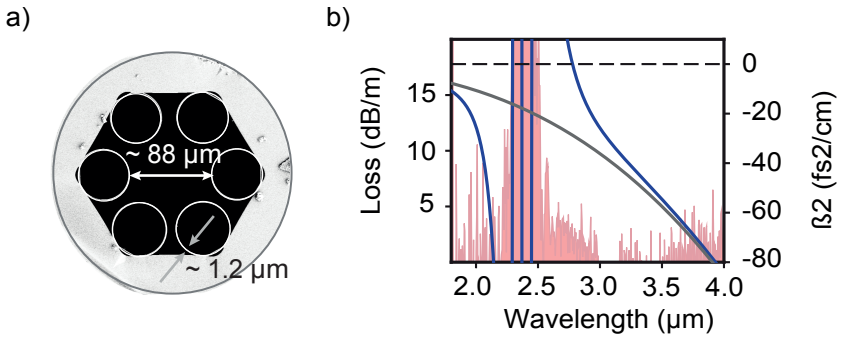

FIGURE 3.9: a) Scanning electron microscope image of the ARR-PCF fibre cleaved surface. b) Measured transmission loss in red together with the dispersion obtained via the Marcatili [126] model (grey) and fitting FEM calculations (blue) for an 88 μm core with 1.2 μm centre wall thickness, in vacuum.

Noble gases introduce positive dispersion in the visible and infrared regimes in free space. Still, proper management of the PCF design can change the sign of the dispersion. In Figure 3.9 (b) in grey is shown the curve of the dispersion estimated for this ARR-PCF using the Marcatili model [126]. This model does not take into account the effect of the anti-crossing resonance that appears around 2.4 μm. More precise calculations using the finite element method (FEM) are shown in blue [127, 128]. As can be seen, close to the resonance around 2.4 μm, the dispersion changes from negative to positive and goes exponentially to infinity.

Soliton self–compression is achieved when soliton-orders higher than one $N = L_d/L_{SPM} > 1$ are propagated inside the medium, where $L_d = T_0^2/\beta_2$ is the dispersion length, T_0 the input pulse duration (in our case 97 fs) and β_2 is the GVD [77, 129, 130]. For a given propagation distance $L \sim L_d/N$, the self-compression factor of the pulse increases with N. The required propagation distance to achieve a similar compression factor increases when higher-order dispersion terms become considerable. Thus, while pulse compression estimations using the Marcatili model would predict optimum compressions at shorter fibres, the more realistic dispersion calculations based on FEM would require longer fibres.

The sharp resonance around 2.4 μm was not only delaying the compression process but also required a medium with a higher nonlinear-coefficient. This effect

increased the challenge of achieving any significant compression in the ARR-PCF and pushed us to study the self-compression process in different noble gases. Moreover, the information available for the ionisation rates in noble gases were for the near-infrared regime (missing in the mid-infrared). As described in chapter 2 filamentation section, the ionisation-rate decreases with the multi-photon order. For instance, in Argon ($E_g = 15.8$ eV) the first MPI order at 1 μm would be 13 (similar to YAG for 3.2 μm), while at 3.2 μm the MPI order would be > 40. Consequently, the available ionisation rates were estimating strong plasma effects in Argon, forcing us to start our experiments using lighter gases like Neon or Helium.

3.2.2 Soliton generation in different noble gases

While the soliton-order increases and higher pulse compressions are achieved, higher-order dispersion terms become considerable. Since these higher-order terms can not be cancelled in the soliton generation process, the created frequencies close to the resonance are shifted in time to the pulse pedestal. Thus, the highest peak powers that can be achieved in the process are limited by the generation of a pedestal. To conclude, small values of the soliton-order ($N < 5$) and waveguides without resonances close to the input frequency are preferable to achieve a clean self-compression [130, 131].

To find the best compression using the gas-filled ARR-PCF, we studied the soliton generation and mid-infrared pulse self-compression in Helium ($E_g = 24.6$ eV), Neon ($E_g = 21.6$ eV) and Argon ($E_g = 15.8$ eV).

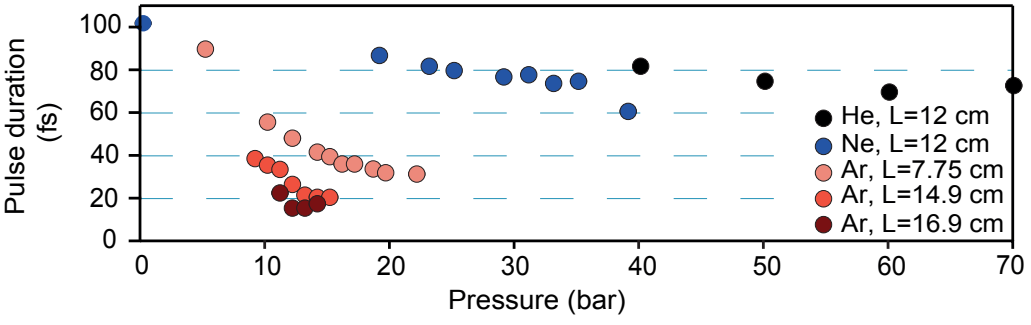

FIGURE 3.10: Measured soliton self-compression of mid-infrared pulses in the ARR-PCF, for Helium, Neon and Argon, in the function of the gas pressure inside the gas-cell.

In Figure 3.10 is shown the soliton generation of the 12 W, 97 fs, 3.2 μm pulses for Helium ($n_2^{Helium}(1bar) \sim 2{\cdot}10^{-23} m^2/W$), Neon ($n_2^{Neon}(1bar) \sim 3{\cdot}10^{-23} m^2/W$) and

Argon ($n_2^{Argon}(1bar) \sim 9{\cdot}10^{-23}m^2/W$) [97]. While the n_2 values were measured for 1 μm pulses, the uncertainty of these values is typically higher than the frequency dependency of n_2 [132, 133]. Moreover, the n_2 values at 1 bar of those noble-gases are three orders of magnitude lower than, for instance in YAG ($n_2^{YAG} \sim 6{\cdot}10^{-20}m^2/W$). Thus, to achieve efficient soliton generation higher pressures than 1 bar and longer propagation distances than in bulk-filamentation are used. While the nonlinear refractive index of the medium is expected to increase linear with the pressure in the gas-cell, the slope varies from one noble-gas to the other. For instance, the response to the pressure variations of Helium is much weaker than in Neon or Argon [134, 135].

As it is shown in Figure 3.10, pressures from 40 bars to 70 bars were required in Helium to achieve some manifestation of compression. As a result, pulse compressions down to 6 cycles (from 9 cycles) were achieved in Helium. Compression effects at higher pressures were not studied as this was the limit allowed by the CaF_2 windows before they could get damaged. In Neon, the compression started to manifest around 20 bars (7.2 cycles), but doubling the pressure did not improve excessively the final compression (5.5 cycles). For both gases, an ARR-PCF of 12 cm length was used.

In Argon, the first tests were carried out using a shorter fibre as high-ionisation effects were estimated. Pulse compressions down to 3-cycles were achieved using a 7.75 cm long ARR-PCF and pressures not higher than 20 bars. As can be seen in Figure 3.10, the compression dependency on Argon pressure is quite linear. Thus, we demonstrated using Argon that easy tuning and characterisation of the soliton process by just varying the Argon static pressure in the gas-cell can be achieved. While for some experiments, pulses as short as possible are required, to study the pulse duration dependency of some physical processes, it can be interesting to be able to tune the compression progressively.

Different fibre lengths were tested in Argon to achieve the optimum compression of our 3.2 μm pulses and at the highest powers. Firstly, to generate a broad enough spectrum, to enable single-cycle pulse durations, the ARR-PCF length was extended to 14.9 cm. With this fibre length, spectral broadening allowing single-cycle durations were achieved. Unfortunately, the soliton coming out from the fibre had residual second-order chirp, and thus, pulses not shorter than 1.8-cycle duration were measured (at 15 bar).

In Figure 3.11 can be seen how the soliton generation behaves when Argon pressure is varied in a 14.9 cm long ARR-PCF. As expected, the input pulse spectrum is

broadened when the pressure in the gas cell is increased. Moreover, the second-order dispersion is compensated in the soliton generation process. Thus close to TL durations are maintained while the spectrum broadens. At low soliton-orders (around 10-12 bar), the solitons are clean, but for higher pressures, a pedestal starts growing due to the uncompressed higher-order terms (14-15 bars). The clean pulses at 12 bars have a full-width half maximum (FWHM) duration of sub-3 cycles (30 fs), while sub-2 cycle (20 fs) pulse durations are achieved at 15 bars.

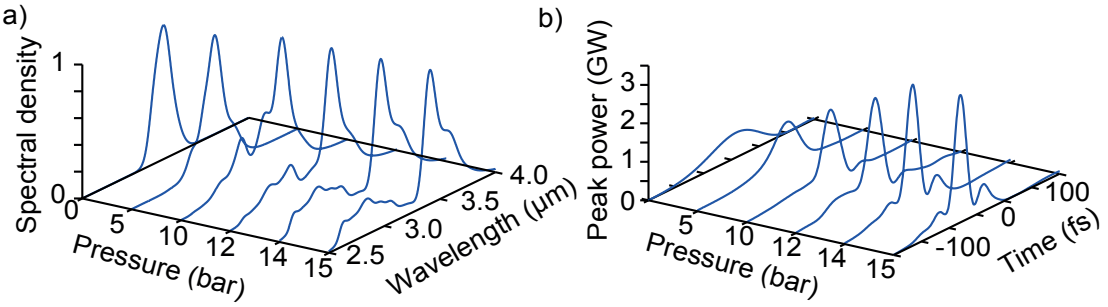

FIGURE 3.11: Evolution of the soliton compression at the output of a 14.9 cm long ARR-PCF as functions of the Argon pressure. (a) Measured spectra and (b) the corresponding temporal profile retrieved from the SHG-FROG measurements.

Once the SPM process is strong enough to generate single-cycle pulses, power-pressure tuning can vary the soliton dynamics and enable the required soliton at the output surface of the ARR-PCF. In our case, we wanted to achieve the optimum compression at the highest OPCPA powers; thus, instead of proceeding with a power-pressure tuning, the fibre length was again varied to reach the best compressions.

The best compression was achieved at 12 bars of Argon in a 16.9 cm long ARR-PCF pumped by 12 W of 3.2 μm pulses. From the 12 W, the actual mid-infrared power coupled and propagated inside the ARR-PCF was 10.1 W, due to the 6% loss in the uncoated input CaF_2 window, and 10% loss in the coupling process. After the output uncoated CaF_2 window 9.6 W and 14.5 fs duration mid-infrared pulses were measured using an all-reflective optics-based SHG-FROG (see appendix A for details).

Figure 3.11 shows the measured and retrieved SHG-FROG traces where the generated sum-frequency spectrum expanse from < 1.3 μm to > 2 μm. The broad sum-frequency measured was achieved thanks to the very thin 30 μm GaSe nonlinear crystal used for frequency doubling of the single-cycle 3.2 μm pulses. Moreover,

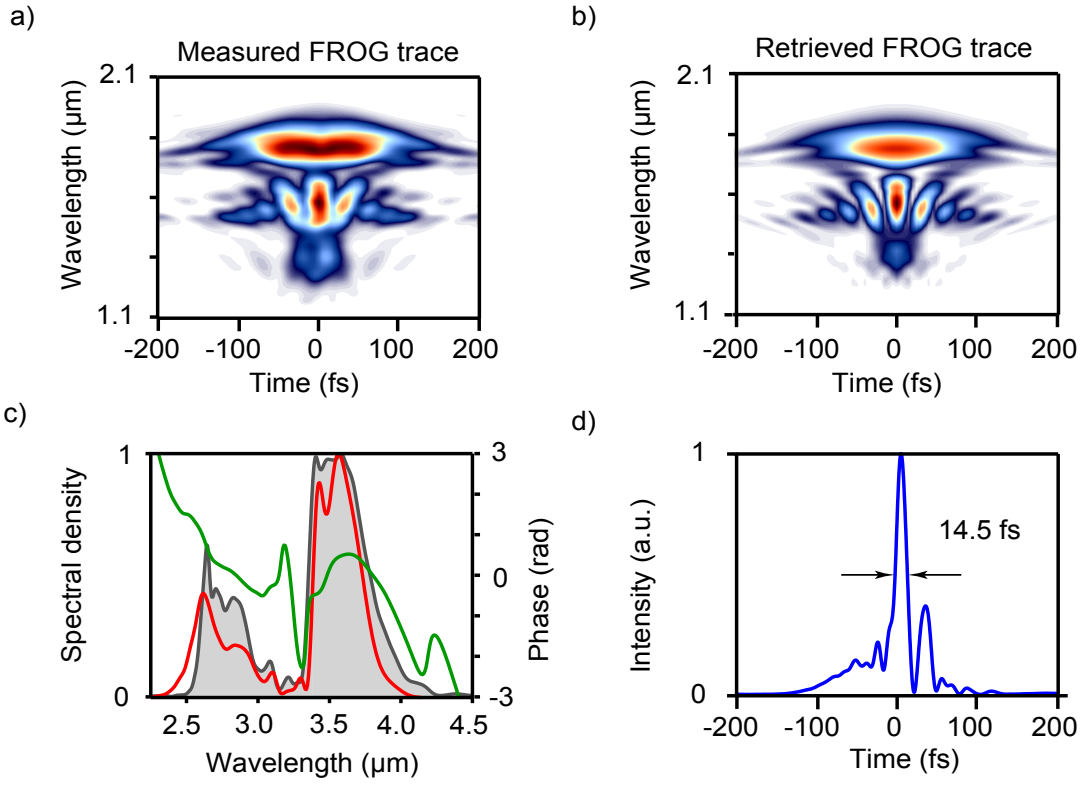

FIGURE 3.12: (a) Measured and (b) retrieved SHG-FROG traces of the single-cycle mid-infrared pulses. (c) Measured spectral density (shaded profile), spectral profile (red) and spectral phase (green) retrieved from the SHG-FROG trace. (d) Retrieved temporal profile (blue) and retrieved instantaneous frequency (red).

the small non-collinear geometry used in the SHG-FROG reduced the wavefront tilt of the broadband pulses in the nonlinear crystal enabling the precise characterisation of the single-cycle 3.2 μm pulses.

The retrieved spectrum (Figure 3.12 (c) red) matches quite well with the measured mid-infrared supercontinuum (Figure 3.12 (c) shadowed grey) expanding from 2.5 μm to 4.3 μm. Moreover, the front part of the pulse shows a pedestal induced by the uncompressed high-order dispersion terms and a post pulse generated typically from a high-order soliton break up.

This compression scheme is remarkably efficient, introducing only a 20% loss, which only 10% are induced by the coupling and guiding of the pulses through the ARR-PCF. The remaining losses are caused by Fresnel reflections in uncoated optics, which we decided to keep due to the difficulty to find broadband dispersion compensated AR/HR coatings in the mid-infrared regime. Nevertheless, we

demonstrated peak powers up to 3.9 GW using this scheme, which is a significant improvement compared with the maximum peak powers (0.36-GW) that the system could deliver before the OPCPA upgrade started in 2016.

3.3 Tunable, bright, multi-octave CEP-stable coherent source

In the previous section, we have demonstrated single-cycle pulse compression of the mid-infrared pulses at OPCPA full-power. In this section, new experiments using improved ARR-PCF are shown. As mentioned before, the ARR-PCF presented above presents a resonance around 2.4 μm. Thus, to achieve cleaner pulses or broader supercontinuum spectrum, a new ARR-PCF with a slightly larger hollow-core size (92 μm) and a new single-ring pattern was designed by our collaborators from MPL (see Figure 3.13 (a)). Interestingly, one of the characteristics of the anti-resonant-reflection PCF is how the resonance and the transmission window can be tuned by varying the wall thickness of the anti-resonant rings in the PCF. Thus, slightly changing the wall thickness, the collaborators from MPL managed to move the resonance from 2.4 μm to around 1.8 μm.

In this section are exposed our efforts to achieve ultra-broadband compressed pulses from UV to the THz regime, generated to be used for different multi-dimensional pump-probe spectroscopic studies (see Fig 1.1 for possible studies). For pump-probe experiments, it is typical to require a few optically synchronised beams [116]. Thus, a reduced amount of power is coupled into the ARR-PCF to achieve the soliton compressed ultra-broadband pulses and save power from the OPCPA for extra beams that the experiment could require.

In Figure 3.13 (b) is shown the soliton compression process using a 20-cm-long ARR-PCF and driven by only 2.8 W of 3.2 μm power from the OPCPA. Thanks to the resonance being shifted to shorter wavelengths, the required power to achieve significant compression is reduced, and more freedom in the pulse compression is achieved. In this fibre, coupling and guiding efficiencies up to 93% are achieved. Moreover, the spatial filter is removed from the set-up thanks to the excellent beam quality of the 3.2 μm pulses.

As can be seen in Figure 3.13 (b) and (c), while the first broadband short pulses are achieved at 25 bars of Argon pressure in the gas-cell, the pulses keep broadening and solitons propagating at higher pressures. The simulations shown in

the *" High-brightness seven-octave carrier-envelope phase-stable light source"* Nature Photonics publication [68] corroborate that the maximum peak powers inside the ARR-PCF are achieved around 30 bars of Argon pressures in the gas-cell. However, such a broadband pulse achieved at 30 bars is so sensitive from any dispersion, collimation and characterisation scheme that some frequencies are lost in space or time (see Figure 3.13 (c)).

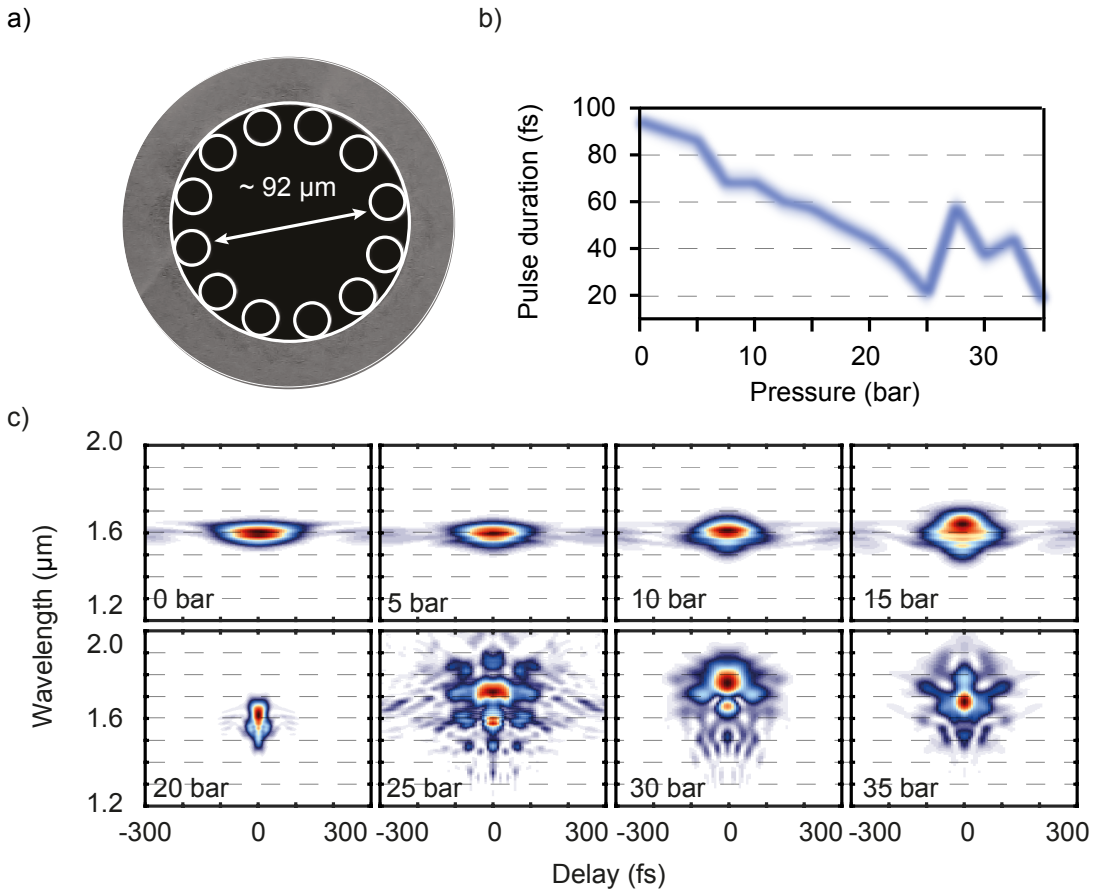

FIGURE 3.13: a) Scanning electron microscope image of the new ARR-PCF. b) Retrieved pulse durations of the compressed 3.2 μm pulses at different Argon pressures inside the gas-cell. c) Pressure scan of the measured SHG-FROG traces at the output of the gas cell.

In the following two sections are presented two results based on the prospects provided by the ARR-PCF. From one side, an ultraviolet DW generation in the soliton compression process, which is only generated when the highest-peak-powers are achieved inside the PCF. From the other side, we have used these broadband compressed pulses to drive the IP-DFG process to generate pulses above 10 μm.

While for the DW generation pulses as short as possible are required inside the ARR-PCF, for the IP-DFG process, clean ultrashort and broadband pulses that

can be propagated in dispersive media are needed. The shown SHG-FROG traces in Figure 3.13 (c) give an overview of the temporal-spectral disposition provided by the compressed mid-infrared pulses.

In the standard DFG process driven by two independent pulses, the generated DFG depends on the frequency separation between the pump and signal pulses. DFG centred at shorter wavelengths will be achieved when larger is the separation of the pump and signal centre wavelength. Similarly, in IP-DFG, higher frequencies will be generated when the driving pulse is broader. While at 20 bars or 35 bars, only long wavelengths can be generated via IP-DFG, around 25 bars, a really broad spectrum with few different spectral peaks is achieved from the ARR-PCF output. At this regime difference frequency mixing between 2.7 μm, 2.9 μm, 3.2 μm, 3.5 μm, and 3.7 μm peaks can be efficiently produced in the IP-DFG process. Thus, it is expected that using the pulses compressed around 25 bars, ultra-broadband pulses from IP-DFG are generated.

3.3.1 Dispersive wave in the UV

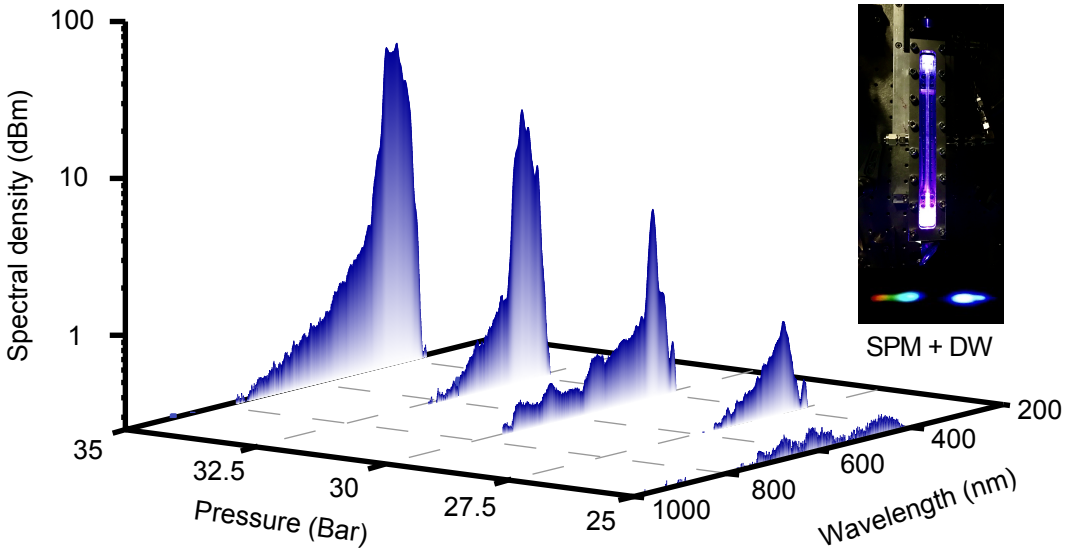

FIGURE 3.14: Evolution of the UV DW generation in the ARR-PCF driven by the 2.8 W, 3.2 μm pulses. The inset shows the gas-cell where the ARR-PCF sits, and all the generated scattered white light in the SPM + DW process. Also shown in the inset the beam profile of DW and the visible SPM part.

The DW can be generated in the soliton compression process when high peak powers are achieved in the process [136]. During the last years, a particular interest in generating few-femtosecond UV pulses grew. A proof of this is the different

publications where they have tried to optimise the DW generation using gas-filled hollow-core fibres [137], or PCFs [138, 139]. Until now, the DW in the UV range was generated by driving the process with 800 nm to 1.6 μm high energy pulses, achieving conversion efficiencies up to 5% [138]. As we knew that high-peak powers were produced inside our ARR-PCF, we decided to study the DW generation in the UV regime driven by our 3.2 μm pulses to expand the radiation down to the ultraviolet regime.

Moreover, these DW pulses are typically generated at the fibre's end. Thus, the UV pulses are generally compressed, providing pulse durations at FWHM down to a few femtoseconds. Therefore, this technique of expanding the spectrum to the UV provides spectral content in this regime and produces coherent pulses that can later be used in a pump-probe scheme for pumping different physical processes. As have been mentioned in the introduction chapter, some of these processes can be the ionisation of molecules like trans-azobenzene [140] pumped around 340 nm or the study of excitons in hexagonal boron nitrate (HBN) pumped by 200 nm pulses [141].

Figure 3.14 shows the emergence of the DW starting around 27 bars and raising with the Argon pressure in the gas-cell up to 35 bars. The maximum DW power achieved is at 35 bars, at a bit higher pressures than where the 3.2 μm pulses are maximally compressed inside the ARR-PCF (around 30 bars). At 35 bars up to 4 mW (25 nJ) of average power are achieved with conversion efficiencies up to 0.17%.

One of the possible reasons for the low conversion efficiency of the DW generation is the possible higher-order resonances that the ARR-PCF presents. As can be seen in Figure 3.15, the first resonance of the ARR-PCF is around 1.8 μm. When the supercontinuum reaches the resonance wavelength, that part of the spectrum is absorbed (Figure 3.15 red arrow) and emitted (Figure 3.15 green arrow). It is expected that at lower wavelengths, higher-order resonances of this first resonance around 1.8 μm appear. Thus, few resonances in the UV regime would absorb the generated DW and limit achieving higher conversion efficiencies.

The dispersion of the typical Kagome PCF driven by near-infrared pulses can be easily tuned by varying the pressure inside the gas cell and, thus, tailoring the centre wavelength of the generated DW. Unfortunately, the dispersion introduced by our ARR-PCF is much flatter, and the pressure dependency of the DW centre wavelength is much weaker. Thus, it is much more challenging to tailor the DW and avoid the ARR-PCF resonances.

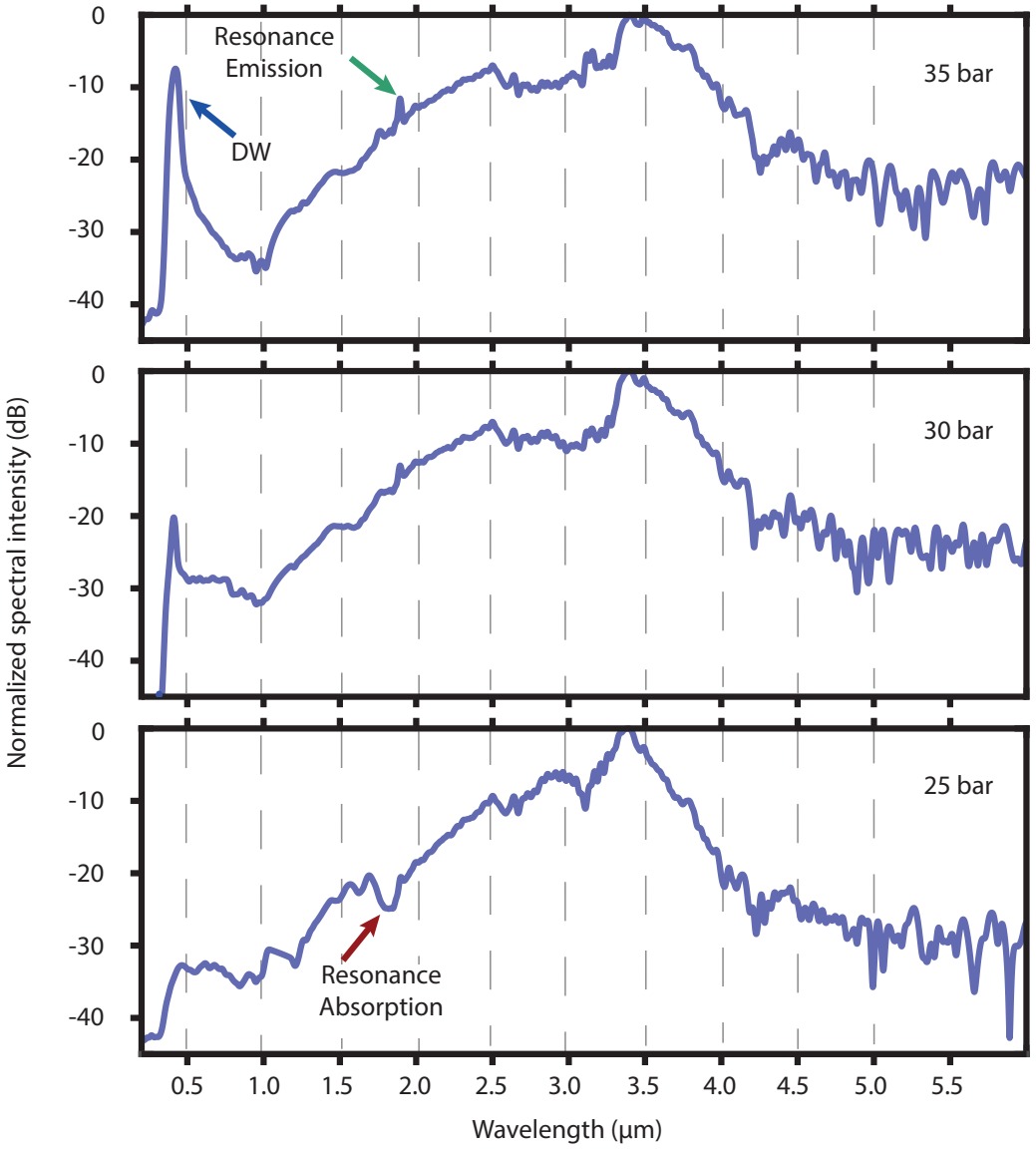

FIGURE 3.15: Measured normalised spectral intensity of the ARR-PCF output at 25 bars, 30 bars and 35 bars.

The beam profile of the DW after a MgF_2 prism is shown in the inset of Figure 3.14, where a clear gap between the generated SPM form 3.2 μm and the DW is visible in the picture. This gap is the fingerprint of a clean DW generation without spectral overlap with the main SPM. Moreover, as the divergence of the DW is almost an order of magnitude smaller than the fundamental 3.2 μm pulses, the DW can be propagated for long distances without the need of using a collimating mirror.

In Figure 3.15 is shown the measured ultra-broadband spectrum generated inside the ARR-PCF and concluded by an SPM expanding from 0.5 μm to 5 μm and a

TABLE 3.2: Estimated pulse duration of a UV pulse at the output of the gas-cell for different DW centre wavelengths and TL durations.

Centre Wavelength (nm)	TL Duration (fs)	Bandwidth (nm)	GDD (fs^2)	FWHM duration (fs)
400	10	23	202	57
	2	117		280
350	10	18	202	68
	2	90		338
300	10	13	202	87
	2	66		430
250	10	9	202	120
	2	46		600
200	10	6	202	200
	2	30		1000

DW generated between 340 nm to 450 nm.

The pulse duration dependency in Argon pressure of the 3.2 μm SPM has been shown in Figure 3.13. While outside of the gas-cell, the FWHM duration of the mid-infrared pulses is limited to the single-cycle duration regime, the simulations carried out by our collaborators from MPL, estimated 3.2 μm pulse durations inside the ARR-PCF down to 3.5 fs [68, 120]. The simulations show extreme ultrafast nonlinear dynamics where an optical-shock-wave couples with the soliton, steepening the tail of the pulse so strongly that soliton transients with optical cycles at FWHM down to 0.32 are generated (see Figure 2 (c) in [68]). Unfortunately, these soliton transients stretch so quickly that only in vacuum could they be measured and used. For instance, an output-window-free gas-cell with differential-pressure-pumping connected to a vacuum chamber would be required to propagate the soliton transients. Moreover, the streaking technique could be used to measure the dispersion-free pulses [142].

Similarly, while it is expected that the DW should also be compressed close to its TL duration of 7 fs (4.8 optical-cycles), we did not have the chance to characterise the pulses. With the compression of the UV pulses, extra care is required as those pulses are generally more sensitive to the dispersion introduced by the propagating medium. Moreover, the shorter the DW pulses' TL duration (or shorter the centre wavelength), the higher the temporal stretching introduced by any dispersive optic. In Table 3.2 is shown how the 3 mm CaF_2 window would stretch the UV pulses with different TL durations.

Table 3.2 shows how challenging it can be to keep an ultrafast UV pulse compressed when it is propagated through different dispersive optics. In the extreme case of 200 nm UV pulses, any small dispersion is enough to stretch the pulses to the picosecond regime. Luckily, in our case, with a centre wavelength around 415 nm and 7 fs TL duration, the generated DW pulses would be expected to be still compressed below 80 fs at the output of the gas-cell.

3.3.2 Intra-pulse differential frequency generation

In this section is demonstrated the expansion of the 3.2 μm compressed pulses up to 40 μm. For this purpose, IP-DFG in different nonlinear mid-infrared crystals is studied. In general, while some nonlinear crystals like GaSe show broadband phase-matching and transmission window, the conversion efficiency can be moderate. On the other hand, in nonlinear crystals like ZGP or CSP with a strong figure of merit (see Figure 1.3), high conversion efficiencies can be achieved. Still, in ZGP, the bandwidth is limited due to the transmission window restricted above 12 μm. In the case of CSP, the transmission window is even more restrictive, absorbing above 9 μm. Different nonlinear crystals are generally swapped to tune the IP-DFG depending on the power required by the experiment or the demanded wavelength range. Switching between various nonlinear crystals can be tedious as all the following will be misaligned, and a from-scratch alignment and temporal-spatial characterisation will be required. The IP-DFG driven by our 3.2 μm solitons, generated in the ARR-PCF, have been tested in GaSe, ZGP and a new mid-infrared nonlinear crystal called BGGSe. BGGSe is acquired from our collaborator Dr Valentin Petrov and shows a high figure of merit (like ZGP). BGGSe can be AR coated, unlike GaSe, and unlike most of the mid-infrared nonlinear crystals, its transmission window expands from the visible regime to $>$ 20 μm

(see Figure 3.18). Finally, BGGSe provides a flat dispersion relation in the mid-infrared regime ($v_p \approx v_s \approx v_i$), implying that ultra-broadband phase-matchings should be achieved.

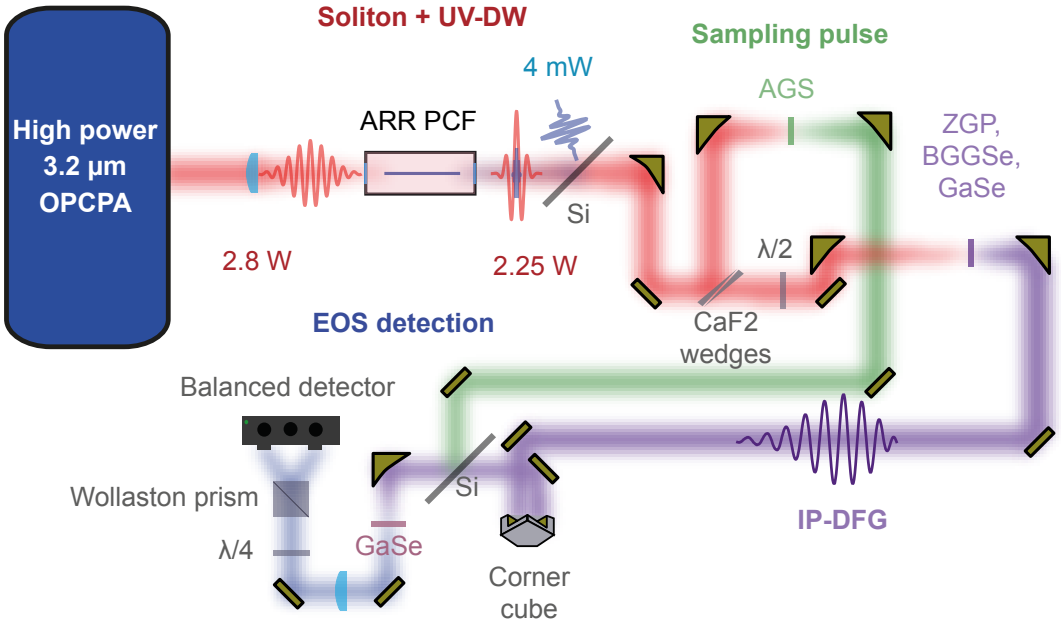

FIGURE 3.16: Schematic layout of the tuneable multi-octave source. 15% of the OPCPA output power is coupled into the ARR-PCF to generate a coherent and compressed supercontinuum from 340 nm to 5 μm. Afterwards, from the ARR-PCF output,1.35 W are used to extend the radiation to 40 μm via IP-DFG in different mid-infrared nonlinear crystals. The IP-DFG pulses are characterised via EOS using sampling pulses generated from the ARR-PCF. The sampling pulses are achieved via SHG in AGS.

Figure 3.16 shows the schematic set-up of the 3.2 μm compression, DW generation, and IP-DFG wave generation and characterisation. As can be seen, all the beams involved in the compact scheme are optically-synchronised and generated from the ARR-PCF. Thus, any possible temporal or beam pointing jitters are minimised to enable the most sensitive experiments via EOS. The EOS is a powerful method to characterise the mid-infrared/THz pulses. Still, it is also an excellent tool for transmission/absorption measurements to study different physical processes in gases or solids due to the enormous sensitivity provided by the technique. Thus, this scheme based on the output of the ARR-PCF enables the generation of an ultrafast wave expanding from UV to 40 μm where the UV part can be used for excitation processes and the IP-DFG to probe the process via EOS.

For this purpose, the soliton compressed 3.2 μm pulses are collimated like in the first version using an $f = 100$ mm gold-coated off-axis parabola. A pair of thin

TABLE 3.3: Phase-matching polarisations and angles for IP-DFG in ZGP, BGGSe and GaSe.

	Theta cutting angle	Type 1 polarisations*	Type 1 angle	$D_{eff.}$ Type 1 (pm/V)	Type 2 polarisations*	Type 2 angle	$D_{eff.}$ Type 2 (pm/V)
ZGP	52.9°	$o-e \rightarrow e$	49°	80	$o-e \rightarrow o$	62°	70
BGGSe	25°	$o-e \rightarrow e$	22°	-	$o-e \rightarrow o$	26°	-
GaSe	0°	$e-o \rightarrow o$	11°	55.3	$e-o \rightarrow e$	13°	52.5

* The equation for phase-matching is defined as $pump + signal \rightarrow idler$.

CaF_2 wedges are used to split the compressed 3.2 μm pulses into two separated beams. The output of the ARR-PCF is polarised in S (vertically); thus, the first surface of the first CaF_2 wedge inserted at 45° will reflect around 7% of the high-power mid-infrared beam. This amount is enough to produce an SHG in a 400 μm thin AGS nonlinear crystal to generate broadband 1.6 μm pulses that can be used as sampling pulses for the later EOS scheme. Unfortunately, the dispersion introduced by the thin AGS is enough to stretch the broadband 1.6 μm pulses. Thus a 12 mm thick BK7 AR-coated window is used to compensate the extra dispersion and keep the 1.6 μm pulses compressed to 21 fs for the EOS. The second CaF_2 wedge is used to clean back the tilted wavefronts from the 3.2 μm pulses and maintain a spatial-chirp-free beam for the IP-DFG process. Note that commercially available high-quality beam splitters can be found in the visible and near-infrared regimes. Still, for our near single-cycle 3.2 μm pulses, such optics need to be customised, and in general, they are not as good as in the near-infrared regime. Thus, more primitive optical designs were chosen to ensure that all the generated pulses are propagated without uncontrolled deterioration. Therefore, gold-coated mirrors have replaced HR mirrors with higher losses (5% per optic) but negligible dispersion effects and broader reflection properties.

After the 3.2 μm beam is split, an off-axis parabolic mirror focuses the high-power 3.2 μm beam into a focal spot of 200 μm waist-radius where the ultra-broadband IP-DFG is produced. For the IP-DFG process phase-matching in bulk, the polarisation of the input pulse has to be rotated to $\sim$ 45°. Then type 1 phase-matching or type 2 phase-matching will be only determined by the nonlinear crystal angle. Table 3.3 shows the estimated theta angles for type 1 and type 2 phase-matching of the IP-DFG in GaSe, ZGP and BGGSe. While in general

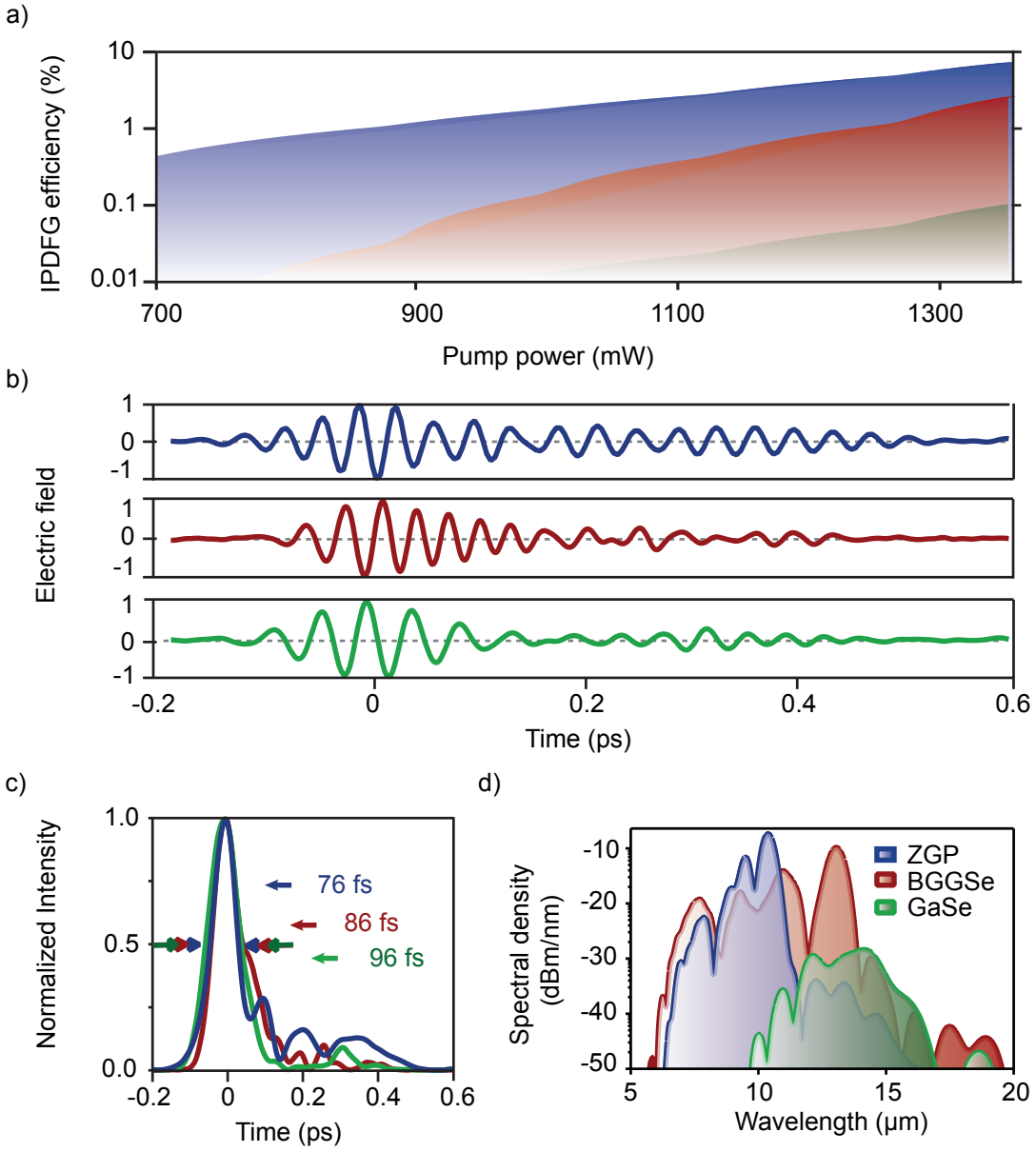

FIGURE 3.17: Power, temporal and spectral IP-DFG comparison at 25 bars of Argon pressure generated in 2-mm AR-coated ZGP (blue), 2.6-mm AR-coated BGGSe (red) and 1-mm uncoated GaSe (green). a) Conversion efficiency in function of the input 3.2 μm power. b) Measured electric-fields via EOS. c) Normalized temporal intensities of the generated IP-DFG. d) Retrieved spectral densities.

type 1 phase-matching provides higher conversion efficiencies than type 2, in the second one, broader phase-matchings are typically achieved. Thus, for our tunable broadband IP-DFG generation type 2 phase-matching is used.

Moreover, the polarisation of the IP-DFG will be determined by the orientation of the nonlinear crystal. Thus, by flipping the nonlinear crystal 90 degrees, the polarisation of the output IP-DFG can be rotated. This condition is necessary

TABLE 3.4: Comparison of the IP-DFG pulse characteristics for ZGP, BGGSe and GaSe at 25 bars Argon pressure.

	Centre wavelength (nm)	FWHM pulse-duration (fs)	FWHM TL-duration (fs)	Pulse optical-cycles (#)	TL optical-cycles (#)
ZGP	10.2	76	53	2.25	1.55
BGGSe	10.0	86	40	2.6	1.2
GaSe	13.0	96	61	2.2	1.45

to exploit in our experiment as GaSe is a negative uniaxial crystal, while ZGP and BGGSe are positive uniaxial crystals. Thus, the output IP-DFG polarisation in GaSe would be perpendicular and would not be phase-matched in the EOS nonlinear crystal.

Figure 3.17 shows the temporal, spectral and power-conversions that have been achieved exploiting the IP-DFG process in 2-mm AR-coated ZGP, 2.6-mm AR-coated BGGSe and 1-mm uncoated GaSe. Using 1.35 W (8.45 μJ) of self-compressed 3.2 μm pulses we demonstrated IP-DFG generation up to 70 mW (0.45 µJ) in ZGP, up to 25 mW (0.16 μJ) using BGGSe and up to 1.8 mW (11.25 nJ) using GaSe. Thus, both ZGP and BGGSe show more than an order of magnitude higher conversion efficiencies than GaSe.

The spectral and temporal information of the IP-DFG pulses is compiled in the electric-field traces shown in Figure 3.17 (b). From those traces, spectral and temporal amplitudes are retrieved. While the spectrum generated from ZGP (Figure 3.17 (d)) is limited to below 12 μm, GaSe enables generating broader pulses centred at longer wavelengths. Moreover, despite the long length of the used BGGSe, it produces the broadest spectrum, spanning over 2 octaves. Thus, we demonstrated that BGGSe combines the properties of GaSe and ZGP, enabling ultra-broadband and high-power IP-DFG generation.

In the time domain (Figure 3.17 (c)) sub-3 cycle waveforms at FWHM intensity were generated by each crystal, close to their TL durations. ZGP produces the shortest pulse as it has narrower spectral content and thus is less sensitive to residual second-order dispersions. GaSe shows the cleanest field shape, centred at a longer wavelength. Therefore the cycle duration is longer, and the dispersion

effect is again lower. In our case, the generated IP-DFG bandwidth in GaSe, ZGP and BGGSe allows compression of pulses down to a single-cycle regime. Still, the dispersion introduced by the nonlinear crystal itself stretches the mid-infrared pulses to 2-2.5 cycles. Table 3.4 summarises the temporal characteristics as well as the centre wavelength of the generated IP-DFG pulses in ZGP, GaSe and BGGSe.

In conclusion, to achieve bright ultra-broadband mid-infrared pulses, BGGSe is demonstrated to be an excellent nonlinear crystal. On the other hand, if high-peak-power pulses around 10 μm are required (for instance, for nonlinear studies), then ZGP provides higher powers with lower pulse durations. Finally, GaSe can be useful when clean electric-field traces are required for high sensitive absorption/transmission experiments.

3.3.3 Multi-octave ultrafast source from ARR-PCF and BGGSe

As shown in Figure 3.13, the spectral and temporal evolution of the compressed 3.2 μm pulses depends on the argon pressure inside the gas-cell. As a result, both the DW generation and the IP-DFG can also be tailored by pressure tuning. Figure 3.18 shows pressure-dependent high-brightness multi-octave spectrum generation that has been achieved using the combination of the optimised mid-infrared ARR-PCF and the new BGGSe mid-infrared high-transmission nonlinear crystal.

In Figure 3.18, in blue, the different spectral densities achieved at the output of the ARR-PCF are shown, while in red is displayed the combined radiation between ARR-PCF and the IP-DFG spectrum in BGGSe. As can be seen in the figure, the transmission window of the BGGSe crystal cuts the radiation below 600 nm, DW included. That is why a silicon wafer is used to split that part of the radiation before the IP-DFG generation.

The maximum DW intensity is achieved at 35 bars, while the longest wavelengths in the IP-DFG process are generated at lower pressures between 20 bars and 25 bars. Moreover, it is shown that the spectral density in the mid-infrared can be tailored while maintaining the high brightness across the spectral range through pressure tuning.

Figure 3.19 shows the envelope peak-power variations of the 3.2 μm solitons (a) and the generated IP-DFG pulses (b) for the different Argon pressures where the high-brightness multi-octave radiation is achieved. While the pedestal in the

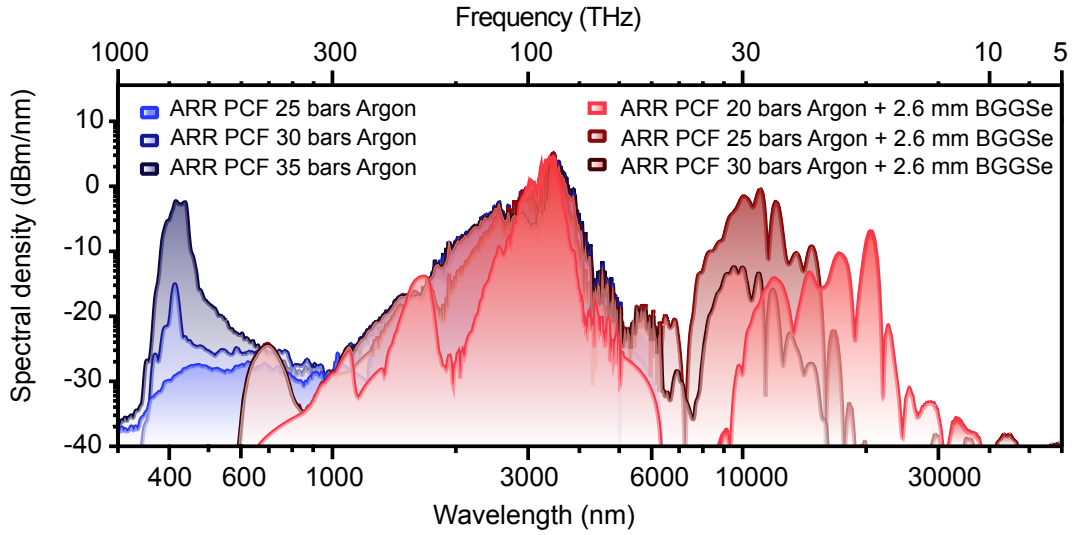

FIGURE 3.18: The measured spectrum of the high-brightness, few-cycle, coherent radiation source for different pressures inside the gas-cell. In different colour-tones of blue is shown the output spectrum from ARR-PCF for 25 bars (light-blue), 30 bars (medium-blue) and 35 bars (dark-blue). In red is shown the combination of ARR-PCF output and IP-DFG spectra in BGGSe at 20 bars (light-red), 25 bars (medium-red) and 30 bars (dark-red).

3.2 μm soliton varies with the pressure introduced in the gas-cell, the main peak of the 3.2 μm pulse remains compressed. The IP-DFG pulses are also compressed to sub-3 optical-cycles across all the pressure range.

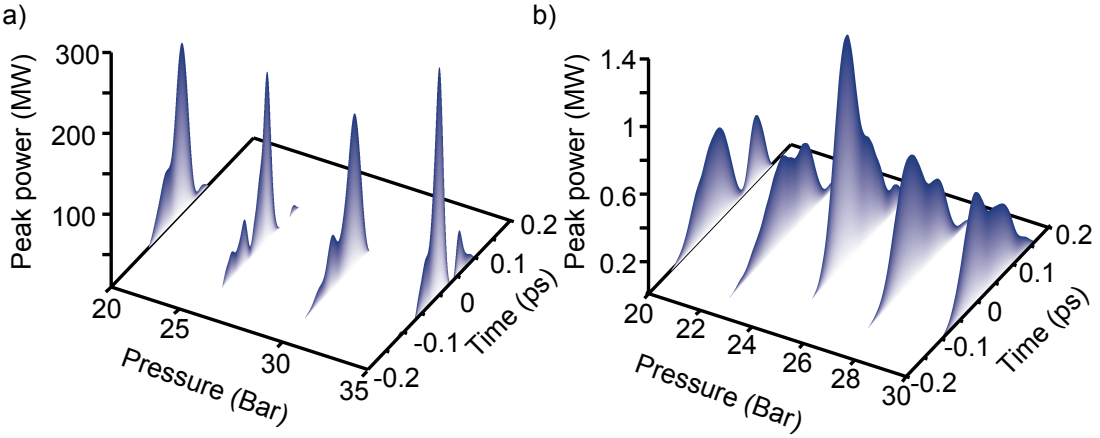

FIGURE 3.19: Evolution of the temporal envelope peak-powers in the function of the Argon pressure inside the gas-cell a) of the 3.2 μm solitons, and b) of the generated mid-infrared IP-DFG in BGGSe.

While the DW duration was not directly measured, we estimated that the DW pulses should also be compressed below 80 fs in all the scanned pressure ranges.

Thus, a simple pressure-tuning enables the generation of optimised spectral content required for the investigation of different molecular processes or light-matter interactions with sub-100 fs duration.

3.4 Conclusions

In summary, we have demonstrated a CEP-stable mid-infrared OPCPA with a chirp-inversion scheme enabling pulse amplification up to 131 μJ energy, at 160 kHz repetition rate and 21 W average power. Pulse compression to 97 fs (sub-9 optical-cycles) with 90% transmission efficiency and excellent pulse-to-pulse stability of 0.33% RMS over 30 mins is shown. Further compression of the mid-infrared pulses in a novel silica capillary-based ARR-PCF down to 1.35 cycles with 80% efficiency is proved via soliton generation. The developed ARR-PCF has been a key tool to boost the peak powers of the mid-infrared OPCPA output to 3.9 GW. This system presents a significant step forward for generating coherent kilo-electron-volt X-rays in table-top systems.

Not only interested in high-photon-energy X-ray generation but also looking forward to enabling multidimensional spectroscopy studies, it has been demonstrated the generation of a high-brightness, tunable, ultra-broadband CEP-stable source with sub-100 fs temporal resolutions. This source has been achieved thanks to an optimised ARR-PCF and the novel mid-infrared BGGSe nonlinear crystal, which together have allowed the soliton self-compression of the 3.2 μm pulses with simultaneous DW generation and the combined bright and broad IP-DFG generation.

In conclusion, while pump lasers nowadays deliver higher energies at shorter pulse duration, the efficient design of the proposed system offers the opportunity to generate kilo-electron-volt X-ray radiation. Moreover, it enables light-matter ultrafast investigations in all the spectral ranges from 340 nm (5.16 eV) and up to 40 μm (31 meV).

Chapter 4

High-energy 7 μm OPCPA

The development of the high-energy mid-infrared OPCPA started around 2012 with the implementation of a three-colour frequency comb source at 100 MHz from Menlo Systems GmbH [39] The three outputs from the fibre laser were conceived to build a full-optically-synchronised system. A pump laser-centred around 2 μm was developed using one of the three outputs from the fibre laser and amplified in a CPA scheme to hundreds of millijoules. The other two outputs from the fibre laser were mixed in a mid-infrared nonlinear crystal via DFG to generate mid-infrared pulses above 6 μm. The mid-infrared pulses were afterwards amplified in an OPCPA design to the millijoule energy levels pumped by the high-energy 2 μm pulses.

The absence of commercially available high-energy lasers above 1 μm highlighted the uniqueness of this 2 μm + 7 μm high-energy laser system, which was designed in collaboration with THALES Group in France. The CPA + OPCPA system was developed to enable tabletop coherent hard-X-rays generation exploiting the wavelength scaling on the strong-field electron recollision process.

In 2015 was demonstrated the generation of 39 mJ of 2052 nm pulses at 100 Hz using the narrowband picosecond output from the fibre laser [143]. In 2016 my colleague and co-worker Daniel Sanchez presented the first design of the OPCPA system delivering 200 μJ and 180 fs pulse durations at 7 μm [144] The OPCPA was comprised of three stages based on ZGP in non-collinear geometry and pumped by 12.2 mJ of 2052 nm energy. While the maximum amplification achieved in the OPCPA was 550 μJ, the final aluminium-grating-based compressor had an overall efficiency of 35% reducing the final available pulse energy significantly.

Just before I started working in the high energy 7 μm OPCPA, Daniel Sanchez began to upgrade the system to overcome the limitations of the OPCPA and increase the 7 μm output energy above the millijoule level. The first goal of the upgrade was to reach pump energies above 200 mJ, which was an intrinsic requirement to later produce pulse energies at 7 μm towards the 10 mJ energy levels (assuming above 5% pump-to-idler conversion efficiencies). Pulse energies in the 2052 nm line up to 260 mJ were achieved in a three-pass cryo-cooled booster CPA using a 50-mm-long Ho: YLF [29]. The cryo-cooled CPA was pumped by a CW 130 W from a Thulium fibre laser at 1940 nm using loose focusing geometry. Unfortunately, cryo-cooling based CPA was driven close to the damage of the Ho: YLF, which was increasing the amplitude fluctuations of the pump pulses up to 0.8%. To achieve higher reliability, I started working on the second upgrade of the 2052 nm pump cryo-cooled CPA. The beam sizes of the 1940 nm and 2052 nm pulses were increased, and an extra-pass was added.

The main limitations on the 7 μm OPCPA were a) the low efficiency of the final compression scheme and b) the maximum pump energies that could be used in a single OPCPA stage. The pump energy in the OCPPA stage was limited by the ZGP aperture and its damage threshold.

Moreover, in the previous design, the 7 μm OPCPA was seeded by a spatial-chirp mid-infrared beam, which was induced by the non-collinear geometry of the DFG. Spatial-chirp, also known as angular-chirp, is introduced when two broadband pulses are combined with a non-collinear geometry in the second-order nonlinear process. In the non-collinear geometry, to match the wave-vectors, α and β angles vary for each frequency inside the generated pulse (see Figure 2.2), thus inducing angular chirp to the generated third-wave. While it is already challenging to correct the spatial chirp in the visible/near-infrared regime [145, 146], in the mid-infrared regime becomes more difficult due to the absence of sensitive beam characterisation devices.

With the previous experience on the 3 μm OPCPA, we decided to implement a collinear geometry-based DFG stage firstly and secondly to replicate the 3 μm OPCPA design with a chirp-inversion stage in the middle. Moreover, both the pulse duration of the 2052 nm pump and 7 μm seed pulses were further stretched to be able to drive the $8x8$ mm^2 ZGP crystals with more pump energy.

In the following sections, I give a more detailed view of each part of the high-energy system and present the measurements and results that I achieved during the development of the different evolving aspects of the system.

Erbium-Thulium-Holmium three-colour fibre laser

The three-colour Erbium-Thulium-Holmium fibre system from Menlo Systems GmbH is based on an Erbium-doped fibre oscillator and a few Erbium doped amplifiers where nanojoule level 1.55 μm pulses are achieved at 100 MHz. Afterwards, the pulses are split inside the system, and one arm is coupled to a solid-core highly nonlinear fibre (HNLF). In the HNLF supercontinuum from 1 μm and up to 2.4 μm is generated via SPM. Later, the 2 μm part of the supercontinuum is amplified in a polarisation-maintaining (PM) Tm/Ho gain fibre via the self-amplification process [147]. The amplified spectrum from the PM Tm/Ho gain fibre expands from 1.9 μm to 2.16 μm. This beam is again split. One arm is amplified in a second PM Tm/Ho gain fibre and externally compressed down to 135 fs in a Martinez type gold-coated compressor. The second arm is filtered to narrow the bandwidth of the 2 μm pulses. With $\sim$ 2 ps duration, the 2052 nm narrowband pulses are efficiently amplified in a high-power PM Tm/Ho gain fibre up to 0.5 W.

The Erbium-Thulium-Holmium fibre system delivers 300 mW (3 nJ) at 1550 nm with 70 fs durations, 100 mW (1 nJ) 2025 nm with 135 fs pulse duration, and the narrowband 2052 nm with $\sim$ 2 ps and 0.5 W.

As the 2-μm broadband pulses are generated via SPM of the 1550 nm pulses, the phase of both colours is related and can be described using the equation 2.2.4. Therefore, the CEP of the mid-infrared 7 μm pulses generated via DFG between those two pulses is expected to be stable. The CEP stability of the 7 μm 100 MHz pulses is proved by measuring the electric field via EOS.

4.1 Development of the high-energy 2 μm Ho:YLF picosecond pump laser

Figure 4.1 shows the design of the CPA where the 2052 nm nanojoule level pulses are amplified up to 260 mJ. The peak intensity through the CPA is maintained below 5 GW/cm^2 to avoid damages in optics. For this purpose, the 2 ps pulses from the Erbium-Thulium-Holmium fibre are stretched up to 340 ps using an AR-coated chirp-volume Bragg grating (CVBG) from (OptiGrate Corp.). The CVBG introduces a dispersion of 150 ps/nm around 2052 nm and has an aperture of 5x8 mm^2. The bandwidth of our picosecond 2 μm pulses is around 2 nm, which

implies that four passes would be required through the CVBG to stretch the pulses to ∼ 300 ps. While in the first 40 mJ CPA design [143] the pulses were stretched up to 170 ps in a double-pass scheme, in the newer version to achieve higher energies, the pulses were stretched to 340 ps.

For the four-pass CVBG configuration, the narrowband 2052 nm vertically polarised beam is sent through an optical isolator. Afterwards, the transmitted beam is reflected in a thin-film polariser (TFP) at 45° and again reflected in the CVBG at a slight angle towards a quarter-wave plate (QWP). Afterwards, The beam is back-reflected towards the CVBG using a mirror at normal incidence. Note that if the CVBG is used at an angle different from normal incidence, like in this case, the reflected beam is spatially chirped and a second pass is required to clean back the wavefronts [148]. The QWP is chosen to rotate the polarisation of the 2052 nm beam from vertical to horizontal after two passes through it. After the second reflection in the CVBG goes through the TFP, and using a second mirror at normal incidence, the beam is sent back towards the CVBG for another two passes. Finally, after four reflections in the CVBG, the again vertically polarised beam is reflected in the TFP, and it goes towards the optical isolator, which reflects the beam at 45° towards the CPA scheme.

A Rubidium Titanyl Phosphate (RTP) Pockels cell (PC) from Bergmann Messgeraete Entwicklung KG is used as a pulse picker at the output of the stretcher to reduce the repetition rate from 100 MHz to 100 Hz before introducing the pulses into the regenerative CPA. The PC uses the basics of the linear electro-optic effect described in section *"Linear electro-optic effect"*. By applying a periodic voltage to the RTP, the polarisation of the 2052 nm pulses can be tunned periodically. The voltage is chosen to flip the polarisation from vertical to horizontal once every 10^6 pulses. Thus, the pulses that remain vertically polarised after the PC are rejected from the beam path using a TFP, and only the 100 Hz pulses are transmitted through the TFP.

The Ho: YLF crystal shows an upper-level lifetime of around 14 ms, which limits the repetition rates that can be used in the regenerative CPAs. While in the literature, higher repetition rates have been demonstrated, chaotic amplifications with pulse bifurcations can be produced when higher repetition rates than 100 Hz are used [149–151]. In this chaotic regime, deteriorated beams with high pulse-to-pulse fluctuations can be generated, affecting the overall system's performance. The chaotic performance of the regenerative CPA can be overcome by pumping the active material over the chaotic regime [28].

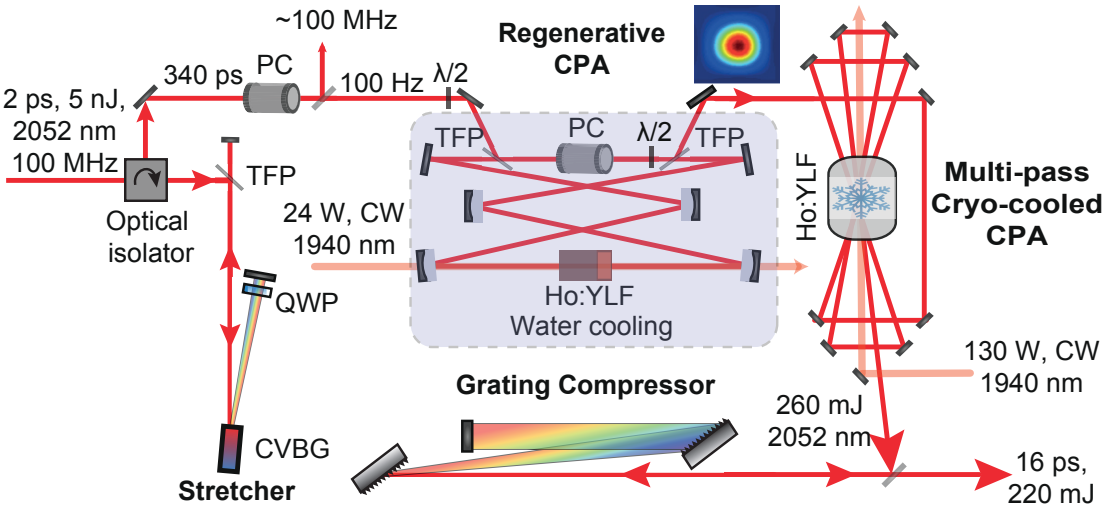

FIGURE 4.1: Schematic design of the high-energy CPA driven by the 2052 nm picosecond pulses. The nanojoule level 2052 nm pulses are stretched to 340 ps in a CVBG to introduce them in the regenerative CPA afterwards. Millijoule level 2052 nm pulses out from the regenerative CPA are presented in the cryo-cooled multi-pass booster CPA to increase the 2052 nm energy up to 260 mJ. The high-energy 2052 nm pulses are back-compressed down to 16 ps in an HR-coated dielectric reflection grating compressor.

The regenerative CPA is based on a water-cooled 3.5-cm-long, 0.5% doped Ho: YLF driven by a 30 W CW Thulium fibre (Tm: fibre) laser centred at 1940 nm from IPG Photonics. A second PC sandwiched between two TFP is used to control the number of passes in the regenerative CPA. A half-waveplate inserted after the PC rotates the polarisation of the 2052 nm pulses from vertical to horizontal. Thus, if no voltage is applied to the PC, the 2052 nm pulses make a single-pass through the CPA and go out reflected in the output TFP. The regenerative CPA used for the amplification of the 2052 nm pulses was designed and built by Dr. Michael Hemmer [143]. The Ho: YLF is pumped by 9.6 W from the Tm: fibre laser at π-polarization [152]. After 36 passes through the regenerative CPA up to 4 mJ of 2052 nm pulses are achieved (gain of $\sim 10^3$) [143].

The advantage of using a CPA design is that the amplification depends only on the fluence of the involving pulses and not on the peak intensity. Thus, CW pump lasers can be used to amplify the picosecond pulses. Moreover, the seed pulse duration does not affect the amplification efficiencies, which can be varied to avoid damages in optics. Therefore, for the new version where the 2052 nm pulses were stretched from 170 ps to 340 ps, the regenerative CPA stayed un-affected.

The Ho: YLF is a birefringent crystal. Thus, absorption and emission coefficients

depend on the input beam polarisation. Moreover, the Ho: YLF energy levels divide from a quasi-three-level system to a four-level system at liquid-nitrogen temperatures (80 K) [153]. Thus, while in-room temperatures, the -direction shows high absorption and emission coefficients for both 1940 nm and 2052 nm [152, 153], at cryo-cooled temperatures, the absorption around 2052 nm decreases significantly [143]. Therefore, to boost the energy of the 2052 nm pulses in a compact scheme and with the highest efficiencies, the booster CPA is based in cryo-cooled 25-mm-long 0.5% doped Ho: YLF crystal. The following sections show the results I achieved in the newly designed four-pass booster CPA.

Moreover, notice that all the 2 μm system is purged with dry air at zero humidity which makes the alignment more challenging. The reason is that water absorption lines are present around 2 μm. In the case of the CW 1940 nm beam, the absorption lines cannot stretch the pulses but introduce huge fluctuations on the beam pointing as well as deteriorate the beam profile of the pump. Thus, it is crucial to align the system at $< 1\%$ humidity.

4.1.1 Multi-pass CPA

The bow-tie type four-pass cryo-cooled CPA is pumped in single-pass using a randomly polarised 130 W CW Thulium fibre laser from IPG Photonics. A cryo-refrigerator from CryoSpectra with a cooling capacity of 100 W at 90 K is used to cool the 25-cm-long Ho: YLF crystal. While the pump power is 130 W, the actual power that is absorbed by the Ho: YLF crystal is around 82% (107 W) and pump to seed conversion efficiency $\sim$ 20%, thus below 90 W are required to be cooled by the cryo-refrigerator. Moreover, both the seed (2052 nm) and the pump (1940 nm) beams were collimated to 2.1 mm of waist radius to maintain the peak intensity in the booster below 10 GW/cm^2 (above 200 mJ). The reduced peak intensity in the cryo-cooled crystal improves the performance of the system and lowers the pulse-to-pulse fluctuations of the high-energy 2052 nm pulses.

In Figure 4.2 are shown the measured and simulated results from the four-pass high-energy CPA. Unfortunately, the 130 W IPG got damaged before the fourth-pass was aligned, and therefore, in this thesis, only the experimental results in a four-pass scheme pumped by a 100 W IPG system are shown. The four-pass CPA was pumped with 100 W from the Tm: fibre from which 82 W were absorbed in the Ho: YLF crystal. In the multipass collimated-beam geometry, energies up to 77.4 mJ were achieved, concluding on 9.4% power conversion efficiency. As can be

seen in Figure 4.2 (a) and (b), the power dependence of the amplification process in the CPA is exponential. Thus, as shown in the simulations, it is expected to reach energies above 200 mJ when pumping the booster CPA with 130 W. Moreover, thanks to the new design with reduced peak intensity, pulse-to-pulse fluctuations decreased to 0.26%, compared to the previous 0.8%. Thus, this design produces robust 2052 nm high-energy pulses with excellent features for pumping the 7 μm OPCPA system. Note that pulse-to-pulse fluctuations of 0.26% are close to the pump features in the 3 μm OPCPA with 0.3% fluctuations.

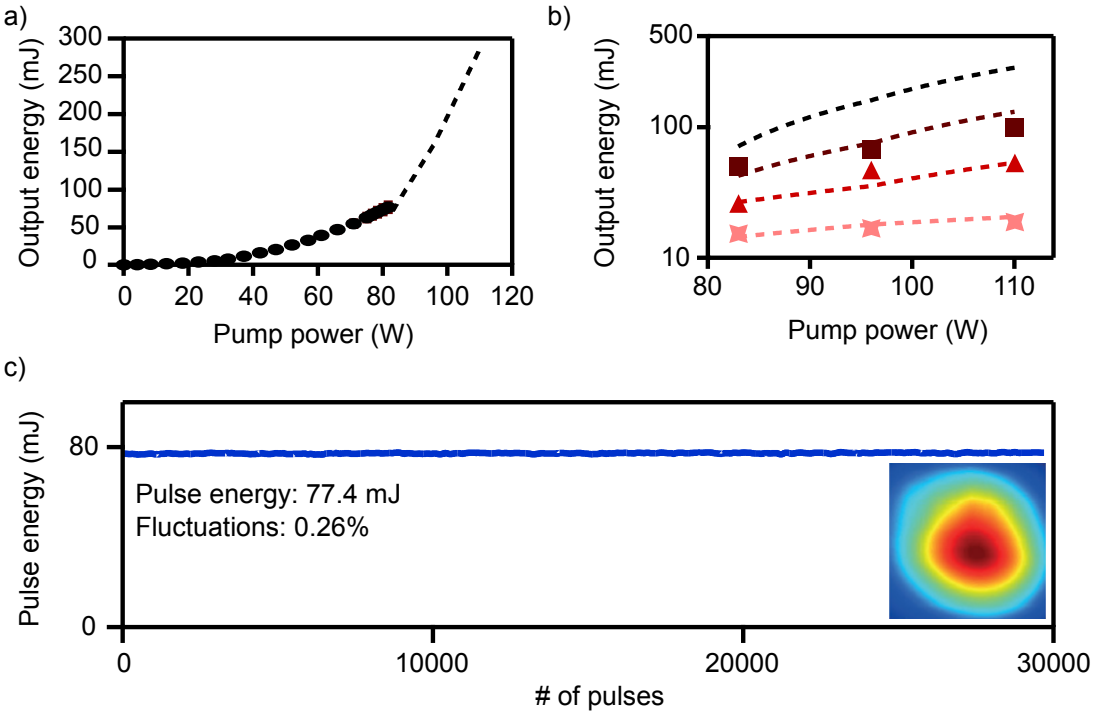

FIGURE 4.2: Characterisation of the four-pass CPA booster. a) Measured (black dots) and simulated (black lines) output energy of the fourth pass in the function of the input 1940 nm pump power. b) Measured first (light-red stars), second (red triangle) and third (dark-red square) pass in the cryo-cooled booster CPA. With light-red dashed lines, normal-red dashed lines, dark-red dashed lines, and black dashed lines are shown the simulated results for the first, second, third and fourth passes, respectively. c) Shows the pulse to pulses fluctuations measured over 30 thousand pulses. The inset shows the beam profile measured at the output of the CPA.

The beam profile of the 2052 nm amplified pulses is shown in the inset of Figure 4.2 (c). The 2052 nm beam, as well as the 7 μm beam in the OPCPA, is measured using a Vanadium oxide-based microbolometer from DataRay Inc. with a pixel size of 17 μm. While this camera is essential for beam profile checkings, the low dynamic range provided and the big pixel size of the camera makes it unsuitable for focal spot determinations. Instead, a home-built knife-edge method was used

to ensure the beam sizes of the 2 μm and 7 μm beams in critical planes such us Ho: YLF crystal position or ZGP position planes. Moreover, while in the 160 kHz OPCPA commercially available fast knife-edge devices could be used to retrieve the beam sizes (Pyroelectric Scanning Slit Profiler NanoScan from Ophir Optronics), those devices are un-suited for lower repetition rates like 100 Hz.

4.1.2 Compression in high-reflection gratings

In the first version of the 2052 nm CPA, a big aperture CVBG was used to compress the high energy output from the CPA. Unfortunately, the maximum energy that could be compressed was limited by the aperture of the CVBG and the third-order processes generated at such high energies. Thus, for the booster upgrade, the compression of the high energy 2052 nm pulses is carried out using a pair of HR-coated reflection gratings from Fraunhofer IOF.

The HR-coated gratings have a grating period of 900 lines/mm. The Littrow angle of the grating used can be calculated from $\theta_L = \arcsin\left(\frac{\lambda}{2d}\right)$ where d is the grating period inversely proportional to the grating line density. Therefore, the maximum grating line density allowed is limited to the Littrow angle, which is required to be below 90°. At the Littrow configuration, the diffracted beam is reflected in the direction of the incident beam. At larger incident angles, the beam is diffracted at shorter angles and vice-versa. Thus, the maximum line density that can be used at a given frequency is limited by the beam size and the aperture of the effective area of the grating that decreases at larger incident/diffracted angles. For the back compression of the high-energy 2052 nm pulses, at a Littrow angle of 67.4°, the incident angle is kept around 65° to be diffracted at 70°.

For the compression of the 340 ps 2052 nm pulses, a grating distance close to 2.5 m is used with a folded footprint of 140 cm by 25 cm. The estimated laser-induced damage threshold (LIDT) is $> 300\ mJ/cm2$, thus to avoid damages in the grating surface, a beam size close to 10 mm waist radius is used in the HR-coated grating with 65 mm x 100 mm aperture size.

The characterisation of the 2052 nm high-energy pulses is carried out using an SHG intensity autocorrelation (AC) technique (see appendix A for details). The SHG-AC can be described by the convolution of the pulse with itself:

$$A(\tau) = \int_{-\infty}^{\infty} I(t)\, I(t-\tau)\, \mathrm{d}t \tag{4.1.1}$$

TABLE 4.1: The relation between SHG-AC with a FWHM value of Δt_{AC} and the original pulse with FWHM of Δt_p.

	$I(t)$	$A(\tau)$	$\Delta t_{AC}/\Delta t_p$
Gaussian	$I_0 e^{-\left(\frac{2\sqrt{Ln2}}{\Delta t_p}t\right)^2}$	$A_0 e^{-\left(\frac{2\sqrt{Ln2}}{\sqrt{2}\Delta t_p}t\right)^2}$	$\sqrt{2} \approx 1.41$
Lorentzian	$I_0 \frac{1}{1+(2t/\Delta t_p)^2}$	$A_0 \frac{1}{1+(2t/2\Delta t_p)^2}$	2.0
$Sech^2$	$I_0 Sech^2\left(\frac{1.76t}{\Delta t_p}\right)$	$A_0 \frac{\left[\frac{2.72t}{1.54\Delta t_p} Coth\left(\frac{2.72t}{1.54\Delta t_p}\right)-1\right]}{Sech^2\left(\frac{2.72t}{1.54\Delta t_p}\right)}$	1.54

where $I(t)$ is the pulse intensity and $A(\tau)$ is the measured SHG-AC. Thus, the FWHM duration of the characterised pulses can be estimated by approximating the shape of the measured AC to a known trace like Gaussian, Lorentzian or $Sech^2$. In Table 4.1, are shown the conversion factors for those pulse shapes.

In figure 4.3 is shown the characterisation of the high-energy 2052 nm pulses. The pulse shape is sensitive to the dispersion introduced by the water absorption lines present in the air. In red is shown the intensity AC measured at 20% of ambient humidity, and it is well fitted to a Lorentzian shape (in dashed red lines). In blue is shown the same autocorrelation after the pump line is purged with dry air ($< 1\%$ humidity), and with blue dashed lines, it is shown the fitting with a Gaussian shape. The FWHM duration of the AC when the line is purged is around 23 ps, while at 20% humidity, the AC value is approximately 33 ps. While the conversion factor for an AC of Gaussian shape is 1.41, the conversion factor between a Lorentzian pulse and its AC is 2.0. Thus, the FWHM duration calculated from both ACs is approximated to 16 ps.

In conclusion, the FWHM durations are similar, but the power content above 50% of the maximum intensity is much lower when the humidity is higher. The amplification in the CPA is independent of the temporal distribution of the 2052 nm pulses; in contrast, the OPCPA amplification dependence on the peak intensity, which reduces the OPCPA efficiency at higher ambient humidities. Therefore, keeping the pump line close to zero humidity is crucial to achieving higher amplification efficiencies.

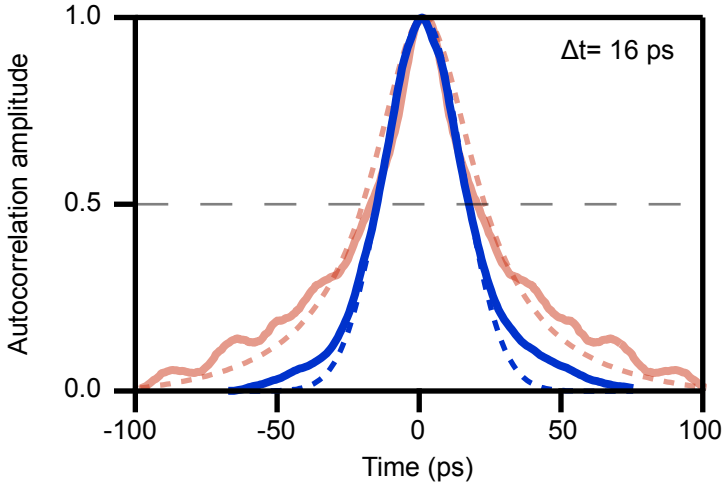

FIGURE 4.3: Autocorrelation of the compressed 2052 nm pulses in the HR-coated dielectric gratings. In blue is shown the shape measured when the full 2052 nm line was purged to $< 1\%$ humidity and its Gaussian fitting with dashed blue lines. In red is shown the SHG autocorrelation measured at 20% humidity in the 2052 nm line and its Lorentzian fitting in dashed red lines.

4.2 Bright 7 μm generation at 100 MHz

In the first OPCPA version, the DFG was carried out using a CSP mid-infrared nonlinear crystal at non-collinear geometries [38]. Pulse energies up to 150 pJ (15 mW) were generated, but due to the non-collinear geometry used for broad-band phase-matching, the generated mid-infrared pulses were spatially chirped. The spatial chirp on the seed mid-infrared pulses increased the challenge to propagate and characterise the mid-infrared pulses limiting the OPCPA design to three stages. Thus, to remove the spatial chirp, the non-collinear CSP-based DFG stage was swapped by a collinear GaSe-based stage.

Figure 4.4 shows the generated mid-infrared spectrum from the GaSe nonlinear crystal (in red) and the newly developed BGGSe crystal. Moreover, with dashed lines are illustrated the simulations of the spectral density from type 1 collinear DFG in 1 mm GaSe (red), 1.5 mm CSP (black) and 2.6 mm BGGSe (blue). The estimated figure-of-merit values for type 1 collinear phase-matching in CSP, GaSe and BGGSe are $\sim 70\ pm^2/V^2$, $\sim 120\ pm^2/V^2$ and $\sim 140\ pm^2/V^2$ respectively. Notice that CSP has the highest figures of merit values ($> 200\ pm^2/V^2$) in type 2 but not in type 1, where our collinear DFG can be phase-matched. Unfortunately, the high Fresnel reflection loss in the uncoated GaSe gives worse spectral brightness results than in CSP.

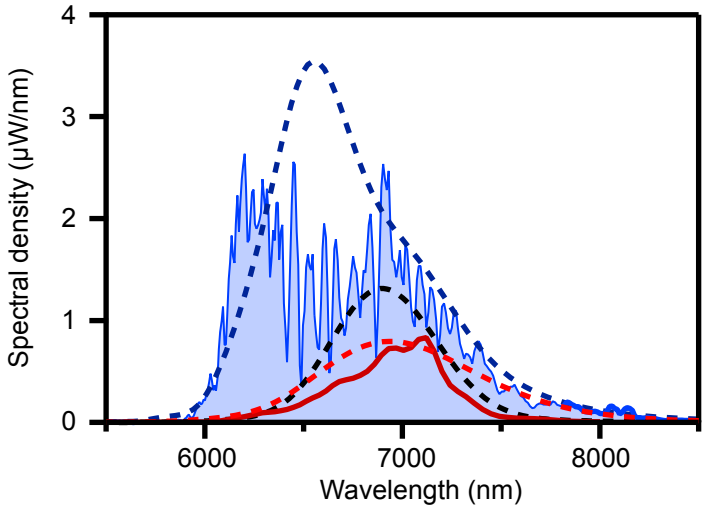

FIGURE 4.4: Measured (solid lines) and simulated (dashed lines) spectral density from the collinear-DFG process in 1 mm uncoated GaSe (red), 1.5-mm-long AR-coated CSP (black) and 2.6-mm-long AR-coated BGGSe (blue).

Taking advantage of that, unlike GaSe, BGGSe can be AR coated; we recycled the 1.55 μm pulses to generate short sampling pulses for the EOS measurements [75]. The 7 μm pulses were separated from the pump (1.55 μm) and signal (2 μm) pulses using a dichroic mid-infrared separator from Edmund Optics. We managed to save 100 mW (1 nJ) from the input 300 mW of the 1.55 μm pulses. Afterwards, the 1.55 μm pulses were coupled into a 20-cm-long solid-core all-normal-dispersion PCF (ANDi-PCF). The broadening in an ANDi-PCF enables pure SPM based spectral expansion, which can be post-compressed using a Fused silica pair of wedges. Pulse compressions from 59 fs to 21 fs were achieved using the recycled 1.55 μm pulses (see appendix A for more details). While compression of the 1.55 μm pulses via soliton generation could be more efficient, pure broadening via SPM was chosen to minimise temporal jitters between the sampling pulses (1.55 μm) and the 7 μm pulses.

From the EOS measurement, we managed to characterise the mid-infrared pulses generated from the DFG stage with such a high sensitivity that we could retrieve the phase jumps induced by the water absorption lines. In Figure 4.5 is shown the characterisation of the 7 μm pulses at 100 MHz and after 2.5 m of propagation in free space at 40% humidity. As can be seen in the absorption lines visible in the spectrum and phase, a substantial amount of water absorption peaks exist below 7 μm. Above 7 μm, the absorption lines disappear, and a cleaner spectrum is achieved. The absorption lines and their effects in the phase of the mid-infrared

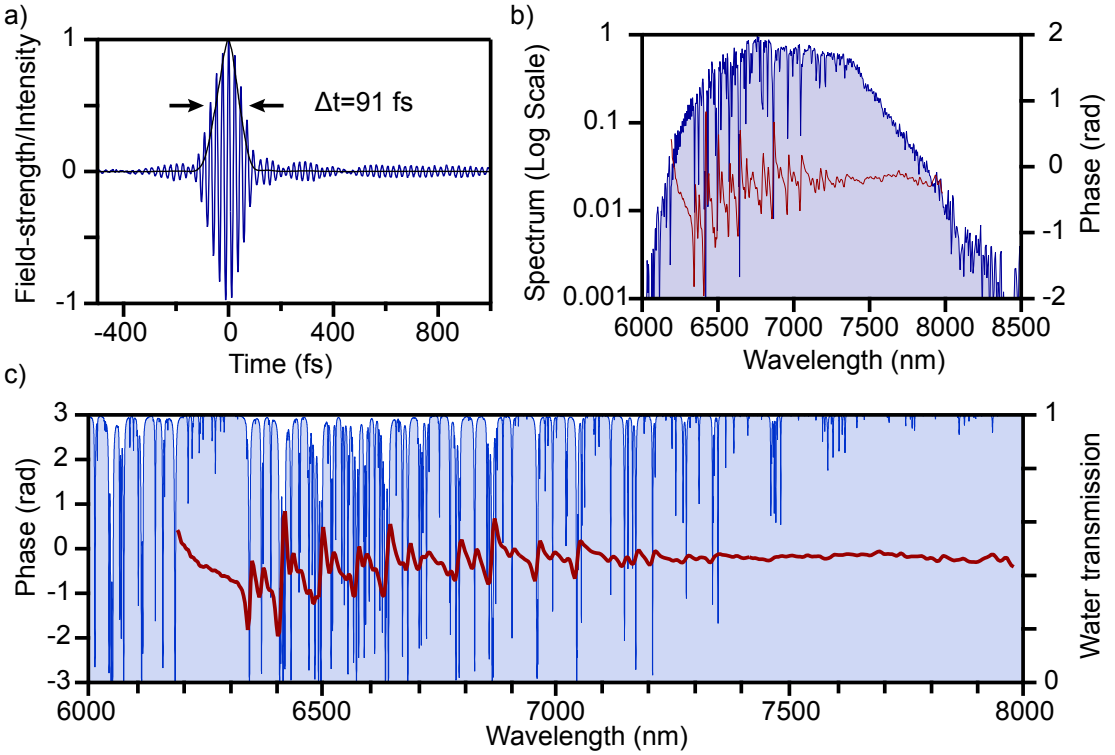

FIGURE 4.5: Characterization of the 7 μm sub-10 pJ 100 MHz pulses. a) Electric field (blue) and intensity (black) of the 7 μm pulses retrieved from the EOS measurement. b) Normalized spectral density of the mid-infrared pulses in shadowed blue and the spectral phase in red. c) Spectral phase (red) and water transmission from the Hitran database (shadowed blue).

pulses shown in Figure 4.5 highlight the importance of developing an OPCPA above 6.7 μm to avoid the main absorption lines between 6.4 μm and 6.7 μm.

The BGGSe sample was acquired after I built the 7 μm OPCPA with the chirp-inverter stage in the middle. Thus GaSe was used in collinear geometry for the generation of the free-angular-chirp 7 μm seed pulses.

4.3 7 μm OPCPA at 100 Hz

Figure 4.6 shows the schematic design of the 7 μm OPCPA. The two femtosecond outputs from the Erbium-Thulium-Holmium fibre front-end are combined in type 1 phase-matching for the DFG process in the GaSe crystal described above. The 7 μm pulses are stretched to 4 ps in a three-pass scheme through a 6-mm-long uncoated BaF2 rod.

All the OPCPA stages are based on ZGP nonlinear crystals from BAE Systems. Type 1 phase-matching configuration in non-collinear geometry with an internal angle between the pump and seed beams of 2.1° ($\theta_{ext.} = 6.6°$) were used in all the stages. The pump peak intensity in the OPCPA stages was set to be between 2 and 4 $GW cm^2$ to avoid damages on the ZGP crystals. Thus, while the pump pulse duration was increased to 16 ps, the overall pump energy used in the OPCPA was still limited to 21.7 mJ due to the reduced ZGP aperture size of 88 mm^2.

Similar to the 3 μm system, the 7 μm OPCPA consists of a pre-amplification and a booster amplification section, with an intermediate chirp inversion stage. Moreover, the final compression is carried out similarly in an efficient three-pass scheme through a 16-cm-long uncoated BaF2 rod.

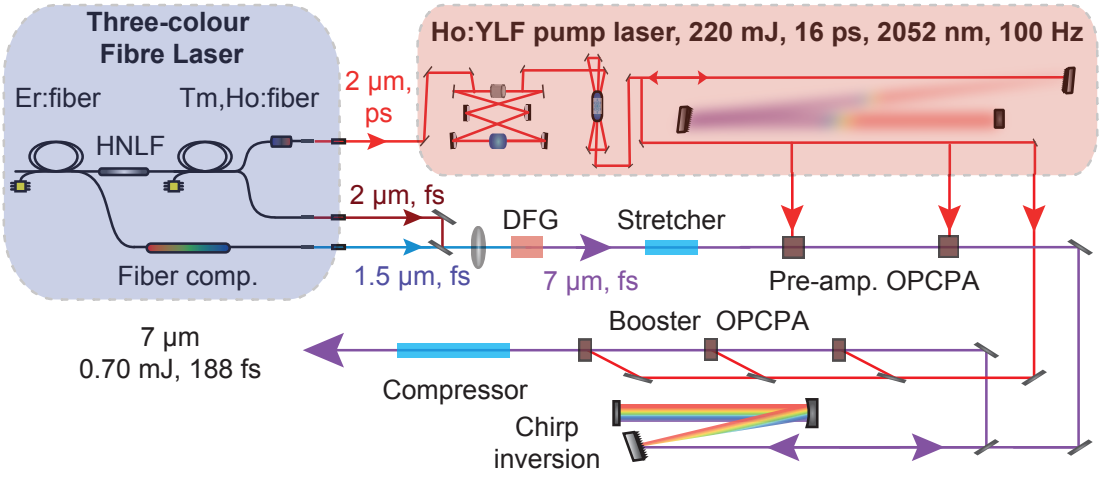

FIGURE 4.6: High energy 7 μm OPCPA scheme. A three-colour fibre front-end drives all system. The mid-infrared pulses generated via DFG are stretched in BaF2 uncoated rod and consecutively amplified in a preamplifier and booster amplifiers with an intermediate chirp-inversion stage. Finally, the 7 μm pulses are compressed in a second uncoated BaF2 rod.

While the initial idea was to build four OPA stages before the chirp-inverter and another four in the booster amplifier, the lack of suitable ZGP crystals reduced the design of the OPCPA to a maximum of five stages. Table 4.2 shows the characteristics of the OPCPA stages and the nonlinear crystals used in each stage. Notice that the first three ZGP crystals are uncoated. The losses induced by Fresnel reflection in ZGP are significant as 27.5% of the pump is reflected on the first surface of the crystal. Therefore, the actual energy used for the amplification is $\sim$ 25% lower. The reflection losses cannot be compensated using higher pump energies, as the damages on the ZGP surface are limiting. Moreover, another 26.7% of the 7 μm energy is lost reflected in the output surface of the ZGP. Nevertheless,

TABLE 4.2: Characteristics of the nonlinear crystals used in the 7 μm OPCPA stages.

	Crystal	Coating	Length (mm)	Cutting angle	Aperture (mm^2)	Output energy	gain	Efficiency (%)
DFG	GaSe	uncoated	1	0°	ø7	7 pJ		
OPA 1	ZGP	uncoated	3	56.8°	6x8	100 nJ	$> 10^4$	0.05
OPA 2	ZGP	uncoated	3	52.9°	8x8	20 μJ	200	1.3/1.18*
Chirp-inverter						2 μJ		
OPA 3	ZGP	uncoated	5	56.8°	5x5	50 μJ	25	3.3/1.6*
OPA 4	ZGP	AR: (2052 + 2900 +7000) nm	2	56.8°	6x8	250 μJ	5	5.7/3.7*
OPA 5	ZGP	AR: (2052 + 2900 +7000) nm	2	52.9°	8x8	750 μJ	3	3.3/3.5*

* The accumulative efficiency is calculated from the overall amplification and all the pump power used.

the amplification efficiencies achieved in the uncoated ZGP crystals are comparable or even better than the efficiencies achieved in the 3 μm OPCPA based on the PPLN crystals.

Another distinctive signature of these OPCPA is the use of ZGP crystals cut at different angles. From one side, we have used ZGP crystals cut close to the OPA phase-matching angle for non-collinear geometry (at 56.8°). In contrast, few are cut at the phase-matching angle for collinear OPA phase-matching (at 52.9°). However, due to the absence of commercially available required dichroic combiners and separators at 7 μm, all the OPCPA stages are aligned for non-collinear geometries. Consequently, a slight front tilt in the 7 μm pulses is induced where ZGP crystals cut at 52.9° are used, which explains the low conversion efficiency achieved in OPCPA 5.

Even with all these challenges and limitations, amplification powers up to 750 μJ are achieved in this mid-infrared high-energy system [29]. While for higher amplification efficiencies, higher aperture AR-coated ZGP crystals would be required,

we demonstrated that a similar design as in the 3 μm OPCPA could be helpful to bust the overall efficiency of the high-energy OPCPA. In the following sections is described in detail each section of the high-energy mid-infrared OPCPA.

4.3.1 Pre-amplifier OPCPA

The pre-amplification section is based on two OPCPA stages based on 3-mm-thick uncoated ZGP crystals pumped by 200 μJ and 1.5 mJ 2052 nm pulses and achieving 7 μm amplification to 0.1 and 20 μJ energies, respectively. Figure 4.7 shows the comparison between the generated spectrum from the DFG process and the amplified spectrum after the pre-amplification section.

The spectrum of the DFG output at 100 MHz is measured using a highly sensitive Fourier-transform infrared (FTIR) spectrometer. Unfortunately, at 100 Hz, the typical FTIR spectrometers cannot be used. Thus, a standard monochromator from Newport together with a nitrogen-cooled mercury cadmium telluride (MCT) detector is used to measure the spectrum of the 7 μm 100 Hz pulses. After the first OPCPA stage, the signal of the 7 μm 100 Hz pulse is too weak for the spectral characterisation using the monochromator + MCT scheme. Thus, spectral characterisation is only carried out after the second OPCPA stage.

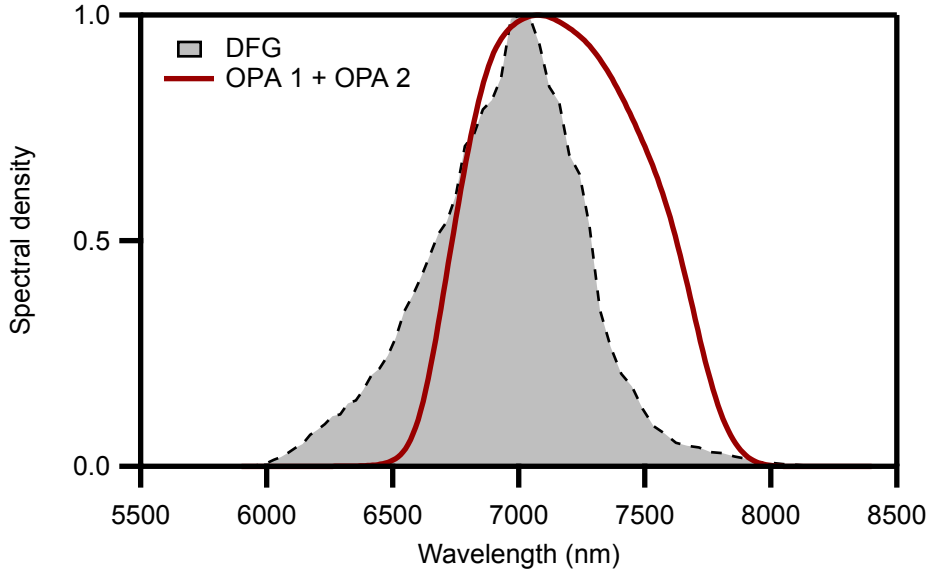

FIGURE 4.7: Spectral density of the generated 7 μm pulses via DFG at 100 MHz (shadowed grey) and measured amplified spectrum after OPA 2 (solid red) at 100 Hz.

4.3.2 Chirp-inverter

One of the challenges of building an OPCPA with such low seed energies is the difficulty characterising the seed pulses' stretched duration. In a system based on a high-energy femtosecond front-end, cross-correlation can be used driven by the femtosecond intense pump pulses. In our case, the only strong enough pulse is the 2052 nm 16 ps duration pump, which is too long to characterise pulses with few picosecond durations. Thus, we rely on simulations for the estimation of the stretched 7 μm duration, which can vary significantly depending on the spectral bandwidth of the mid-infrared pulses.

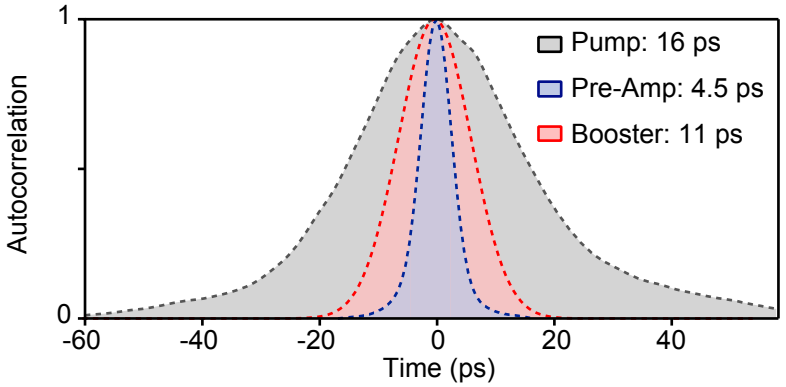

FIGURE 4.8: Comparison of the SHG-AC of the 7 μm pulses in the pre-amplification OPCPA (shadowed blue), booster OPCPA (shadowed red), and the compressed 2052 nm pump pulses (shadowed grey). The respective FWHM durations are shown in the inset.

The mid-infrared energies achieved after the pre-amplification section enable the characterisation of the stretched mid-infrared pulses via SHG-AC. In Figure 4.8 is shown SHG-AC traces of the stretched 7 μm pulses in the pre-amplification section and after the chirp-inverter. The stretching factor of the mid-infrared pulses in the pre-amplifier is around 0.28. Initial calculations estimated stretched mid-infrared duration of approximately 6 ps, which would imply a stretching factor of about 0.37% similar to the one achieved in the pre-amplification section of the 3.2 μm OPCPA. Unfortunately, the spectral narrowing produced in OPA 1 and OPA 2 reduced the effect of the dispersion introduced in the bulk stretcher.

The chirp-inverter is based on an Aluminum-coated reflection grating with 150 lines/mm and a gold-coated 2-inch size curved mirror with $f = 200$ mm. The distance between the grating and the curve mirror was set to around 190 mm to compensate for the initial negative chirp and add extra positive chirp. The overall efficiency of the chirp-inverter was concluded to be only 10%.

Using the advantages of having a chirp-inverter in the middle of the OPCPA, we stretched the mid-infrared pulses up to 11 ps to optimise the amplification in the booster amplifier.

Due to the low sensitivity of the monochromator + MCT, we ruled out following a similar procedure like in the 3 μm OPCPA to choose the stretching factor by continuously tunning the chirp-inverter and estimating the peak power that the OPCPA could deliver. For instance, while using the FTIR dynamic ranges above four orders are suitable to achieve (see Figure 3.15 or Figure 3.18), using the combination of monochromator + MCT, we were limited to dynamic ranges below 3 dB. The chirp-inverter was set from the beginning to introduce a dispersion that could be compensated at the end of the OPCPA using a 48-cm-long BaF2 rod.

4.3.3 Booster-amplifier OPCPA

The booster amplifier is based on three consecutive OPCPA stages. The first stage is based on a 5-mm-thick uncoated ZGP crystal, which is mainly used to compensate for the losses induced by the chirp-inverter. The last two stages are composed of 2-mm-thick AR-coated ZGP crystals. The 2052 nm pulses drive these final two stages with 3.5 and 15 mJ energies, boosting the 7 μm pulse amplification to 0.25 and 0.75 mJ, respectively.

For the temporal overlap between the 7 μm pulses at the output of the chirp-inverter and the pump pulses, a significant extra beam path ($\sim$ 3 m) of the pump 2052 nm beam is required. HR curved mirrors are used to keep the beam size of the 2052 nm pulses collimated. We found that in the high energy beam path, dust particles were attracted towards the beam, producing damage on various HR mirrors. This problem was solved by implementing a dust-free dry air compartment, which was also required to avoid the creation of the pedestal induced by water absorption lines.

Figure 4.9 shows the evolution of the amplified 7 μm spectrum after the mid-infrared pulses are further stretched up to 11 ps. While in the pre-amplification section, the efficiency is limited to 2%, above 5% efficiencies are achieved in the booster. Moreover, the strong chirp introduced in the chirp-inverter produces a spectral narrowing effect in the OPCPA stages, increasing the TL durations from 126 fs (OPA 2) to 155 fs (OPA 5).

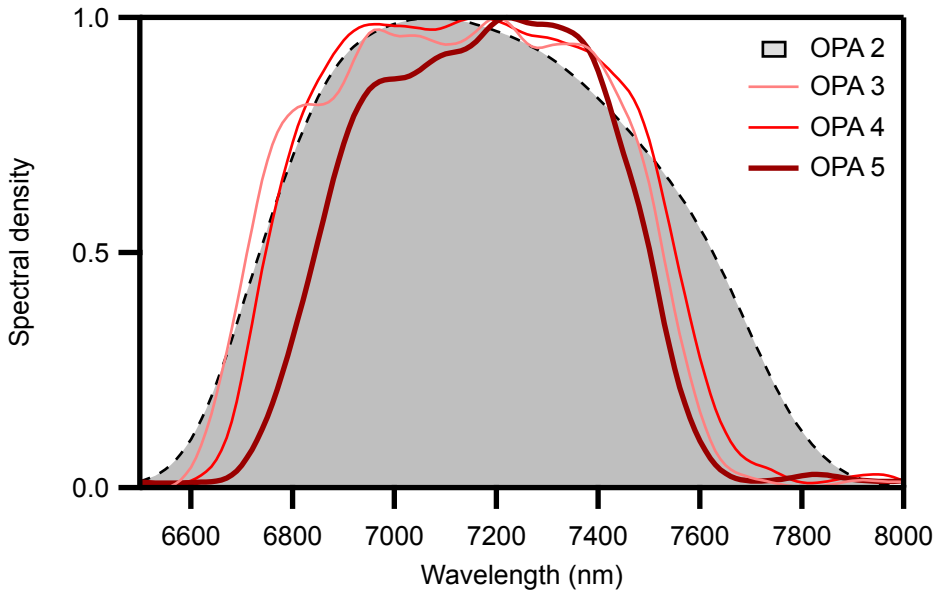

FIGURE 4.9: The spectrum measured of the mid-infrared pulses out of the chirp-inverter in shadowed grey together with the amplified spectra from each booster OPCPA stages.

Figure 4.10 shows the characteristics of the five 7 μm OPCPA stage. The saturation of the stage ensures that the pulse-to-pulse fluctuations of the mid-infrared output are minimised.

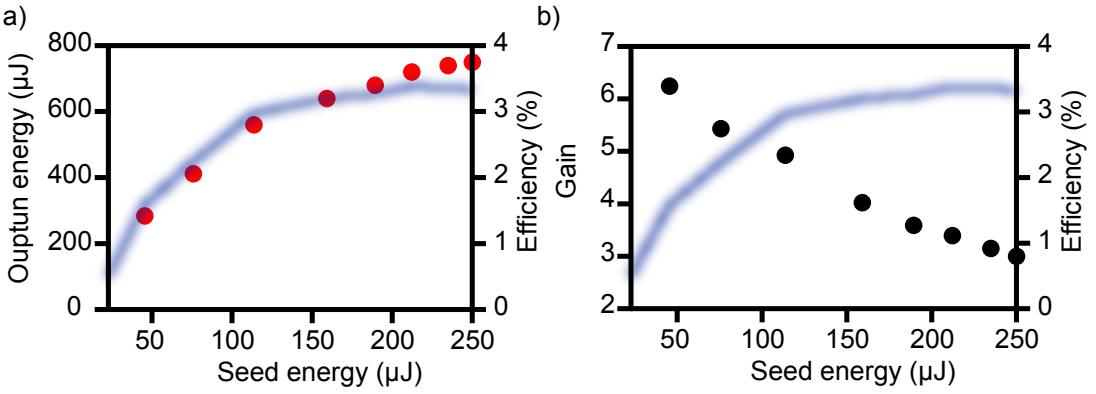

FIGURE 4.10: a) Output energy from the OPCPA as a function of the seed energy for the last stage (red dots). In blue is shown the pump to idler efficiency of the stage. b) The gain curve of the final OPCPA stage (black dots) and the pump to idler efficiency (blue) in function of the seed energy.

4.3.4 Pulse compression in bulk

Thanks to the chirp-inverter, the amplified pulses with positive chirp are back compressed after 3-passes in a 16-cm-long uncoated BaF2 rod. Initially, an SHG-AC was used based on a 1-mm-thick ZGP crystal. However, the enormous background signal detected in the photodiode induced by the mid-infrared high-energy pulses made challenging a clean characterisation of the compressed pulses. Thus, a grating-based InGaAs extended spectrometer was used to reduce the background signal. The extended InGaAs detector is limited to 2.5 μm. Therefore, the characterisation of the 7 μm pulses was carried out using a third harmonic generation (THG) FROG based on a thin ZnSe sample (see appendix A for details). In the spectrometer, we also measured higher harmonics, which were easily subtracted to retrieve the THG-FROG. In Figure 4.11 are shown the harmonics 3^{rd}, 4^{th}, 5^{th}, 6^{th} and 7^{th} measured in the expanded InGaAs spectrometer generated from a polycrystalline ZnSe sample. Moreover, higher harmonics from 7^{th} to 13^{th} were also detected using a silicon detector-based spectrometer.

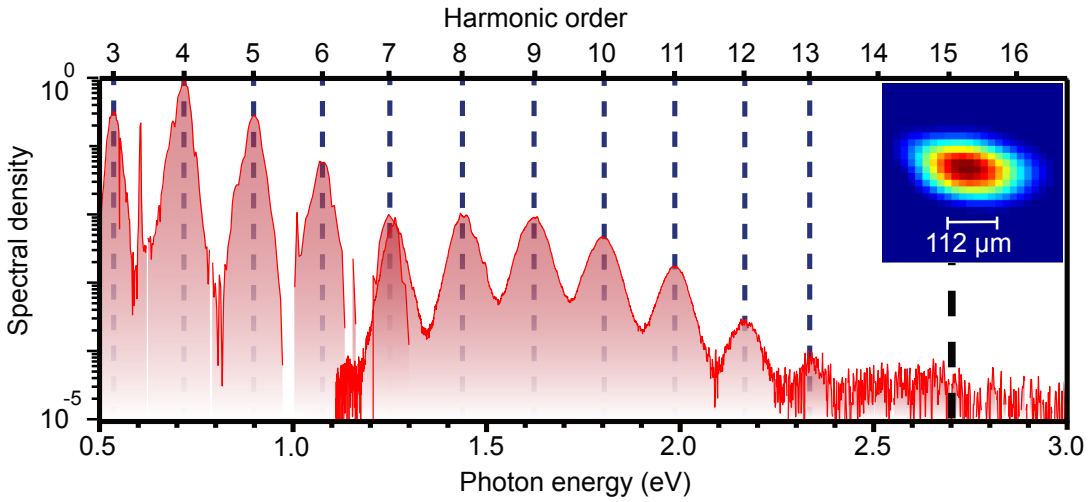

FIGURE 4.11: Measured high-harmonics in a polycrystalline ZnSe crystal (red shadowed line). The dashed blue lines show the harmonic orders of 7 μm and the black thick dashed line refers to the bandgap of the crystal around 467 nm. The inset shows the measured beam profile of the 7 μm pulses at the HHG focal plane.

The compressed high-energy 7 μm pulses out from the OPCPA are focused using a gold-coated $f = 75$ mm off-axis parabolic mirror, and back collimated with an $f = 75$ mm fused plano-convex silica lens. The fused silica lens is used to absorb all the 7 μm beam to protect the detectors and reduce the background noise.

Figure 4.12 shows the measured THG-FROG trace and the retrieved temporal and spectral mid-infrared pulse characteristics. A clear pedestal that expands over the picosecond range can be seen in the measured THG-FROG trace induced by the water absorption lines. The trace was measured at 20% humidity in the pulse characterisation compartment, but the rest of the OPCPA system was purged with dry air. While the absorption lines do not affect the final FWHM duration of the pulses, similar to the 2052 nm pulses, a pedestal is created.

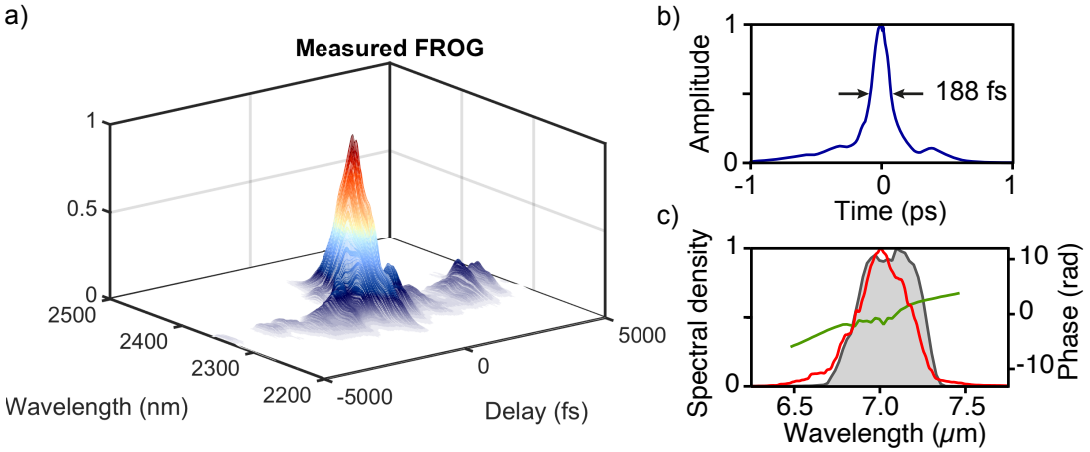

FIGURE 4.12: Characterisation of the 7 μm compressed pulses at the output of the OPCPA. a) measured THG-FROG trace. b) Retrieved temporal intensity shape of the 7 μm pulses. c) Measured (shadowed grey), retrieved spectrum (red) and retrieved spectral phase (green).

The difficulty of compressing the mid-infrared pulses was mitigated by moving the mid-infrared centre frequency from 6.5 μm towards 7 μm, avoiding deepest water absorption lines, as mentioned in the section *"Bright 7 μm generation at 100 MHz,"*

4.4 Conclusions

The new design for the booster CPA with collimated multi-pass geometry and the free-angular-chirp OPCPA with chirp-inverter included enables the development of a tabletop high-energy two-colour system with excellent performance. Moreover, the bright and broadband 7 μm pulses generated via DFG in BGGSe developed in combination with the optically-synchronised EOS set-up enables highly sensitive absorption spectroscopy measurements in the 7 μm mid-infrared regime.

Those results can be used to develop a new system with boosted energies for both 2052 nm and 7 μm pulses. From one side, the energy of the 2052 nm pulses is

expected to increase above 200 mJ using the 130 W 1940 nm Tm: fibre version. Regarding the OPCPA, extra variations are enabled. The high brightness mid-infrared generated in BGGSe enables moving the chirp-inverter to the front-end of the OPCPA. This way, the 7 μm stretched pulse duration can be set from the beginning of the OPCPA, enabling an optimised temporal overlap between the 2052 nm pump pulses and 7 μm pulses. Fewer OPCPA stages would be required, and the required beam path of the 2052 nm beam through the OPCPA would be significantly reduced. This newer design would simplify the mid-infrared 100 Hz OPCPA.

Moreover, BGGSe could be an excellent new candidate for a nonlinear crystal in the OPCPA stages. While ZGP has a much higher figure-of-merit $\sim 206\ pm^2/V^2$ than BGGSe $\sim\ 160\ pm^2/V^2$, the bandgap of the BGGSe is at a much lower wavelength. In general, crystals with higher bandgap energies afford higher peak intensities as the cross-section to achieve MPI is much weaker [154]. Therefore, the OPCPA stages could be pumped with much higher peak intensities. It is estimated that the damage threshold of BGGSe is similar to the damage threshold of GaSe $\sim\ 10^3\ GW/cm^2$ [155]. Thus, the damage threshold of BGGSe is estimated to be more than a hundred times higher than in ZGP, which would decrease the required maximum OPA crystal aperture size and increase the efficiency of the OPA stages significantly (see equation 2.2.34). An OPCPA built with BGGSe crystal could enable the required improvement in amplification efficiency, which using ZGP crystal is limited due to the low damage threshold of the nonlinear crystal.

Chapter 5

High harmonics in the high-T_c superconducting phase

Thanks to the high-brightness harmonic spectrum produced by the 7 μm pulses shown in Figure 4.11, we decided to exploit the advantages of studying high harmonics in solids (HHS) pumped by mid-infrared source. Driving the HHS process with mid-infrared sources enables using a single standard Si-based grating spectrometer to detect multiple harmonics. For instance, harmonics from third to 17^{th} can be detected in a Si-based spectrometer pumped by 3.2 μm pulses. Therefore, sensitive compact schemes can be developed for the investigation of HHS.

Several harmonics can present different intra- and inter-band transition contributions when driven by mid-infrared pulses in materials with bandgaps of few electronvolts. By studying the ratios between intra- and inter-band contributions, charge dynamics inside the medium can be investigated. In the appendix C is shown some of the studies carried out during the PhD to understand more in detail the HHS process. The enhancement of even harmonics dependent on the sample orientation or pump-probe experiments to retrieve the electron-phonon scattering times is shown in this appendix.

In this chapter are shown the investigation on surface harmonics generated in a high-critical-temperature (high-T_c) superconducting YBCO sample. By tunning the YBCO sample temperature from 300 K (room-temperature) down to liquid-nitrogen temperatures, we have studied the harmonic yield behaviour when the superconducting phase is achieved. These studies highlight the HHS yield enhancement when the superconducting phase is reached.

Figure 5.1 shows the schematic design used to generate and detect the studied HHS process. For the cleanest measurements, the HHS was driven by vertically polarised 3.2 μm pulses, and the sample rotated at 45° to detect only the harmonics generated at the YBCO sample's surface. The system is designed to study power-dependent harmonic generation with motorised 3.2 μm pump power control.

The polarisation of the vertically polarised 3.2 μm beam from the output of the OPCPA is varied using a MgF_2 half-waveplate. Afterwards, a wire-grid polariser with extinction ratios higher than 10000 : 1 is used to reduce the 3.2 μm pump power when the motorised half-waveplate is rotated. The wire-grid polariser is set to transmit vertically polarised light. This power-control scheme enables a precise 3.2 μm energy tunning without varying other pulse parameters such as pulse duration or beam size.

The mid-infrared beam is focused to 115 μm waist radius using an $f = 75$ mm gold-coated off-axis parabolic mirror. The mid-infrared beam transmitted through a 400 μm thin uncoated CaF_2 window is focused into the YBCO placed inside the vacuum chamber. The generated harmonics and the mid-infrared beam are reflected in the YBCO surface and ejected from the vacuum chamber at 45° through a second 400 μm uncoated CaF_2 window. Then, the output beam is collimated using an $f = 75$ mm lens and back focused employing an $f = 150$ mm lens. Plano-convex fused silica lenses are used to absorb frequencies above 2.7 μm and thus, block the 3.2 μm beam. The high harmonics generated in YBCO are free-space coupled into the custom-configured Maya2000 Pro spectrometer from Ocean Optics, Inc.

A home built imaging system combined with a digital USB microscope is used to monitor the possible degradation of the YBCO sample. The maximum peak intensity used was kept below 100 GW/cm^2, where we did not experience any degradation or damage in the sample. The imaging system ensures the alignment of the 3.2 μm beam reflecting on the YBCO sample and not on the Copper grid, where the sample was glued. In set-ups where the sample is set at normal incidence (usually for transmission experiments), the integrated light source of the digital USB microscope is enough to image the sample's surface. In our case, as the sample was inserted at 45° for the reflection measurements, a different white light source propagating in the same direction as the mid-infrared beam was required. Therefore, mirrors in foldable mounts were used to propagate the white-light collinear to the 3.2 μm beam when demanded.

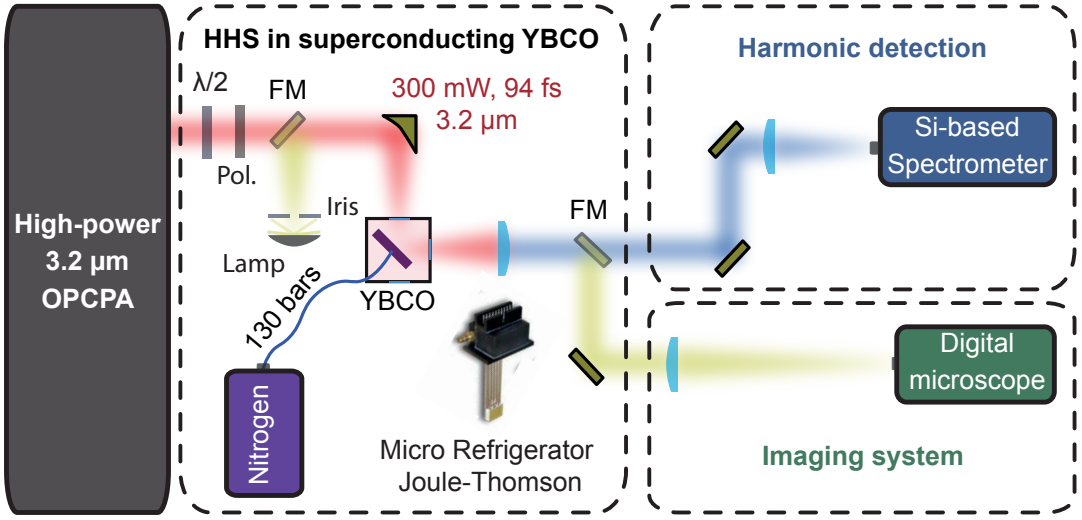

FIGURE 5.1: Schematic set-up for generating and detecting the surface harmonics in the high-Tc YBCO superconductor. The mid-infrared beam is transmitted through a CaF_2 thin window and is focused into the YBCO sample inside the vacuum chamber. A Joule-Thomson micro refrigerator cools the YBCO sample. The generated harmonics ejected from the YBCO at 45° transmitted through a second CaF_2 thin window in the vacuum chamber. The output beam is collimated and back focused into the Si-based grating spectrometer. An imaging system is used to cross-check the YBCO sample status.

The cooling of the YBCO sample is carried out using a Joule-Thomson micro-refrigerator from MMR Technologies, Inc. The micro-refrigerator is based on micro-crystal-fibres, where nitrogen at high pressure is conducted. Therefore, the small aperture size of the crystal fibres drives the compression of the high-pressure nitrogen gas, and liquid nitrogen is produced locally. For this purpose, around 130 bars of nitrogen gas with high purity were required. After the nitrogen flows through the crystal fibres, the nitrogen gas is evacuated from the refrigerator's output. While this method enables a compact cooling system, the cooling capacity is limited to < 300 mW. Therefore, the reduced cooling capacity limited the maximum power allowed to drive harmonics in the YBCO crystal.

Moreover, thanks to the high sensitivity of the Maya2000 Pro spectrometer, quick measurements were acquired, which was required to ensure stable temperatures in the YBCO sample. All the harmonics were measured at once and using integration times of 500 ms. For this purpose, the third harmonic was attenuated using a BG39 Schott Glass Colored Filter. Thus, the third harmonic was filtered to the fifth harmonic signal levels. Thanks to the high dynamic range of the Si-based spectrometer, the seventh harmonic was measured simultaneously.

TABLE 5.1: Temperature-dependent optical properties of YBCO for S polarised 3.2 μm pulses.

Temperature (K)	Dielectric value	Reflectance at 0° (%)	Reflectance at 45° (%)	Skin depth (nm)	Scattering time (fs)
300	$-18.3 + i \cdot 14.6$	76.9	81.0	1186	18
200	$-20.1 + i \cdot 14.3$	78.9	82.6	1197	20.2
100	$-21.5 + i \cdot 14.3$	80.3	83.6	1200	23
85	$-26.7 + i \cdot 19.2$	81.2	85.0	1034	-
70	$-26.7 + i \cdot 102.9$	79.0	84.5	446	-
50	$-30.5 + i \cdot 118.7$	80.2	85.5	416	-

5.1 Properties of high-T_c YBCO

The high-T_c YBCO was grown and provided by our collaborator Dr. Anna Palau from ICMAB-CSIC [156]. A 2.5 mm x 2.5 mm size and 40 μm thin YBCO sample was glued on top of a 3 mm aperture Copper grid with the measured Tc value around 90 K. The superconducting properties of $Y_1Ba_2C_3O_{7-x}$ are sensitive to the value of x. While the $Y_1Ba_2C_3O_6$ has a tetragonal form and is insulating, increasing the oxygen content slightly causes the reduction of the a-axis and elongates the b-axis. Thus, the structure of YBCO becomes orthorhombic with lattice parameters of $a = 3.82$ $\mathring{A}$, $b = 3.89$ $\mathring{A}$, and $c = 11.7$ $\mathring{A}$ [157]. The orthorhombic YBCO becomes superconducting at the liquid-nitrogen temperatures. The highest T_c values in YBCO can be achieved when $x \sim 0.07$, becoming superconductor at 95 K.

To estimate the high harmonic generation in the sample, firstly, the field strength in the sample is required to be calculated, which varies with the sample's temperature. In Table 5.1 are shown the optical properties of YBCO found in the literature for frequencies close to our driving field at 3.2 μm [158, 159].

In Figure 5.2 (a) and (b) are shown the electrical properties of the orthorhombic $Y_1Ba_2C_3O_7$ crystal calculated at $T = 0$ K using the Quantum Espresso software,

based on the density-functional theory (DFT). In Figure 5.2 (c) is shown the structure of the YBCO used in the DFT code for the calculation of the energy bands and the dipole moments.

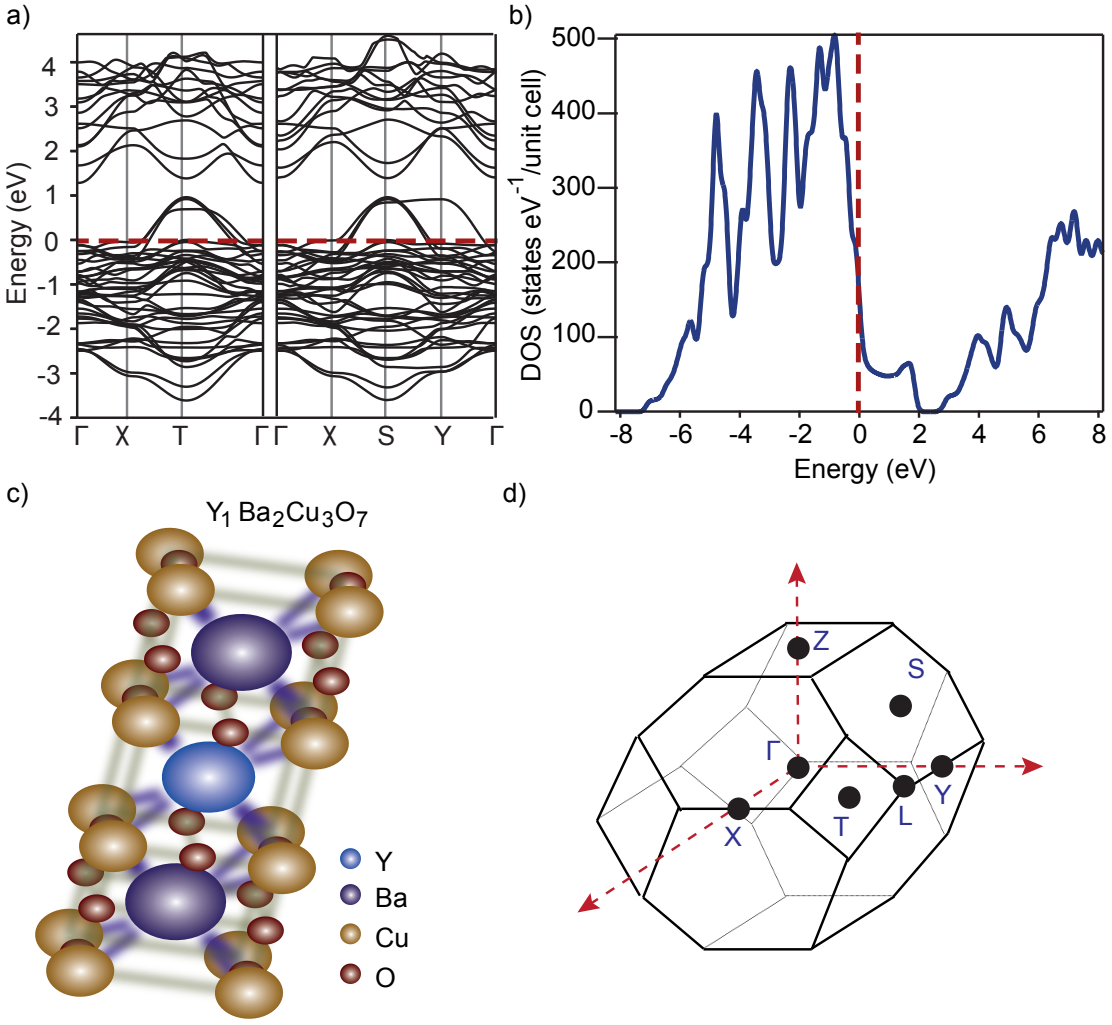

FIGURE 5.2: Structural and electrical properties of the YBCO crystal. a) Band structure for the high-symmetry directions and b) the density of states (DOS) per unit-cell calculated using DFT for the YBCO structure shown in c). In d) is shown the high-symmetry directions of a body-centred orthorhombic structure.

At temperatures above the superconducting regime, band structures and the dipole moments calculated from the DFT can be used in combination with the theory described in section *"Quantum view"* to predict the high harmonic behaviour. Moreover, the temperature variations can be estimated by varying the scattering time in equation 2.3.15. The calculations can be reduced to a single valence band and a single conduction band for simplification purposes. The inter-band transitions from the valance band to the conduction band can be easily calculated using the dipole moments calculated from the DFT code. Moreover, the induced currents inside the crystal (intra-band transitions) can be simplified to

hole-charge currents induced in the valance band and electron currents generated in the conduction band:

$$J(t) = -2\{f_e v_c + f_h v_v\} \tag{5.1.1}$$

where $f_{e,h}$ is the electron/hole density in the conduction/valance band calculated from inter-band transitions, and $v_{c,v}$ is the group velocity calculated from the derivative of the energy bands.

At temperature values lower than the T_c, the superconductivity is reached, and band splitting close to the Fermi level is produced. The critical current J_c describes the maximum current that a superconductor can sustain before developing resistance. The superconductivity state will be broken if the J_c value in the superconducting band is exceeded. In general, there can be two contributions to the current flowing on the surface of a superconductor. From one side, there is the contribution of the electron charges transported through the superconducting surface. From the other side, we have the screening currents induced by applied magnetic fields:

$$J_T = J_I + J_H \tag{5.1.2}$$

where J_I is the current related to intra-band transitions, and J_H is related to the currents induced by magnetic fields. The superconductivity would be lost if $J_T > J_c$.

Figure 5.3 shows the J_c value for different temperatures measured and provided by our collaborator Dr. Anna Palau. At $J_T = 0$ the critical temperature is determined to be around 90 K, while at higher applied currents, lower temperatures are necessary to reach the superconducting state.

The estimated current density induced in the conduction band from equation 5.1.1, is $\sim 0.2\, TA/m^2$. While this value is an order of magnitude higher than the J_c value around 80-90 K, the current density value is estimated from the original conduction band above T_c. The value of the current induced in the superconducting splitted band is unknown. Therefore, a complete simulation of electron dynamics in the superconducting phase would be required to estimate J_T appropriately. Moreover, based on the dipole moment approximation, the current screening induced by the mid-infrared magnetic field is neglected in those calculations [160].

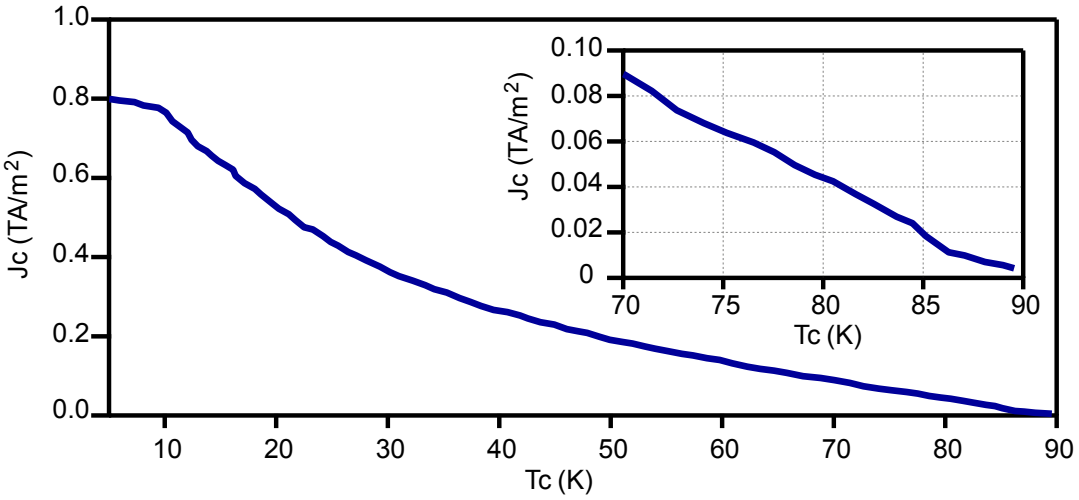

FIGURE 5.3: Measured critical current-density dependency (J_c) on the critical temperature of the YBCO sample. In the inset is shown zoom-in the regime our superconductivity measurements were carried out.

In any case, comparing the $T_c \sim 90$ K shown in Figure 5.3 with the high harmonic results in Figure 5.5 with $T_c \sim 85$ K, it could be that we already were generating currents in the superconducting phase that were shifting slightly the T_c value. The lack of a theory for light-matter interaction in high-T_c superconducting states has encouraged us, in collaboration with the group of Prof. Dr. Maciej Lewenstein at ICFO, to find a theory based on the experimental results shown in the following sections.

5.2 High harmonics in YBCO

In the last decade, numerous experiments have been carried out in nanostructured mediums to enhance the HHS process and generate higher photon fluxes close to the UV regime. The absence of any theoretical model that could predict the HHS process in high-T_c superconductors encouraged us to study the process to look for new approaches that could enhance the HHS process. Therefore, we have investigated the power and temperature dependencies of the produced harmonics at the surface of the high-T_c YBCO.

5.2.1 Power dependency of the harmonics

The power dependency of the surface harmonics generated in the YBCO sample at room temperatures and in the superconducting phase (at 80 K) is studied in

this section. Figure 5.4 shows the 3.2 μm pump peak intensity dependency on the generated 3^{rd}, 5^{th} and 7^{th} harmonic intensities. While the third harmonic rises quicker at room temperatures, the fifth and seventh harmonics are boosted quicker when the superconducting phase is reached. Moreover, the seventh harmonic generated at room temperature reaches the saturation of the maximum yield around 600 TW/m^2, while at the superconducting phase, the same harmonic keeps rising at 900 TW/m^2 pump intensities. This effect is weaker in the fifth harmonic, but as can be seen in Figure 5.4, also this harmonic reaches the saturation point around 850 TW/m^2 at room temperatures.

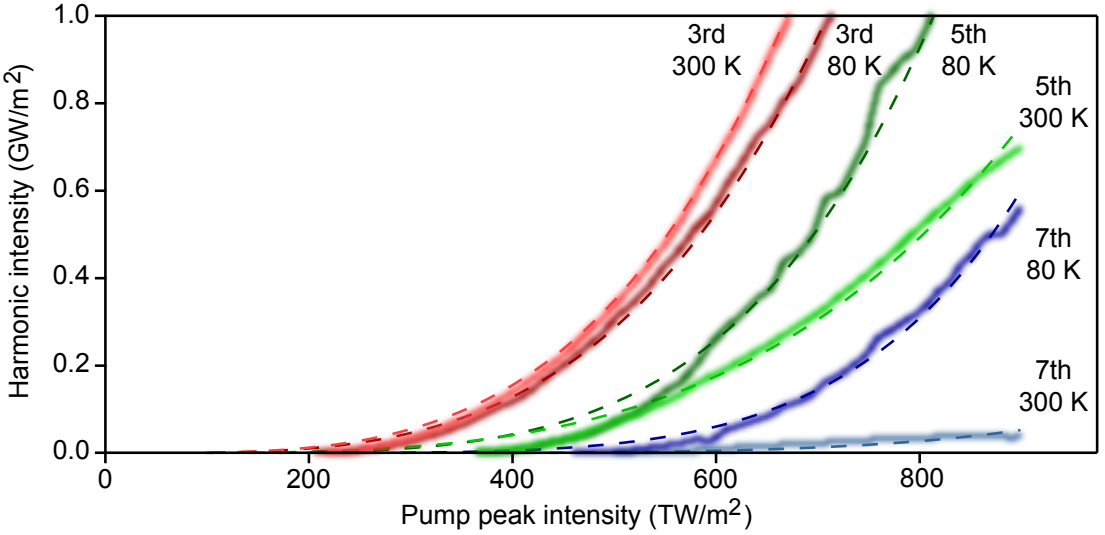

FIGURE 5.4: Power dependency of 3^{rd} (red curve), 5^{th} (green curve) and 7^{th} (blue) harmonic generated at the surface of the YBCO sample at room temperature (light colours) and when the superconductivity state is reached at 80 K (dark colours). With dashed lines are shown the Bessel function fittings using the equation 2.4.8.

In Figure 5.4 with dashed lines are shown the fitted curves using the equation 2.4.8 deduced from the classical HHS point of view. The YBCO sample is rotated at 45°, and the 3.2 μm driving field is vertically polarised to avoid HHS dependency on the YBCO angle. Thus, the harmonics are generated in the a/b plane. Table 5.2 shows the fitted values of the first-kind Bessel orders (J_N) and the lattice-parameter retrieved from the curves shown in Figure 5.4. As the harmonics are generated in the a/b plane, the lattice parameter retrieved should be close to $a = 3.82$ $\mathring{A}$ or $b = 3.89$ $\mathring{A}$ distances in the YBCO orthorhombic structure. Unfortunately, the Bessel function fitting error is larger than the difference between the values of a-axis, b-axis and c-axis in the YBCO orthorhombic sample.

In principle, from the classical point of view, the Bessel order should be an integer number and should match the harmonic order. Experimentally the results achieved

TABLE 5.2: Bessel function fitting coefficients extracted from the power dependency measurements at 300 K and 80 K.

Temperature (K)	Harmonic (#)	Bessel (#)	Lattice parameter ($\mathring{A}$)	Power (#)
300	3	3.6	3.29	3.4
80	3	3.6	3.13	3.3
300	5	3.6	3.97	3.7
80	5	4.4	4.13	4.6
300	7	4.4	3.90	4.8
80	7	5.5	4.20	6.5

show that a real Bessel number is required to fit the measured power dependency of the harmonics. Moreover, while the calculated Bessel order for the 3^{rd} harmonics is higher than 3, for fifth and seventh harmonics, the Bessel order is lower than the harmonic order.

The typically used fitting expression $I(N\omega_0) \propto I^N$ is an approximation of the Bessel functions. This expression can be achieved by expanding the Bessel functions into the powers of the driving electric fields as follows:

$$J_N\left(\frac{\Omega_B}{\omega_0}\right) = \sum_{m=0}^{\infty} \frac{(-1)^m}{m!\Gamma(m+N+1)} \left(\frac{eaE}{2\omega_0\hbar}\right)^{2m+N} \tag{5.2.1}$$

If we approximate the expansion to the first order of the summation, we get that the harmonic yield increases with $I_N(N\omega_0) \propto \left|J_N\left(\frac{\Omega_B}{\omega_0}\right)\right|^2 \propto I^N$. Thus, the generally used power relation to predicting the harmonic signals in the function of the driving pump intensity is recovered from weak pump intensities.

In the last column of Table 5.2 is shown the fitting power coefficients retrieved from the measurements shown in Figure 5.4. The N coefficient retrieved from the Bessel function fitting and power relation fitting agree qualitatively on the behaviour of

the harmonics generated in the YBCO sample, at room temperatures, as well as in the superconducting phase.

5.2.2 Temperature dependency of the harmonics

In Figure 5.5 is shown the temperature dependency of the HHS generated at the surface of the YBCO at the maximum driving mid-infrared field allowed by the cryo-micro-refrigerator and the critical current-density ($I = 900\ TW/m^2$ or $E = 0.083\ V/\AA$ in vacuum). While the driving field signal does not vary substantially with temperature, the signals of the third, fifth and seventh harmonics vary significantly. Those variations increase with the harmonic order. The highest variations are measured below the T_c value, where all the harmonics are enhanced. For instance, at the seventh harmonic, an enhancement of more than an order of magnitude is achieved.

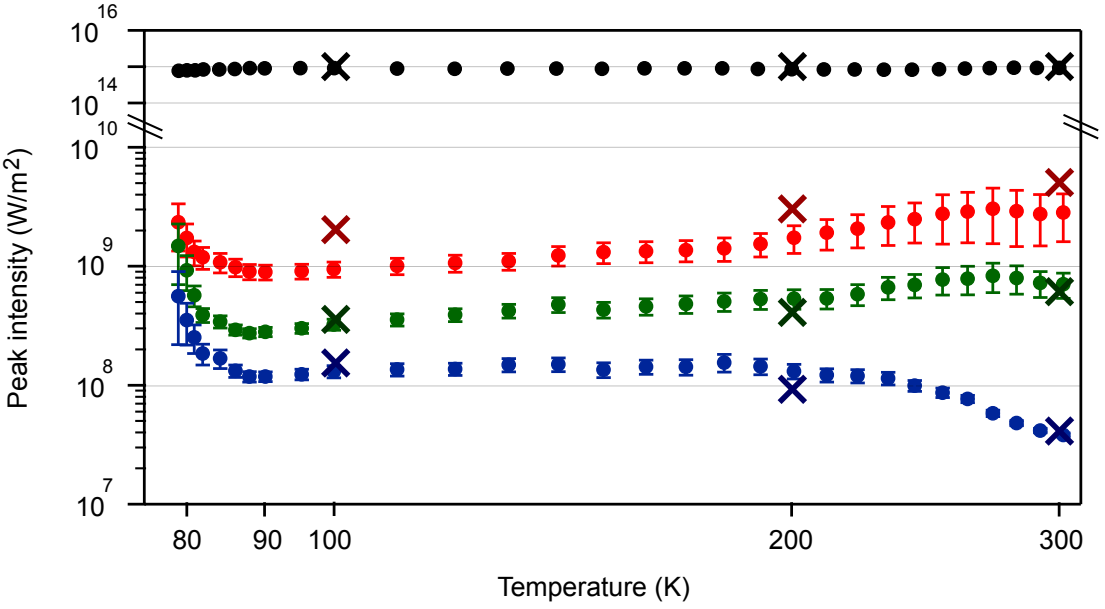

FIGURE 5.5: Measured temperature-dependent harmonic intensity for 1^{st} (black dots), 3^{rd} (red dots), 5^{th} (green dots) and 7^{th} (blue dots) harmonics. With crosses are shown the predicted harmonic intensities above the superconducting state for fundamental (black-crosses), third (dark-red cross), fifth (dark-green cross) and seventh (dark-blue cross) harmonics.

Above the T_c value, the real part of the dielectric function and the scattering time increase while temperature decreases (see Table 5.1). Higher scattering times promote higher efficiencies for higher harmonics, while lower harmonic signals are slightly attenuated. Therefore, the signal of the third and fifth harmonics decrease from 300 K to 100 K, while the 7^{th} harmonic signal increases.

In Figure 5.5, with crosses, the estimated harmonic intensities are represented, taking into account intra- and inter-band transitions. The harmonic signal dependent on temperature was successfully estimated by considering the temperature-dependent variations of the dielectric function and the scattering time. Moreover, from the simulations, we could conclude that the intra-band transition contribution to the fifth and seventh harmonic was minor.

At lower temperatures than the T_c value, when the superconductivity phase is achieved, the scattering time and the imaginary part of the dielectric function rise exponentially. Moreover, the real part of the dielectric value stays unvaried. As shown in Figure 5.5 below T_c ($\sim$ 85 K), all the harmonics grow exponentially. Unfortunately, we could only measure down to 78 K as we were limited by the liquid-nitrogen temperatures achieved in the micro-refrigerator.

5.2.3 Harmonic centre frequency blue-shift

The harmonic centre frequency shift is a footprint of the strong electron dynamics induced by the mid-infrared pulses inside the medium during the harmonics generation process [100]. In Figure 5.6 is shown the characterisation of the harmonic centre frequency blue-shift, which increases with the pump intensity. The pump mid-infrared spectrum is centred at $\lambda_c = 3195$ nm ($E = 388$ meV). Thus, the centre frequencies expected for the 3^{rd}, 5^{th} and 7^{th} harmonics would be $\lambda_c^3 = 1065$ nm ($E = 1164$ meV), $\lambda_c^5 = 639$ nm ($E = 1940$ meV) and $\lambda_c^7 = 457$ nm ($E = 2713$ meV) respectively.

As shown in Figure 5.6 (a), at weak enough pump intensities, it would be expected that the measured harmonics' centre frequency would converge to the estimated centre frequencies shown with dashed lines. Moreover, the maximum frequency shifts measured are still inside each harmonic's estimated FWHM spectral bandwidth. For instance, while the FWHM spectral bandwidth estimated for the third harmonic expanse from 1120 meV to 1200 meV, the maximum centre frequency shift measured is of 1190 meV ($\Delta E \sim 28$ meV). The FWHM bandwidth of the fifth-harmonic expanse from 1880 meV to 2000 meV with the maximum frequency shift of $\Delta E \sim 28$ meV. Moreover, the FWHM bandwidth of the seventh-harmonic expanse from 2620 meV to 2800 meV and the maximum frequency shift measured is $\Delta E \sim 50$ meV. Therefore, while frequency shifts are generated, the new centre frequency remains inside the initially estimated harmonic FWHM spectral bandwidth.

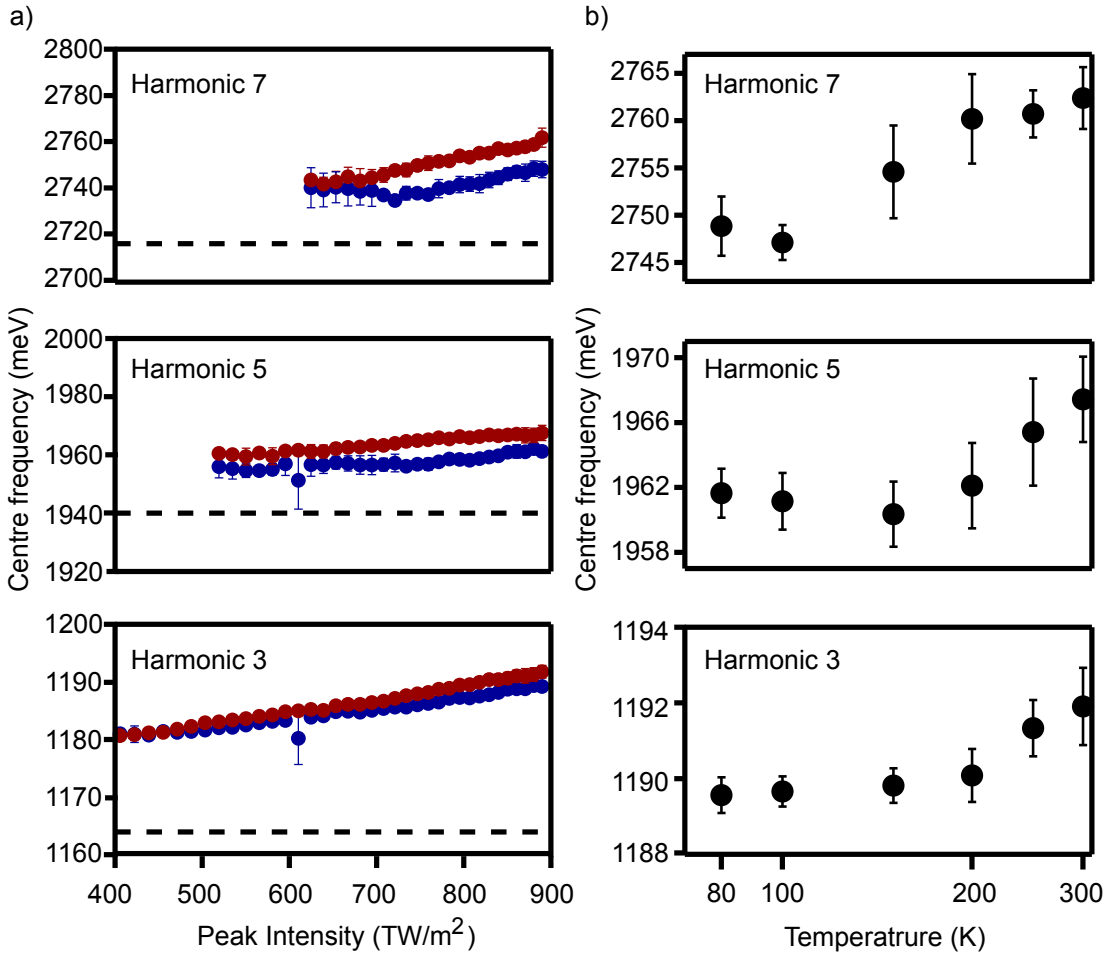

FIGURE 5.6: a) Measured centre frequency shift dependence on the pump intensity for third, fifth and seventh harmonics. Blue dots and red dots indicate the centre frequency values measured at 80 K and 300 K, respectively. The black dotted lines show the centre frequency calculated as $\omega_c = N\omega_0$. b) Measured temperature dependency of the harmonic centre frequency.

Figure 5.6 (b) shows the harmonic centre-frequency variation in function of the temperature in the YBCO sample. Interestingly, the blue-shit is weaker at the superconducting state than at room temperatures. However, the centre frequencies of the harmonics are still blue-shifted at the lowest temperatures. The production of weaker blue shifts at lower temperatures could be related to reducing electron-electron scattering processes, which would agree with the larger scattering times expected in the superconducting phase.

5.3 Discussion

One of the limitations of harmonic amplification from nanostructures is the enhancement decrease experienced at the highest peak intensities [161]. While nanostructures can enhance the fields to achieve higher efficiencies in the HHS process, they are limited by the low scattering times.

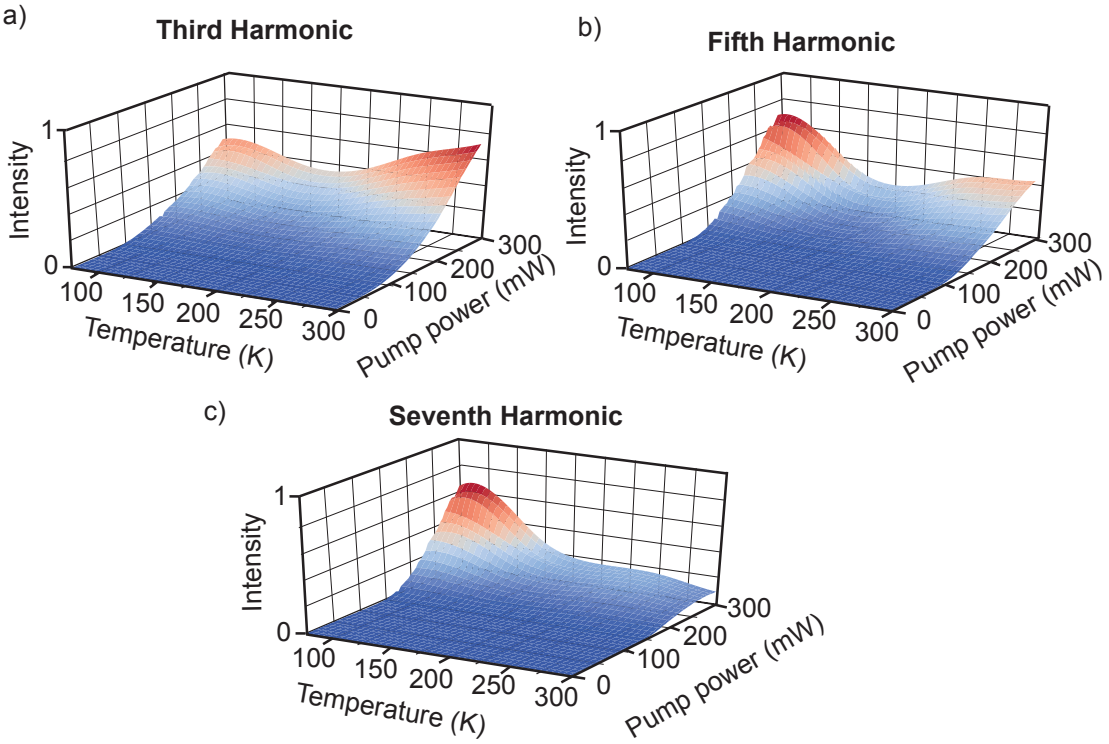

FIGURE 5.7: Power and temperature dependency of the a) third, b) fifth and c) seventh harmonics in the surface of the high-Tc YBCO. The temperature dependency is presented from room temperatures down to 78 K crossing the phase-change from insulating to the superconducting state.

In high-T_c superconductors, we have demonstrated that the electron-electron scattering is significantly reduced below T_c. Therefore, harmonic saturation is avoided, and weaker blue shifts are generated in the superconducting phase. In this chapter, we have demonstrated the exponential rise of the harmonics generated in the superconducting phase of a high-T_c superconductor. We have shown that the highest amplifications are promoted at the highest harmonics, where yields at seventh harmonic as high as third and fifth harmonic yields have been measured.

Figure 5.7 shows the power and temperature dependency behaviour of the third, fifth and seventh harmonics generated in the surface of our YBCO sample. As shown in Figure 5.7, the power range used for pumping the YBCO sample does not vary the T_c value, which implies that the current generated in the superconducting

state is lower than the J_c value. While the harmonic yields show an exponential rising from 85 K to 78 K remains open the question of at which temperatures would saturate the harmonic amplification, or if the harmonic yield would exponentially grow down to the liquid-Helium temperatures (4 K). The efficiency of the harmonics generated in bulk surfaces used to be especially weak ($10^{-4}\%$), but if the rising trend measured in the superconductivity phase would keep rising exponentially, remarkable efficiencies could be enabled. The theory developed by the group of Prof. Dr. Maciej Lewenstein at ICFO attempts to illustrate the HHS process in the high-T_c superconducting phase and predict harmonic amplification at lower temperatures than the temperatures achieved experimentally in this chapter.

Experimentally, pump-probe measurements can be used to characterise electron-electron, electron-phonon and phonon-phonon scattering time variations with temperature (see appendix C). Moreover, new experiments could be carried out to analyse possible T_c shifts at higher pump peak intensities and study the phase change region more in detail. Finally, retrieving Berry curvatures [162] or energy-bands close to the Fermi energy [163, 164] are features that high harmonics have encrypted in their generation process and could be retrieved from the HHS signal.

Chapter 6

Summary and Outlook

This thesis shows the generation of intense, few-cycle, mid-infrared pulses based on extreme nonlinear processes. The main results can be summarised as follows: (i) the development of a mid-infrared OPCPA delivering single-cycle few-GW-level pulses at 160 kHz, (ii) the generation of bright, multi-octave, CEP-stable source expanding from 340 nm to 40 μm at 160 kHz, (iii) the development of a mid-infrared OPCPA delivering 700 μJ of ultrafast 7 μm pulses at 100 Hz, and (iv) harmonic enhancement in high-T_c YBCO superconductor.

6.1 Single-cycle 3.9-GW mid-infrared pulses at 160 kHz

We have demonstrated a novel architecture for efficient OPCPA development that produces GW-level 3.2 μm pulses. Although nowadays there are more powerful pump lasers with shorter pulse durations commercially available, the novel design of the OPCPA has enabled the amplification of 3.2 μm seed pulses with exceptional efficiencies, achieving record powers of ultrashort 3.2 μm pulses. Moreover, we have proved the strength of the novel mid-infrared ARR-PCF by achieving near-single-cycle mid-infrared pulse compression and triplicating the peak powers delivered from the OPCPA. This system combines the highest average power with a single-cycle duration in the mid-infrared regime. Furthermore, it presents a significant step forward for generating coherent X-rays in the kilo-electron-volt regime via HHG in noble gases.

The HHG in noble gases requires peak intensities typically in the $10^{14}-10^{15}$ GW/cm^2 range. Moreover, the low ionisation cross-sections of the noble gases in the mid-infrared regime and the unfavourable wavelength scaling nature of the harmonic generation demand peak intensities close to 10^{15} GW/cm^2. Therefore, the generated single-cycle mid-infrared pulses should be focused down to a 15 μm waist radius to achieve the expected petawatt peak intensities, which at the same time increases the technological challenge of creating X-rays in the kilo-electron-volt regime.

Simulations carried out to predict soliton compression and DW generation highlight the extreme peak intensities that can be achieved inside the ARR-PCF. These simulations estimate peak intensities of up to 60 TW/cm^2 inside the 92 μm core ARR-PCF driven by less than 20% of the full OPCPA output [68]. Therefore, tapering our ARR-PCF [165] can enable us to achieve petawatt intensities at larger mid-infrared beam sizes, thus easing the technological challenges for the generation of kilo-electron-volt X-rays driven by mid-infrared pulses.

6.2 Bright multi-octave CEP-stable sources at 160 kHz

The ultra-broadband spectrum and ultraviolet DW generation have been demonstrated by driving extreme soliton dynamics inside the mid-infrared ARR-PCF. By tuning the gas pressure inside the gas cell, the soliton compression is regulated for DW generation in the ultraviolet regime, expanding the ARR-PCF output from 340 nm to 6 μm.

Simultaneously, the generated mid-infrared soliton is employed to drive the IP-DFG process in the newly developed BGGSe mid-infrared nonlinear crystal. The high efficiency provided by the BGGSe crystal combined with the considerable acceptance bandwidth provided has enabled us to produce CEP-stable, sub-3-cycle, mid-infrared pulses expanding from 6 μm to 40 μm.

The combination of the ultraviolet DW, ultra-broadband near-single-cycle mid-infrared supercontinuum, and the sub-3-cycle mid-infrared pulses from the IP-DFG creates a sub-100 fs seven-octave expanded CEP-stable source at 160 kHz. The ultra-broadband source leads to multidimensional spectroscopy experiments such as light-matter interaction studies in solid-state physics or absorption peak characterisation for chemical identification.

6.3 High-energy 7 μm OPCPA at 100 Hz

We have demonstrated the development of the 7 μm OPCPA at 100 Hz based on the previously developed 3.2 μm OPCPA architecture. This thesis shows the energy scaling of the mid-infrared pulses, achieving compressed 7 μm pulse energies up to 700 μJ pumped by 21.7 mJ of optically synchronised homebuilt 2052 nm pulses. For OPCPA optimisation purposes, the chirp of the stretched 7 μm pulse is tailored and back-compressed efficiently using a BaF_2 dielectric bulk rod.

Even with the upgraded system, the 7 μm pulse energies are still limited for coherent X-ray generation due to the harmonic generation's unfavourable wavelength scaling nature. On the other hand, the 2.9 μm signal wave generated in the 7 μm OPCPA reaches uncompressed energies of 1.5 mJ. These energies are ten times higher than those obtained in the 3.2 μm OPCPA at 160 kHz. Thus, the 2.9 μm pulses generated in the 7 μm OPCPA have the potential to generate kilo-electron-volt radiation at moderate noble gas pressures.

Moreover, the newly studied mid-infrared BGGSe nonlinear crystal enables new opportunities to develop the 7 μm OPCPA with optimised efficiencies. The intense 7 μm pulses generated via DFG in the BGGSe crystal can be directly aligned in the Martinez stretcher. Thus, the losses induced by the Martinez are reduced, and the 2052 nm pump propagation is minimised.

Furthermore, BGGSe could be a new candidate to boost the efficiencies in the OPCPA stages, which are nowadays limited by the low damage threshold of the ZGP crystals. While BGGSe provides a slightly lower figure-of-merit value (see Figure 1.3), it is expected to afford higher damage thresholds. Therefore, BGGSe can boost the final OPCPA stage's efficiency, increasing the final mid-infrared pulse energy. For instance, efficiencies of up to 10% in the last booster stage pumped by 2052 nm 100 mJ pulses would enable 7 μm amplifications up to 10 mJ. While ZGP's low damage threshold prevents it from pumping the final stage with such high energies, higher damage thresholds in BGGSe may allow it to use the entire available 2052 nm pump energy.

6.4 Enhancement of harmonics in high-T_c YBCO

We have demonstrated the harmonic enhancement at the surface of the high-T_c YBCO superconducting state. The saturation of the harmonic intensity and the

blue-shift of the harmonic centre frequency are both reduced below T_c. Moreover, the full intra-band and inter-band simulations conducted show that the 5^{th} and 7^{th} harmonics are produced mainly from inter-band transitions. Therefore, the Bessel orders retrieved for the 5^{th} and 7^{th} harmonics are expected not to match the harmonic order. These results match the Bessel order fittings shown in appendix C, where the Bessel order of the 9^{th} harmonic generated above bandgap in ZnSe does not match the harmonic order. On the other hand, the harmonics generated below the bandgap in ZnSe, expected to be produced from intra-band transitions, give a good match between the Bessel order and the harmonic order.

Furthermore, it has been shown that higher harmonics are more sensitive to the favourable properties of the superconducting state, showing an exponential increase in the harmonic intensity on the YBCO surface. The exponential rise is proven from 90 K to 80 K, but harmonic behaviour at lower temperatures is not yet certain. A Liquid-Helium-based cryo-cooling system could enable studying the harmonics' enhancement down to 4 K and clarify the behaviour at lower temperatures. Moreover, pump-probe experiments could be carried out to learn more about those high-T_c superconductors and their behaviour through phase transitions.

Appendix A

Pulse characterisation

This appendix describes the pulse characterisation techniques used to characterise pulses with different frequencies, bandwidths, and durations developed during the PhD. Various autocorrelation schemes have been used depending on the pulse characteristics. While narrowband picosecond pulses are insensitive to the dispersion introduced by possible transmission optics in the characterisation set-up, they require stable beam pointings during long temporal delays (up to 25 mm). On the other hand, near-single-cycle pulse characterisation can be carried out at shorter temporal delays, but transmission optics should be avoided. Therefore, for long pulses, a Michelson interferometer with a transmission beam splitter and a corner cube for highly stable temporal delays is typically used. For single-cycle broadband pulses, an all-reflective-optics based characterisation scheme is crucial to be used, even if the beam pointing is limited to stage travels of a few millimetres.

For SHG-intensity autocorrelation, SHG-FROG or THG-FROG, two identical pulses are required to be temporally and spatially overlap in a nonlinear crystal where SHG or THG is generated. A second harmonic beam propagating together with its fundamental beam is generated from each replicated pulse. Moreover, a sum-frequency beam is also generated with the two replicated pulse contributions. The nonlinear process is generated in non-collinear geometry to avoid interferences between the three waves at the SHG frequency. Thus, the SFG beam is propagated in the middle between the two SHG beams that can be filtered using an iris or slit. In the THG-FROG, four waves at the THG frequency are generated, two of them propagating collinearly with the fundamental pulses and two more between the fundamental beams. The THG-FROG trace can be measured by recording one of the middle THG signals using the corresponding spectrometer.

A Michelson interferometer type scheme is typically used for the generation of two identical pulses. The fundamental beam is generally split into two beams using a pellicle type beam-splitter or cutting the beam in two using D-shape reflection optics or prisms. Afterwards, one arm is back-reflected towards the beam splitter in a fixed mirror. In contrast, the other arm is back-reflected using a movable mirror built in a translation stage. The temporal delay between the replicated pulses is varied by changing the length of the Michelson moveable arm. For high pointing stabilities, the back-reflection of the movable arm is carried out using a corner cube.

Once the nonlinear process is generated and the unnecessary beams are filtered, the nonlinear signal is back focused on the detector entrance. A photodiode can be used to measure SHG-intensity autocorrelations. Moreover, a spectrometer is used for FROG measurements.

The SHG-intensity traces are required to be symmetric in time as the convolution of replicated pulses is measured. Therefore, while the THG-FROG provides complete temporal information, the SHG-autocorrelation or SHG-FROG is required to be symmetric, and thus, the temporal direction becomes ambiguous. The symmetry of the SHG traces can be used to ensure that the pulse characterisation measurement has been taken correctly. Spatial overlap variations induced by the translation stage, generation of extra pulses (with different propagation directions) in one of Michelson's arms or spatially chirp pulses can introduce asymmetric traces. Wavefront tilts or spatial chirps can be produced inside the nonlinear crystal when the non-collinear geometry is too large. The wavefront tilt effects increase with broader pulses. Therefore, it is crucial to minimise the non-collinear angle in the characterisation set-up to characterise ultra-broadband pulses.

Figure A.1 shows the different autocorrelation schemes used during the PhD for SHG-FROG (a) and (b), SHG-intensity autocorrelation (c) and (d), and THG-FROG (d). The scheme shown in (a) is typically used in ultrafast pulse characterisation. It is based on a Michelson interferometer with one arm spatially shifted to generate the non-collinear geometry. The two parallel arms are reflected towards the off-axis parabolic mirror, and the spatial overlap is only achieved at the focal plane, where the nonlinear crystal is placed. The pellicle beam-splitter is based on a thin membrane with one of the surfaces coated to ensure 50/50 beam splitting. If an inappropriate pellicle is used, the coating fails, and the reflections in the coating become comparable to the Fresnel reflections in the uncoated surface.

More than a single pulse is propagated in one of the arms, and asymmetric FROG or autocorrelations are measured.

Figure A.1 (a) type schemes provide robust SHG-FROG measurements for few-cycle pulse characterisation. The 97 fs 3.2 μm pulses out of the 160 kHz OPCPA are measured using this set-up (see Figure 3.7). For broader and shorter pulse characterisation, non-collinear angles introduced by the corner cube in (a) can be too large, inducing significant wavefront tilts resulting in an asymmetric SHG-FROG trace.

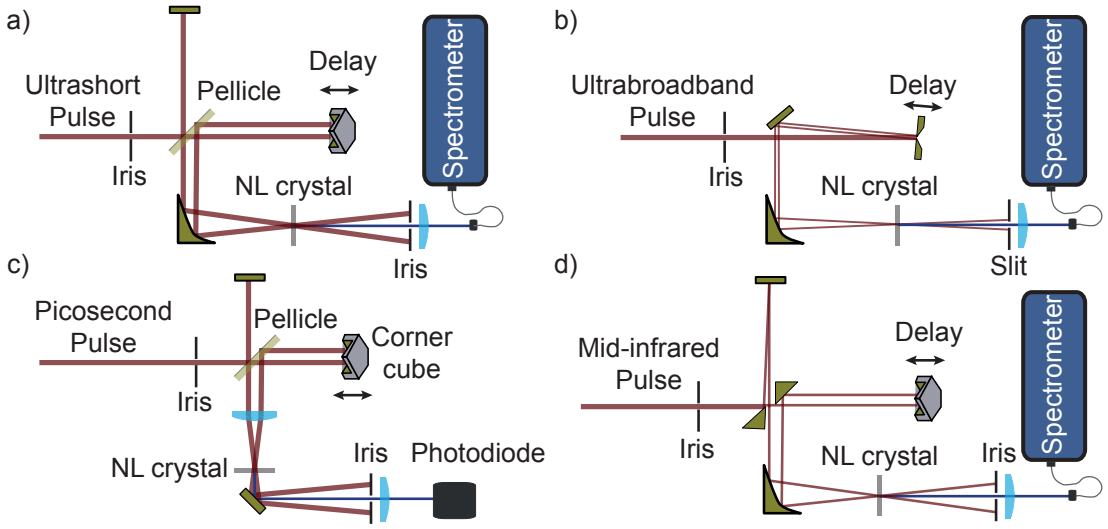

FIGURE A.1: Pulse characterisation schemes optimised for different pulse parameters. a) SHG-FROG set-up for few-cycle pulse characterisation. b) SHG-FROG layout for ultra-broadband single-cycle pulse characterisation with reduced non-collinear angles. c) Autocorrelation set-up for characterisation of narrowband picosecond pulses. d) THG-FROG scheme for few-cycle mid-infrared pulse characterisation.

A new SHG-FROG set-up was built to characterise the near-single-cycle 3.2 μm pulses. Figure A.1 (b) layout minimises the wavefront tilts generated in the nonlinear crystal and avoids using pellicles. Thus, the second layout is suitable for ultra-broadband single-cycle pulse characterisation (see Figure 3.12). Unfortunately, in this scheme, D-shape flat mirrors are used for the delay line instead of corner cubes limiting the travelling distance with stable beam pointings to a few millimetres.

Figure A.1 (c) shows the SHG-intensity autocorrelation set-up used to characterise the 2052 nm pulses (see Figure 4.3). While the layout is similar to (a), the off-axis parabolic mirror is replaced by a simpler plano-convex lens. The achromatic

dispersion and chirp introduced by the plano-convex lens are negligible for the narrowband 2052 nm pulses.

The characterisation of the stretched 7 μm pulses via SHG-intensity autocorrelation (see Figure 4.8) or the characterisation of the compressed ultrafast 7 μm pulses via THG-FROG (see Figure 4.12) is carried out using the layout shown in Figure A.1 (d). Pellicles are not typically available at long wavelengths. Thus the beam is spatially split using gold-coated prisms. While the scheme in (b) also uses all-reflecting optics, it is not suited to characterise picosecond pulses. As the bandwidth of the compressed 7 μm pulse is narrow enough to neglect wavefront tilts, larger non-collinear angles than in (b) can be used.

In all these schemes, it is necessary to ensure that the split beams are propagated parallel to the focusing optics. Then, both beams are focused in the same plane, and the highest nonlinear signals are achieved.

The spectral characterisation is conducted using different instruments depending on the spectral region required to be measured. The visible/near-infrared spectrum from 180 nm to 1100 nm is measured using an HR4000 or MayaPro spectrometers from Ocean Optics Inc. The near-infrared regime from 900 nm to 2550 nm is measured using the extended InGaAs NIR256 spectrometer from Ocean Optics Inc. An FTIR from Newport is used to characterise the spectral content from 1.6 μm up to 16 μm of waves with repetition rates higher than 10 kHz. The scanning stage frequency limits typically the lowest repetition rates retrieved with the FTIR. Thus, for the spectral characterisation of the 100 Hz 2052 nm and 7 μm pulses, a monochromator from Newport is used. While visible spectrometers and the FTIR provide sub-nanometric frequency resolution and present incredible sensitivities, the extended InGaAs spectrometer and the monochromator specs are more restricted.

The EOS technic is used for direct measurement of the mid-infrared electric fields. The EOS set-up used to characterise the 7 μm pulses at 100 MHz (see Figure 4.5), and mid-infrared pulses generated via IP-DFG at 160 kHz (see Figure 3.17) is shown in Figure 3.16. A linear piezo stage with nanometric resolutions and 12 mm travelling distance from SmarAct GmbH is used to vary the temporal overlap between pump and probe pulses. A half-inch corner cube is employed to ensure a stable pointing during the mid-infrared electric field measurement.

The main challenge in developing an EOS set-up is the generation of optically synchronised probe near-infrared sub-20 fs pulses. The probe pulses for the characterisation of the 7 μm pulses are generated from the recycled 70 fs, 1.55 μm pulses through BGGSe. The broadening of the 1.55 μm is generated using the NL-1550-NEG1 PCF from NKT photonics. The NL-1550-NEG1 PCF is an all-normal dispersion PCF with a 3 μm solid-core diameter and designed to be used with 1.55 μm pulses. The broadening of the 1.55 μm pulses is produced in a 20 cm long fibre where powers of 22 mW at 100 MHz are coupled with 25% coupling efficiencies. The broadened 1.55 μm pulses are then compressed down to 21 fs using a pair of fused silica wedges.

The probe pulses used for the characterisation of the IP-DFG pulses at 160 kHz are generated by frequency doubling the ARR-PCF output 30 fs, 3.2 μm pulses. The SHG is produced in a 400 μm thin AR coated AGS crystal. The dispersion introduced by the AGS crystal is post compensated by adding an extra 12 mm thick BK7 window achieving pulse durations of 22 fs at the 1.6 μm. The same 3.2 μm pulses are used for the IP-DFG, thus minimising the optical beam path from mid-infrared pulse generation to its characterisation via EOS.

In both set-ups, the pump and probe pulses are combined collinearly using a 0.5 mm thin silicon wafer and focused in a 30 μm GaSe crystal using a gold-coated off-axis parabolic mirror. The mid-infrared pulses change the GaSe crystal's birefringence, which simultaneously changes the probe pulse's polarisation. The polarisation variations induced in the probe pulse are linearly proportional to the mid-infrared field strength. An ellipsometry measurement based on a quarter-waveplate, Wollaston prism and a balanced detector is used to measure the polarisation changes with exceptional sensitivities. The EOS technique provides unique resolutions to measure absorption peaks induced by the medium where the mid-infrared beam is propagated. Thus, the method can be used to recognise unknown elements present in the medium.

Appendix B

Filamentation driven by 3.2 μm ultrafast pulses

Before the soliton compression in the ARR-PCF was developed, the 3.2 μm ultrafast pulses were compressed via filamentation. As was shown by Michaël Hemmer and co-workers in 2013 [113], microjoule level 3.1 μm pulses could be compressed below 3-cycles via filamentation in a YAG crystal. They demonstrated 3 μJ pulse self-compression from 70 fs down to 32 fs (factor $\sim$ 2.2). After the 3.2 μm OPCPA was upgraded (see section 3.1), our goal became to compress efficiently the 118 μJ energies delivered from the OPCPA to achieve the highest peak powers.

As described in equation 2.3.14, the self-focusing effect will be triggered once the critical power is overcome. The self-focusing effects become stronger at higher pulse energies, and higher losses from plasma generation are induced. Moreover,

TABLE B.1: Optical parameters of BaF_2, Sapphire and YAG.

	n_0	n_2 $(10^{-20}\ m^2/W)$	GDD (fs^2/mm)	Bandgap (eV)	Critical power* (MW)
BaF_2	1.46	1.99	-57	11.1	49.62
Sapphire	1.71	4.23	-696	9.9	16.66
YAG	1.78	8.3	-408	7	9.76

* Critical power for self-focusing calculated using equation 2.3.14 for our 3.2 μm pulses.

TABLE B.2: 3.2 μm pulse parameters used for the filamentation process in BaF_2, Sapphire and YAG.

	Maximum energy (μJ)	Peak power (MW)	Beam waist (μm)	Rayleigh length (mm)	Crystal Length (MW)	Max. Peak intensity (TW/cm^2)	B integral
BaF_2	6	60	64	4	15	0.9	1.4
Sapphire	30	300	44	2	10	9.9	16
YAG	10	100	83	6.8	3	3.3	37

* Bintegral calculated from equation 2.3.5. The estimated Rayleigh length is used for L_i.

powerful self-focusing effects combined with weak plasma generations can promote possible damages in the medium. Therefore, we studied various nonlinear materials with different optical properties to find the most suitable medium to generate the self-compression 3.2 μm pulses at higher pulse energies than investigated so far. In Table B.1 are shown the optical properties of BaF_2, YAG and Sapphire crystals used for the filamentation experiments. While YAG has the highest n_2 value and lowest critical power, even in BaF_2 with a relatively low n_2 value, the critical power for self-focusing is overcome above 5 μJ.

Each material requires the optimisation of the focal size and crystal length to achieve the optimum compression of the 3.2 μm pulses. Moreover, the maximum energy allowed by each nonlinear material to generate a clean filamentation process is different. In Table B.2 are shown the 3.2 μm pulse parameters optimised for each medium. In BaF_2, the peak power value used is close to its critical power value and the B integral just slightly above 1. On the other hand, in YAG and Sapphire, the peak powers used are an order of magnitude higher than their critical powers, and higher B integrals are used. Therefore, BaF_2 provides higher control on the filamentation and compression process than YAG and Sapphire. Using a 15 mm long BaF_2 pumped by 6 μJ mid-infrared pulse energies compression down to 40 fs was achieved in this medium (factor $\sim$ 2.5). While the compression factor was relatively high, we found that the BaF_2 damage threshold was around an order of magnitude lower than in Sapphire and YAG, restricting the mid-infrared pulse self-compression to energies below 6 μJ.

YAG with higher damage thresholds enabled pumping the nonlinear medium with higher pulse energies. Unfortunately, multi-filamentation processes were triggered

due to the high B integral values achieved already at 10 μJ pulse energies. The multi-filamentation process produces unstable beam parameters and enhanced power fluctuations. Moreover, the high positive nonlinear dispersion introduced (due to the high B integral value) was not compensated with the negative chirp introduced by the medium. Thus, the mid-infrared pulse stretching up to 160 fs was measured.

Sapphire showed the highest damage threshold values enabling the filamentation stage to pump up to 10 TW/cm^2. Moreover, more conservative B integrals avoided the generation of multi-filamentation processes. Figure B.1 shows the schematic design for the generation of self-compressed mid-infrared pulses via filamentation in Sapphire. The pulse energy of the high-power 3.22 μm beam out from the OPCPA (see Figure 3.1) is controlled using a half-waveplate and the wire-grid high extension-ratio polariser. Due to the high dispersion introduced by the sapphire rod (see Table B.1), the 3.22 μm pulses were pre-positively chirped using a 6 mm thick AR coated Silicon window. While in principle, we could post-compensate the pulses inserting the 6 mm AR coated after the filamentation process, it is preferable to pre-compensate and reduce the effect of the huge TOD introduced by the Silicon window to the 3.22 μm pulses. The mid-infrared beam is focused in the 10 mm sapphire crystal using an uncoated $f = 75$ mm plano-convex fused silica lens and back collimated using an Aluminium coated curved mirror with $f = 75$ mm. The metallic curved mirror is used to collimate the broadened pulses avoiding possible achromatic aberrations induced by lenses.

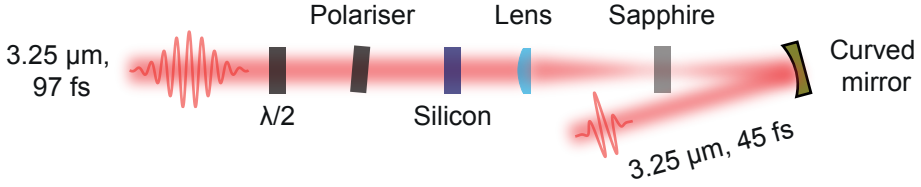

FIGURE B.1: Conceptual design of the self-compression set-up via the filamentation process. The energy of the mid-infrared pulses is controlled using a half-waveplate and a mid-infrared polariser. A 6 mm long AR coated Silicon window is used to pre-compensated the Sapphire chirp. The 3.2 μm pulses are focused in the 10 mm sapphire crystal using an uncoated $f = 75$ mm plano-convex fused silica lens and back collimated using an Aluminium coated curved mirror with $f = 75$ mm.

Figure B.2 shows the compressed pulse duration dependency on the input driving pulse energies in the 10 mm thick Sapphire rod. While the pulse duration decreases with higher pump energies, the efficiency of the process drops significantly at higher intensities. For instance, at 152 μJ input energies, the achieved efficiency is around

40%. When the input energy is double (302 μJ), the output efficiency is half (22%). Thus, while input peak powers of 300 MW were used for the filamentation process, around 135-150 MW peak powers were measured at the output.

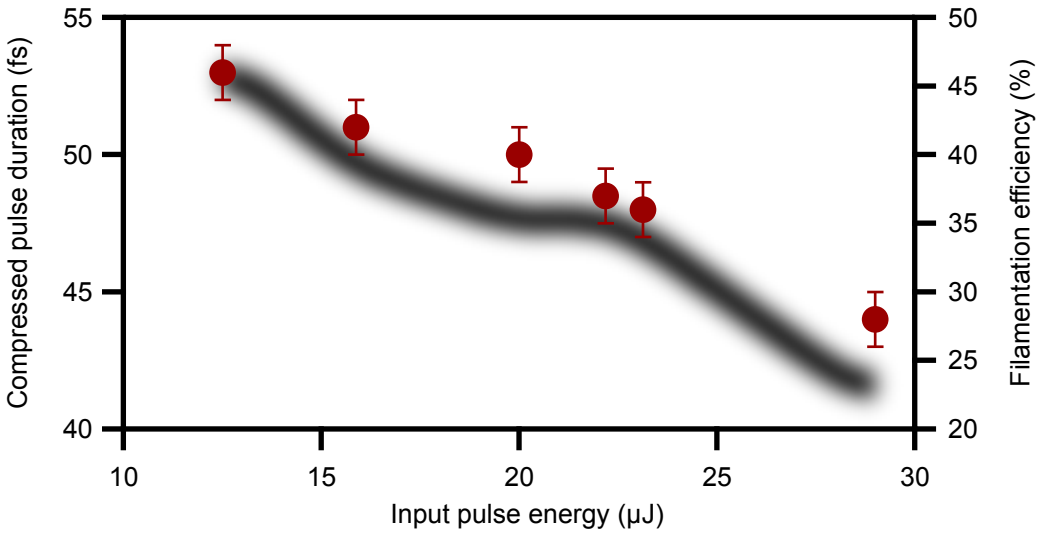

FIGURE B.2: Input pulse energy dependency of the compressed 3.2 μm pulses in the filamentation process (red dots), and transmission efficiency through the Sapphire rod (black line).

Thanks to the simplicity of this compression scheme, it can be interesting to exploit in experiments that require few microjoules and close to 3-cycle durations. On the other hand, compression techniques with higher efficiencies are required for strong-field processes, which demand higher peak powers.

Nowadays, more intricate bulk compression schemes are developed to compress high energy pulses using multi-pass geometries. In those schemes, the filamentation process is avoided, and higher efficiencies are maintained by compressing the pulses exploiting pure SPM [166–168].

Appendix C

HHS in ZnSe driven by mid-infrared ultrafast pulses

During the PhD, HHS was studied driven by 3.2 μm pulses and 7 μm pulses. Two different spectrometers are required to measure the harmonics generated from 7 μm pulses. Third, five and seventh harmonic can be measured using an extended InGaAs spectrometer (900 nm to 2500 nm). Moreover, the harmonics generated from 7^{th} to 35^{th} silicon-based spectrometers can be used. The low dynamic range, sensitivity, and wavelength resolution of the standard extended InGaAs spectrometers limit the measurement of the harmonics generated in the near-infrared regime. Therefore, HHS produced driven by 7 μm pulses can be attractive when harmonics above 7th are required to be studied. Unfortunately, the low repetition rate of our 7 μm OPCPA and the unfavourable wavelength scaling behaviour of the HHS process demands thick mediums or high peak intensities. Moreover, transmission HHS experiments in thick materials or driven at high peak intensities can obscure the interpretation of the measurement. Thus, while the first harmonic generation experiments in ZnSe were conducted driven by 7 μm pulses, more in-depth investigations were carried out driven by 3.2 μm high-repetition-rate pulses, in thin samples and driven with < 100 GW/cm^2 intensities.

Figure C.1 shows the comparison between the harmonics driven by 7 μm and 3.2 μm pulses. While a broad harmonic spectrum was measured driven the process with 7 μm pulses in a 3 mm thick polycrystalline ZnSe piece (see Figure 4.11), only the third and fourth harmonics could be measured using a six times thinner sample. For instance, the fourth harmonic intensity is ten times lower than the harmonic intensity achieved driven by 3.2 μm pulses.

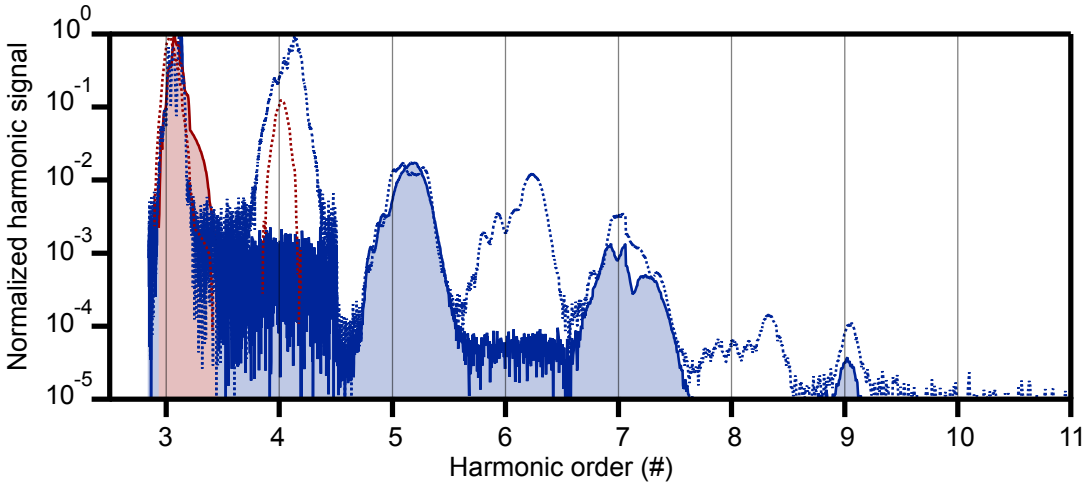

FIGURE C.1: Generated harmonics through a 400 μm thin ZnSe sample cut in 100 plane driven by horizontally polarised 7 μm (red curves) and 3.2 μm (blue curves) pulses. The shadowed curves correspond to the HHS process generated at normal incident angle ($\theta = 0°$). The dotted lines correspond to the harmonics generated with the ZnSe sample at $\theta = 25°$.

TABLE C.1: Mid-infrared pulse parameters used for the HHS experiments.

Centre wavelength (nm)	Pulse energy (μJ)	Pulse duration (fs)	Beam waist (μm)	Peak intensity (GW/cm^2)
3195	1.875	97	115	93
7100	25	188	150	375

Table C.1 shows the pulse parameters used for the HHS process driven by 3.2 μm and 7 μm pulses. Even using much higher 7 μm peak intensities, the efficiency in generating the highest harmonics drops significantly. The highest harmonics are expected to be generated from the inter-band process, which is less efficient at a longer driving wavelength. In contrast, the third harmonic is produced from the intra-band transitions, thus expecting weaker dependencies on the driving frequency. Therefore, the 400 μm thin ZnSe sample could still be used to characterise the 7 μm pulses via THG-FROG measurements.

Figure C.2 shows the layout of the set-up used for the HHS investigations driven by 3.2 μm pulses. The power of the 3.2 μm beam is controlled by a MgF_2 half-waveplate implemented in a motorised stage and a wire-grid polariser set to transmit horizontally polarised light. Afterwards, the mid-infrared beam is focused

using an $f = 75$ mm gold-coated off-axis parabolic mirror and generated harmonics free-space coupled in the Si-based spectrometer using an $f = 75$ mm uncoated fused silica plano-convex lens. The ZnSe sample is implemented in a rotational motorised stage for the angular-dependency measurements.

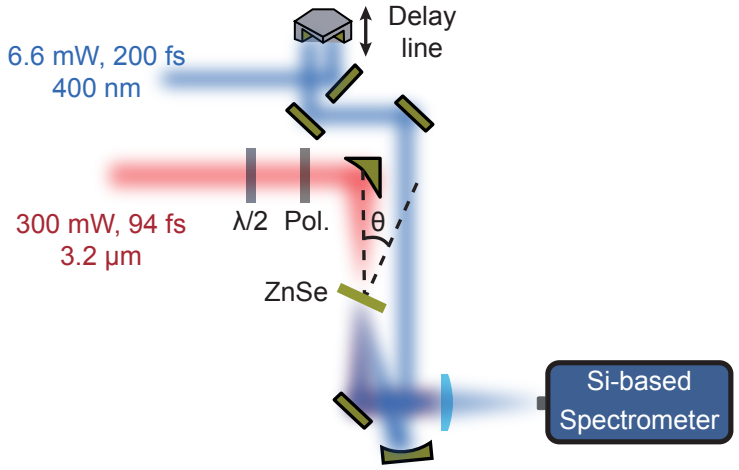

FIGURE C.2: Conceptual design for the investigation of the HHS process. Vertically polarised 3.2 μm pulses go through an attenuation stage based on a half-wave plate the wire-grid polariser. The polariser is set to transmit horizontally polarised light. The mid-infrared beam is focused in the ZnSe sample using an $f = 75$ mm gold-coated off-axis parabolic mirror and back imaged in the Si-based spectrometer using an $f = 75$ mm fused silica plano-convex lens. For the pump-probe experiments, a 400 nm pulse is focused on the back surface of the ZnSe sample using an $f = 100$ mm aluminium-coated curved mirror. The temporal delay between both pulses is varied using a corner cube built in a translation stage.

The bandgap of the ZnSe is around 459 nm. To excite electrons from the valance band to the conduction band, a 400 nm pump line was developed. From the 3.2 μm pulses out of the OPCPA, a 1 mm thick AR coated AGS nonlinear crystal (cut at $\theta = 34°$) was employed to double the frequency of the 3.2 μm pulses. After reflecting the generated 1.6 μm pulses in a dichroic, the 3.2 μm pulses were transmitted towards the HHS set-up. The 1.6 μm pulses were again doubled in a 2 mm thick AR coated BBO nonlinear crystal (cut at $\theta = 21°$), and once more in a second 1 mm thick AR coated BBO (cut at $\theta = 29.2°$) for the generation of the 400 nm pulses with 15 mW and 200 fs pulse duration. Peak intensities at the focus of 1.3 GW/cm^2 were achieved by focusing the 400 nm pulses using an $f = 100$ mm aluminium coated curved mirror. An aluminium-coated corner cube was implemented on top of a motorised translation stage to ensure stable beam pointing during the pump-probe experiment. The developed HHS set-up enables 3-dimensional HHS study, including power-, angular- and temporal-dependencies.

Angular-dependency of the harmonics

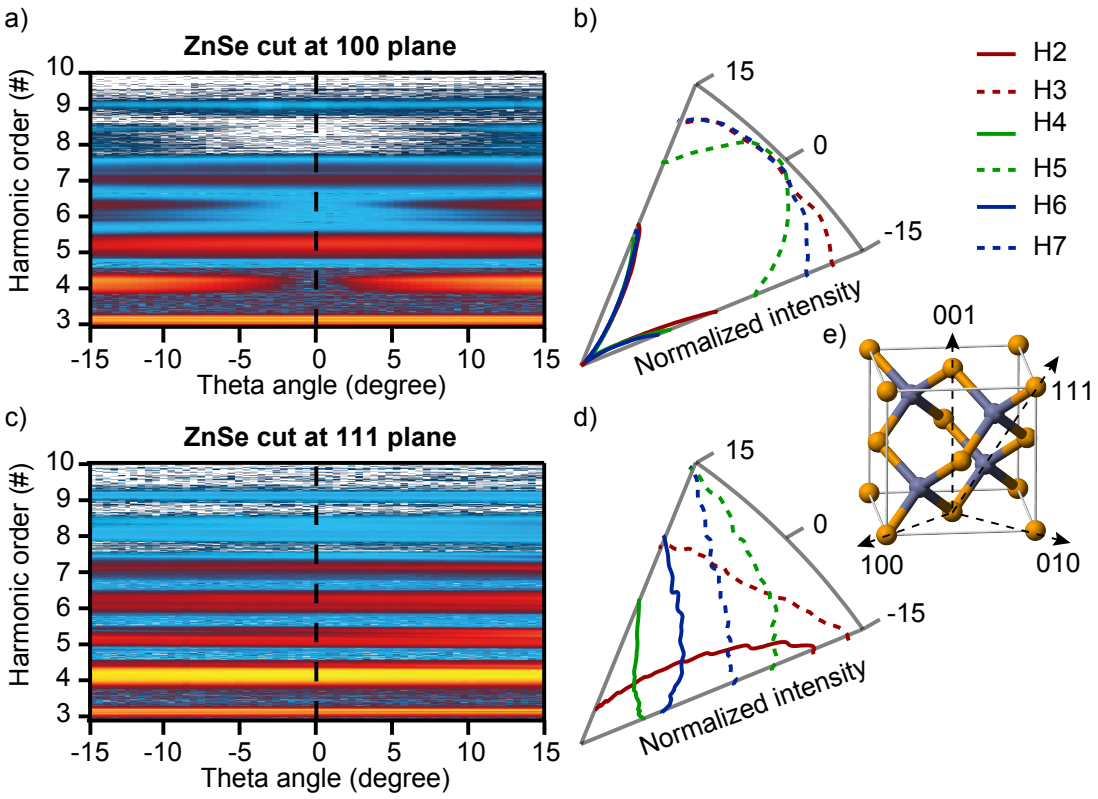

FIGURE C.3: Angular-dependency study of the HHS process in a 400 μm thin ZnSe sample. a) Spectral evolution of the generated harmonics and b) polar representation of the normalised harmonic intensities from a ZnSe cut at 100 plane. c) Spectral evolution of the generated harmonics and d) polar representation of the normalised harmonic intensities from a ZnSe cut at 111 plane. Dashed lines represent odd harmonics: 3^{rd} (dashed red), 5^{th} (dashed green) and 7^{th} (dashed blue). With solid lines are shown even harmonics: 2^{nd} (solid red), 4^{th} (solid green) and 6^{th} (solid blue). e) ZnSe crystallographic structure and main directions.

In Figure C.3 is shown the HHS angular-dependency studied in 400 μm thin 100 and 111-cut ZnSe monocrystalline samples. In the 100-cut ZnSe sample, only odd harmonics are produced at $\theta = 0°$ due to the high-symmetry introduced by the cubic structure (see Figure C.3 (e)). When the crystal is rotated, its centrosymmetric nature is hacked, and even harmonics are produced. As shown in Figure C.3 (b), the even harmonic signal increases at higher theta angles, while the odd harmonic signal decreases. Harmonics generated in the 111-cut ZnSe sample, both even and odd harmonics generation is demonstrated for all the measured theta angles. As shown in Figure C.3 (d), the second and third harmonic intensity decreases from $-15°$ to $15°$ while the intensity of the higher harmonics (both even and odd) increases.

Power-dependency of the harmonics

The harmonics generated from the intra-band transitions depend on the medium's lattice distance, which can be estimated fitting equation 2.4.8 to the measured pump-field dependent harmonic intensities. Figure C.4 shows HHS's power-dependency measurement carried out at normal incidence, in the 400 μm thin 100-cut ZnSe.

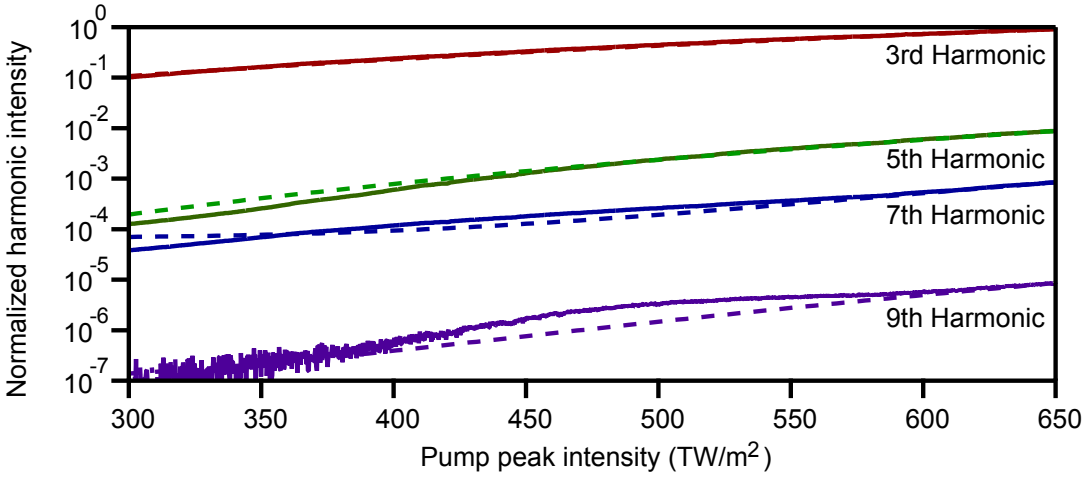

FIGURE C.4: Pump peak intensity dependency on the 3^{rd} (red), 5^{th} (green), 7^{th} (blue) and 9^{th} (purple) harmonic intensity. In dashed lines are shown with the corresponding colours the fittings based on equation 2.4.8.

ZnSe has a zinc blende type crystallographic structure with a lattice constant of $a = 566.8\ pm$. Table C.2 shows the achieved Bessel orders and lattice parameters retrieved from fitting the power-dependency curves shown in Figure C.4. The third and five harmonics are generated below the bandgap energy. Thus, those harmonics are expected to be generated from intra-band transitions described in section 2.4.1. The seventh harmonic is generated across the ZnSe bandgap energy. As shown in Table C.2, the Bessel orders required for fitting the measured 3^{rd}, 5^{th} and 7^{th} curves match with the harmonic orders.

On the other hand, the Bessel order retrieved from the ninth harmonic generated above bandgap, and thus, in the output surface of the ZnSe sample, does not match with the harmonic order. The inter-band transitions are not described by equation 2.4.8 used for the fitting. Thus, assuming that the ninth harmonic is generated from inter-band transitions, the mismatch between the fitted Bessel order and harmonic order could be explained.

TABLE C.2: Bessel function fitting coefficients extracted from the power dependency measurements shown in Figure C.4.

Harmonic (#)	Centre wavelength (nm)	Bessel (#)	Lattice Parameter (pm)
3^{rd}	1065	2.97	618
5^{th}	639	4.99	584
Bandgap at 459 nm			
7^{th}	456	6.94	663
9^{th}	355	6.99	589

Pump-probe harmonic decay measurements

Electron-electron, electron-phonon and phonon-phonon scattering processes can be studied by measuring the generated harmonic intensities in a pump-probe scheme. The pump field pre-excites the electrons from the valance band to the conduction band, and the probe pulse generates the harmonics. A 400 nm field with 200 fs duration is used to excite electrons across de bandgap, and the 3200 nm 97 fs pulses generate the harmonics through the 111-cut ZnSe sample. For this experiment, 111-oriented ZnSe is used to study the pump dependency in even and odd harmonics.

Figure C.5 shows the harmonic intensity variations measured when a pump field pre-excites the electrons from the valance band to the conduction band. Interestingly, five and sixth harmonics are enhanced when electrons are pumped to the conduction band, while the intensity of the 7^{th}, 9^{th} and 11^{th} decreases. Moreover, while the third harmonic variation is almost imperceptible, a slight reduction in the third harmonic intensity is measured.

The harmonic decays are related to the medium's relaxation times. The rising edge should be a convolution between the pump Gaussian pulses, probe Gaussian pulse and the absorption (usually described by Lorentzian shapes). Moreover, the long temporal decay can be expressed with an exponential. The Gaussian traces' convolution is defined in equation 4.1.1 and maintains the Gaussian profile. The

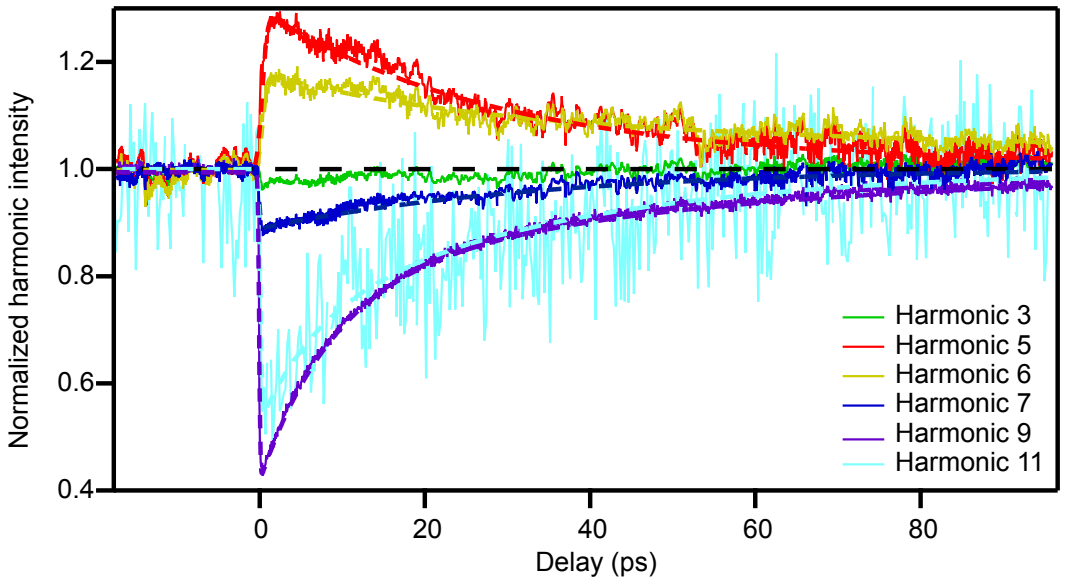

FIGURE C.5: Pump-probe measurement and the retrieved harmonic decay curves from the 111-cut ZnSe sample. Normalised integrated intensities from 3^{rd} (solid green), 5^{th} (solid red), 6^{th} (solid yellow), 7^{th} (solid blue), 9^{th} (solid purple) and 11^{th} (solid light-blue) harmonics. With dashed lines are shown the fitting curves achieved from equation C.2.

convolution of the Gaussian shape with a Lorentzian function is the Voigt profile. Thus, the function required to fit the measured harmonic curves would be the convolution between Voigt and exponential decay. For this purpose, a numerically described fitting function is required, interfering with the fitting algorithm's convergence. Therefore, we have neglected the absorption Lorentzian profile and proceed to fit the curves with the convolution of the Gaussian profile with the exponential decay:

$$f(t) = \int_0^\infty e^{-\left(\frac{t'}{2\sigma}\right)^2} e^{-(t'-t)/\tau} \mathrm{d}t' = \sigma\sqrt{\pi} e^{\frac{\sigma^2-\tau t}{\tau^2}} \left[1 + Erf\left(\frac{-2\sigma^2+\tau t}{2\sigma\tau}\right)\right] \quad \text{(C.1)}$$

where τ is the scattering time of the decaying channel. The equation C.1 is extended to retrieve two different decay times from the curves shown in Figure C.5:

$$I(t) = 1 + \sum_{i=1}^{2} C_i e^{\frac{\sigma^2-\tau_i t}{\tau_i^2}} \left[1 + Erf\left(\frac{-2\sigma^2+\tau_i t}{2\sigma\tau_i}\right)\right] \quad \text{(C.2)}$$

where C_i is the weight of each scattering process.

While decay processes above 500 fs are retrieved with our scheme, typical electron-electron scattering times with few femtosecond time scales are is unaffordable to detect due to the long pump and probe pulse durations. Table C.3 shows the decay times retrieved from the fitting equation C.1 and C.2 to the curves shown in Figure C.5.

TABLE C.3: Retrieved decay times from pump-probe HHS measurement. The second column shows the decay rate retrieved from a single decay function (equation C.1). Third and fourth columns show the extracted decay rates assuming two different decay rates contributing to the harmonic intensity variations (equation C.2).

Harmonic (#)	Decay time τ (ps)	Decay time τ_1 (ps)	Decay time τ_2 (ps)
3^{rd}	18.34 ± 1.15	20.6 ± 1.3	-
5^{th}	33.96 ± 0.33	33.6 ± 0.3	0.65 ± 0.06
6^{th}	72.38 ± 1.24	72.3 ± 1.3	0.51 ± 0.19
7^{th}	4.05 ± 1.66	-	3.4 ± 1.6
9^{th}	23.05 ± 0.15	28.9 ± 0.2	2.93 ± 0.20
11^{th}	24.54 ± 1.64	24.2 ± 1.1	2.09 ± 1.76

The second column of Table C.3 shows the retrieved phonon-phonon scattering times extracted from a single decay term. The second decay term is required to retrieve electron-phonon relaxation times (or optical phonons) in the few picosecond durations [169–171].

Phonon-phonon and electron-phonon scattering times vary with the bands where electron transitions are induced [172]. Thus, the retrieved scattering times from different harmonics correspond to various band transitions. Electron-phonon relaxation times from (0.51 ± 0.19) ps [173] to (3.4 ± 1.6) ps [169] depending on the analysed harmonics are achieved. Only a single relaxation channel is extracted from the third and seventh harmonic due to the low harmonic signal variations measured in the pump-probe experiment.

In conclusion, while ab-initio calculations can be carried out to estimate those parameters in semiconductors such as ZnSe [172], medium characterisation based on HHS measurements, shown here, can help to analyse more complex materials such as YBCO.

List of Figures

List of Tables

Bibliography

[1] Maiman, T. Stimulated Optical Radiation in Ruby. *Essentials of Lasers* **87**, 134–136 (1960).

[2] Franken, P. A., Hill, A. E., Peters, C. W. & Weinreich, G. Generation of optical harmonics. *Physical Review Letters* **7**, 118–119 (1961).

[3] Laenen, R., Graener, H. & Laubereau, A. Broadly tunable femtosecond pulses generated by optical parametric oscillation. *Optics Letters* **15**, 971 (1990).

[4] Dubietis, A., Jonušauskas, G. & Piskarskas, A. Powerful femtosecond pulse generation by chirped and stretched pulse parametric amplification in BBO crystal. *Optics Communications* **88**, 437–440 (1991).

[5] Lewenstein, M., Balcou, P., Ivanov, M. Y., L'Huillier, A. & Corkum, P. B. Theory of high-harmonic generation by low-frequency laser fields. *Journal of Chemical Information and Modeling* **53**, 1689–1699 (1994).

[6] Corkum, P. B. Plasma perspective on strong field multiphoton ionization. *Physical Review Letters* **71**, 1994–1997 (1993).

[7] Popmintchev, T., Chen, M. C., Arpin, P., Murnane, M. M. & Kapteyn, H. C. The attosecond nonlinear optics of bright coherent X-ray generation. *Nature Photonics* **4**, 822–832 (2010).

[8] Teichmann, S. M., Silva, F., Cousin, S. L., Hemmer, M. & Biegert, J. 0.5-keV Soft X-ray attosecond continua. *Nature Communications* **7**, 1–6 (2016).

[9] Silva, F., Teichmann, S. M., Cousin, S. L., Hemmer, M. & Biegert, J. Spatiotemporal isolation of attosecond soft X-ray pulses in the water window. *Nature Communications* **6**, 1–6 (2015).

[10] Gaumnitz, T. et al. Streaking of 43-attosecond soft-X-ray pulses generated by a passively CEP-stable mid-infrared driver. *Optics Express* **25**, 27506 (2017).

[11] Franklin, R. E. & Gosling, R. G. The Structure of Sodium Thymonuclete Fibres . I . The Influence of Water Content. *Acta Cryst.* **6**, 673 (1953).

[12] Davis, T. J., Gao, D., Gureyev, T. E., Stevenson, A. W. & Wilkins, S. W. Phase-contrast imaging of weakly absorbing materials using hard X-rays (1995).

[13] Wilkins, S. W., Gureyev, T., Gao, D., Pogany, A. & A.W.Stevenson. Phase-contrast imaging using polychromatic hard X-rays. *Nature* **384**, 335 (1996).

[14] Buades, B. et al. Dispersive soft x-ray absorption fine-structure spectroscopy in graphite with an attosecond pulse. *Optica* **5**, 502 (2018).

[15] Buades, B. et al. Attosecond-resolved petahertz carrier motion in semi-metallic TiS_2. *arXiv* 23–26 (2018).

[16] Porer, M. et al. Non-thermal separation of electronic and structural orders in a persisting charge density wave. *Nature Materials* **13**, 857–861 (2014).

[17] Pires, H., Baudisch, M., Sanchez, D., Hemmer, M. & Biegert, J. Ultrashort pulse generation in the mid-IR. *Progress in Quantum Electronics* **43**, 1–30 (2015).

[18] Diddams, S. A., Hollberg, L. & Mbele, V. Molecular fingerprinting with the resolved modes of a femtosecond laser frequency comb. *Nature* **445**, 627–630 (2007).

[19] Abbas, M. A. et al. Time-resolved mid-infrared dual-comb spectroscopy. *Scientific Reports* **9**, 1–9 (2019).

[20] Pessot, M., Maine, P. & Mourou, G. 1000 times expansion/compression of optical pulses for chirped pulse amplification. *Optics Communications* **62**, 419–421 (1987).

[21] Kiss, Z. J. & Duncan, R. C. Cross-pumped Cr^{3+}-Nd^{3+}:YAG laser system. *Applied Physics Letters* **5**, 200–202 (1964).

[22] Andriukaitis, G. et al. 90 GW peak power few-cycle mid-infrared pulses from an optical parametric amplifier. *Optics Letters* **36**, 2755 (2011).

[23] Baudisch, M. et al. Sub-4-optical-cycle, 340 MW peak power, high stability mid-IR source at 160 kHz. *Journal of Optics (United Kingdom)* **17**, 94002 (2015).

[24] Moulton, P. F. Spectroscopic and laser characteristics of $Ti:Al_2O_3$. *Journal of the Optical Society of America B* **3**, 125 (1986).

[25] Bartels, R. A. et al. Generation of spatially coherent light at extreme ultraviolet wavelengths. *Science* **297**, 376–378 (2002).

[26] Chalus, O., Bates, P. K. & Biegert, J. Design and simulation of few-cycle optical parametric chirped pulse amplification at mid-IR wavelengths. *Optics Express* **16**, 673–677 (2008).

[27] Schulz, M. et al. Yb:YAG Innoslab amplifier: efficient high repetition rate subpicosecond pumping system for optical parametric chirped pulse amplification. *Optics Letters* **36**, 2456 (2011).

[28] Grafenstein, L. V., Bock, M., Ueberschaer, D., Griebner, U. & Elsaesser, T. Ho:YLF chirped pulse amplification at kilohertz repetition rates – 43 ps pulses at 2 μm with GW peak power. *Optics Letters* **41**, 4668 (2016).

[29] Elu, U. et al. Table-top high-energy 7 μm OPCPA and 260 mJ Ho:YLF pump laser. *Optics Letters* **44**, 3194 (2019).

[30] Kanai, T. et al. Parametric amplification of 100 fs mid-infrared pulses in $ZnGeP_2$ driven by a Ho:YAG chirped-pulse amplifier. *Optics Letters* **42**, 683 (2017).

[31] Grafenstein, L. V. et al. 5 μm few-cycle pulses with multi-gigawatt peak power at a 1 kHz repetition rate. *Optics Letters* **42**, 3796–3799 (2017).

[32] Cousin, S. L. et al. High-flux table-top soft x-ray source driven by sub-2-cycle, CEP stable, 185-μm 1-kHz pulses for carbon K-edge spectroscopy. *Optics Letters* **39**, 5383 (2014).

[33] Partin, D. L. Lead salt quantum well diode lasers. *Superlattices and Microstructures* **1**, 131–135 (1985).

[34] Tolstik, N., Sorokin, E. & Sorokina, I. T. Graphene mode-locked Cr:ZnS laser with 41 fs pulse duration. *Optics Express* **22**, 5564 (2014).

[35] Vasilyev, S., Moskalev, I., Mirov, M., Mirov, S. & Gapontsev, V. Three optical cycle mid-IR Kerr-lens mode-locked polycrystalline Cr^{2+}:ZnS laser. *Optics Letters* **40**, 5054 (2015).

[36] Moskalev, I. et al. 140 W Cr:ZnSe laser system. *Optics Express* **24**, 713–720 (2016).

[37] Erny, C., Moutzouris, K. & Biegert, J. Mid-infrared difference-frequency generation of ultrashort pulses tunable between 3.2 and 4.8 μm from a compact fiber source. *Optics Letters* **32**, 1138–1140 (2007).

[38] Sánchez, D. et al. Broadband mid-IR frequency comb with $CdSiP_2$ and $AgGaS_2$ from an Er,Tm:Ho fiber laser. *Optics Letters* **39**, 6883 (2014).

[39] Hoogland, H. et al. All-PM coherent 205 µm Thulium/Holmium fiber frequency comb source at 100 MHz with up to 0.5 W average power and pulse duration down to 135 fs. *Optics Express* **21**, 31390 (2013).

[40] Kowligy, A. S. et al. Infrared electric field sampled frequency comb spectroscopy. *Science Advances* **5**, 36–38 (2019).

[41] Pupeza, I. et al. High-power sub-two-cycle mid-infrared pulses at 100 MHz repetition rate. *Nature Photonics* **9**, 721–724 (2015).

[42] Petrov, V. Frequency down-conversion of solid-state laser sources to the mid-infrared spectral range using non-oxide nonlinear crystals. *Progress in Quantum Electronics* **42**, 1–106 (2015).

[43] Schunemann, P. G. New nonlinear crystals for the mid-infrared. In *Optics InfoBase Conference Papers*, vol. Nonlinear (2017).

[44] Wood, R. M., Sharma, S. K. & Waite, P. Laser damage in optical materials at 1.06 μm. *GEC journal of science & technology* **48**, 141–151 (1982).

[45] Hildenbrand, A. et al. Laser damage of the nonlinear crystals $CdSiP_2$ and $ZnGeP_2$ studied with nanosecond pulses at 1064 and 2090 nm. *Optical Engineering* **53**, 122511 (2014).

[46] Hansson, G., Karlsson, H., Wang, S. & Laurell, F. Transmission measurements in KTP and isomorphic compounds. *Applied Optics* **39**, 5058 (2000).

[47] Ishizuki, H. & Taira, T. Mg-doped congruent $LiTaO_3$ crystal for large-aperture quasi-phase matching device. *Optics InfoBase Conference Papers* **16**, 2531–2534 (2008).

[48] Manjooran, S., Zhao, H., Lima, I. T. & Major, A. Phase-matching properties of PPKTP, MgO:PPSLT and MgO:PPcLN for ultrafast optical parametric oscillation in the visible and near-infrared ranges with green pump. *Laser Physics* **22**, 1325–1330 (2012).

[49] Baudisch, M., Hemmer, M., Pires, H. & Biegert, J. Performance of MgO:PPLN, KTA, and $KNbO_3$ for mid-wave infrared broadband parametric amplification at high average power. *Optics Letters* **39**, 5802 (2014).

[50] Furukawa, Y. et al. Green-induced infrared absorption in MgO doped $LiNbO_3$. *Applied Physics Letters* **78**, 1970–1972 (2001).

[51] Hirohashi, J., Pasiskevicius, V., Wang, S. & Laurell, F. Picosecond blue-light-induced infrared absorption in single-domain and periodically poled ferroelectrics. *Journal of Applied Physics* **101** (2007).

[52] Freytag, F. et al. Picosecond near-to-mid-infrared absorption of pulse-injected small polarons in magnesium doped lithium niobate. *Optical Materials Express* **8**, 1505 (2018).

[53] Okorogu, A. O. et al. Tunable middle infrared downconversion in GaSe and $AgGaS_2$. *Optics Communications* **155**, 307–312 (1998).

[54] Zhang, G. et al. Growth and polarized Raman spectroscopy investigations of single crystal $CdSiP_2$: Experimental measurements and ab initio calculations. *Journal of Crystal Growth* **473**, 28–33 (2017).

[55] Ni, Y. et al. Growth and characterization of mid-far infrared optical material CdSe crystal. *Optical Materials Express* **8**, 1796 (2018).

[56] Kanai, T., Lee, Y., Seo, M. & Kim, D. E. Supercontinuum-seeded, carrier-envelope phase-stable, 45-W, 38-μm, 6-cycle, KTA optical parametric amplifier driven by a 14-ps Yb:YAG thin-disk amplifier for nonperturbative spectroscopy in solids. *Journal of the Optical Society of America B* **36**, 2407 (2019).

[57] Thiré, N. et al. Highly stable , 15 W , few-cycle , 65 mrad CEP- noise mid-IR OPCPA for statistical physics. *Optics Express* **26**, 26907–26915 (2018).

[58] Elu, U. et al. High average power and single-cycle pulses from a mid-IR optical parametric chirped pulse amplifier. *Optica* **4** (2017).

[59] Boyd, R. W. *Nonlinear Optics* (Academic Press, 1992).

[60] Jean-Claude Diels and Wolfgang Rudolph. *Ultrashort Laser Pulse Phenomena* (Academic Press, 2006).

[61] Kolesik, M., Moloney, J. V. & Mlejnek, M. Unidirectional Optical Pulse Propagation Equation. *Physical Review Letters* **89**, 1–4 (2002).

[62] Jones, D. J. et al. Carrier-envelope phase stabilization of femtosecond modelocked lasers and direct optical frequency synthesis. *Science* **288**, 635–639 (2000).

[63] Hongjun, L. et al. Investigation of spectral bandwidth of optical parametric amplification. *Applied Physics B: Lasers and Optics* **79**, 569–576 (2004).

[64] Petrov, V. & Noack, F. Mid-infrared femtosecond optical parametric amplification in potassium niobate. *Optics Letters* **21**, 1576 (1996).

[65] Umemura, N., Yoshida, K. & Kato, K. Phase-matching properties of $KNbO_3$ in the mid-infrared. *Applied Optics* **38**, 991 (1999).

[66] Manley, J. M. & Rowe, H. E. Some General Properties of Nonlinear Elements-Part I. General Energy Relations. *Proceedings of the IRE* **44**, 904–913 (1956).

[67] Timmers, H. et al. Molecular fingerprinting with bright , broadband infrared frequency combs. *Optica* **5** (2018).

[68] Elu, U. et al. Seven-octave high-brightness and carrier-envelope-phase-stable light source. *Nature Photonics* **15**, 277–280 (2021).

[69] Nishikawa, T., Uesugi, N. & Yumoto, J. Parametric superfluorescence in $KTiOPO_4$ crystals pumped by 1 ps pulses. *Applied Physics Letters* **58**, 1943–1945 (1991).

[70] Chalus, O., Schunemann, P. G., Zawilski, K. T., Biegert, J. & Ebrahim-Zadeh, M. Optical parametric generation in $CdSiP_2$. *Optics Letters* **35**, 4142 (2010).

[71] Tavella, F., Marcinkevičius, A. & Krausz, F. Investigation of the superfluorescence and signal amplification in an ultrabroadband multiterawatt optical parametric chirped pulse amplifier system. *New Journal of Physics* **8** (2006).

[72] Arisholm, G. Second-Order Nonlinear Interactions in Birefringent Media. *Journal of the Optical Society of America B* **14**, 2543–2549 (2007).

[73] Wu, Q. & Zhang, X. C. Free-space electro-optic sampling of terahertz beams. *Applied Physics Letters* **67**, 3523 (1995).

[74] Gallot, G. & Grischkowsky, D. Electro-optic detection of terahertz radiation. *Journal of the Optical Society of America B* **16**, 1204 (1999).

[75] Elu, U. et al. Few-cycle mid-infrared pulses from $BaGa_2GeSe_6$. *Optics Letters* **45**, 3813–3815 (2020).

[76] Keiber, S. et al. Electro-optic sampling of near-infrared waveforms. *Nature Photonics* **10**, 159–162 (2016).

[77] Agrawal, G. P. *Nonlinear Fiber Optics*, vol. XXXIII (Academic Press, 2013).

[78] Parent, A., Morin, M. & Lavigne, P. Propagation of super-Gaussian field distributions. *Optical and Quantum Electronics* **24**, 1071–1079 (1992).

[79] Weber, H. Some historical and technical aspects of beam quality. *Optical and Quantum Electronics* **24**, 861–864 (1992).

[80] Siegman, A. E. Analysis of laser beam quality degradation caused by quartic phase aberrations. *Applied Optics* **32**, 5893 (1993).

[81] Perevezentsev, E., Poteomkin, A. & Khazanov, E. Comparison of phase-aberrated laser beam quality criteria. *Applied Optics* **46**, 774–784 (2007).

[82] Jeong, T. M. & Lee, J. Accurate Determination of the Beam Quality Factor of an Aberrated High-power Laser Pulse. *Journal of the Korean Physical Society* **55**, 488–494 (2009).

[83] Fibich, G. & Gaeta, A. L. Critical power for self-focusing in bulk media and in hollow waveguides. *Optics Letters* **25**, 335 (2000).

[84] Schlessinger, L. & Wright, J. A. Inverse-bremsstrahlung absorption rate in an intense laser field. *Physical Review A* **20**, 1934–1945 (1979).

[85] Kolesik, M., Katona, G., Moloney, J. V. & Wright, E. M. Theory and simulation of supercontinuum generation in transparent bulk media. *Applied Physics B: Lasers and Optics* **77**, 185–195 (2003).

[86] Kolesik, M. & Moloney, J. V. Nonlinear optical pulse propagation simulation: From Maxwell's to unidirectional equations. *Physical Review E - Statistical Physics, Plasmas, Fluids, and Related Interdisciplinary Topics* **70**, 11 (2004).

[87] Andreasen, J. & Kolesik, M. Nonlinear propagation of light in structured media: Generalized unidirectional pulse propagation equations. *Physical Review E* **86**, 1–9 (2012).

[88] Okhrimchuk, A. G., Mezentsev, V. K., Schmitz, H., Dubov, M. & Bennion, I. Cascaded nonlinear absorption of femtosecond laser pulses in dielectrics. *Laser Physics* **19**, 1415–1422 (2009).

[89] Darginavičius, J. et al. Ultrabroadband supercontinuum and third-harmonic generation in bulk solids with two optical-cycle carrier-envelope phase-stable pulses at 2 μm. *Optics Express* **21**, 25210 (2013).

[90] Pearl, S., Rotenberg, N. & Van Driel, H. M. Three photon absorption in silicon for 2300-3300 nm. *Applied Physics Letters* **93**, 9–12 (2008).

[91] Arola, E. Theoretical studies on multiphoton absorption of ultrashort laser pulses in sapphire. *IEEE Journal of Quantum Electronics* **50**, 709–720 (2014).

[92] Cassataro, M. et al. Generation of broadband mid-IR and UV light in gas-filled single-ring hollow-core PCF. *Optics Express* **25**, 7637 (2017).

[93] Travers, J. C., Chang, W., Nold, J., Joly, N. Y. & St. J. Russell, P. Ultrafast nonlinear optics in gas-filled hollow-core photonic crystal fibers [Invited]. *Journal of the Optical Society of America B* **28**, A11 (2011).

[94] Tani, F., Travers, J. C. & St.J. Russell, P. Multimode ultrafast nonlinear optics in optical waveguides: numerical modeling and experiments in kagomé photonic-crystal fiber. *Journal of the Optical Society of America B* **31**, 311 (2014).

[95] Zeisberger, M. & Schmidt, M. A. Analytic model for the complex effective index of the leaky modes of tube-type anti-resonant hollow core fibers. *Scientific Reports* **7**, 1–13 (2017).

[96] Vincetti, L. & Rosa, L. A simple analytical model for confinement loss estimation in hollow-core Tube Lattice Fibers. *Optics Express* **27**, 5230 (2019).

[97] Lehmeier, H., Leupacher, W. & Penzkofer, A. Nonresonant third order hyperpolarizability of rare gases and N2 determined by third harmonic generation. *Optics Communications* **56**, 67–72 (1985).

[98] Couairon, A. & Mysyrowicz, A. Femtosecond filamentation in transparent media. *Physics Reports* **441**, 47–189 (2007).

[99] Vampa, G. et al. Plasmon-enhanced high-harmonic generation from silicon. *Nature Physics* **13**, 659–662 (2017).

[100] Baudisch, M. et al. Ultrafast nonlinear optical response of Dirac fermions in graphene. *Nature Communications* **9**, 1–6 (2018).

[101] Bauer, D. & Hansen, K. K. High-Harmonic Generation in Solids with and without Topological Edge States. *Physical Review Letters* **120**, 177401 (2018).

[102] Osika, E. N. et al. Wannier-bloch approach to localization in high-harmonics generation in solids. *Physical Review X* **7**, 1–14 (2017).

[103] Ashcroft, N. W. & Mermin, N. D. *Solid State Physics* (1976).

[104] Wegner, M. *Extreme Nonlinear Optics* (Springer, Berlin, Heidelberg, 2005).

[105] Giannozzi, P. et al. QUANTUM ESPRESSO: a modular and open-source software project for quantum simulations of materials. *Journal of Physics: Condensed Matter* **21**, 395502 (2009).

[106] Luu, T. T. & Wörner, H. J. High-order harmonic generation in solids: A unifying approach. *Physical Review B* **94**, 1–9 (2016).

[107] Chalus, O., Bates, P. K., Smolarski, M. & Biegert, J. Ultrashort mid-IR OPCPA with micro-joule energy at 100 kHz. *Optics InfoBase Conference Papers* **17**, 3330–3332 (2009).

[108] Thai, A., Hemmer, M., Bates, P. K., Chalus, O. & Biegert, J. Sub-250-mrad, passively carrier–envelope-phase-stable mid-infrared OPCPA source at high repetition rate. *Optics Letters* **36**, 3918 (2011).

[109] Hemmer, M., Thai, A. & Baudisch, M. 18-µJ energy, 160-kHz repetition rate, 250-MW peak power mid-IR OPCPA. *Chinese Optics Letters* **11**, 11–13 (2013).

[110] Silva, F. et al. Multi-octave supercontinuum generation from mid-infrared filamentation in a bulk crystal. *Nature Communications* **3** (2012).

[111] Pullen, M. G. et al. Kinematically complete measurements of strong field ionization with mid-IR pulses. *Journal of Physics B: Atomic, Molecular and Optical Physics* **47** (2014).

[112] Wolter, B. et al. Formation of very-low-energy states crossing the ionization threshold of argon atoms in strong mid-infrared fields. *Physical Review A - Atomic, Molecular, and Optical Physics* **90**, 1–8 (2014).

[113] Hemmer, M., Baudisch, M., Thai, A., Couairon, A. & Biegert, J. Self-compression to sub-3-cycle duration of mid-infrared optical pulses in dielectrics. *Optics Express* **21**, 28095 (2013).

[114] Pullen, M. G. et al. Imaging an aligned polyatomic molecule with laser-induced electron diffraction. *Nature Communications* **6**, 1–6 (2015).

[115] Wolter, B. et al. Ultrafast electron diffraction imaging of bond breaking in di-ionized acetylene. *Science* **354**, 308–312 (2016).

[116] Baudisch, M., Wolter, B., Pullen, M., Hemmer, M. & Biegert, J. High power multi-color OPCPA source with simultaneous femtosecond deep-UV to mid-IR outputs. *Optics Letters* **41**, 3583 (2016).

[117] Baudisch, M. et al. 44 μJ, 160 kHz, few-cycle mid-IR OPCPA with chirp reversal. In *2016 Conference on Lasers and Electro-Optics (CLEO), San Jose, CA,* (2016).

[118] Rodwell, M. J., Bloom, D. M. & Weingarten, K. J. Subpicosecond Laser Timing Stabilization. *IEEE Journal of Quantum Electronics* **25**, 817–827 (1989).

[119] Lemoff, B. E. & Barty, C. P. J. Quintic-phase-limited, spatially uniform expansion and recompression of ultrashort optical pulses. *Optics Letters* **18**, 1651 (1993).

[120] Voronin, A. A. & Zheltikov, A. M. Sub-half-cycle field transients from shock-wave-assisted soliton self-compression. *Scientific Reports* **10**, 1–9 (2020).

[121] Benabid, F., Knight, J. C., Antonopoulos, G. & Russell, P. S. J. Stimulated Raman scattering in hydrogen-filled hollow-core photonic crystal fiber. *Science* **298**, 399–402 (2002).

[122] Pryamikov, A. D. et al. Demonstration of a waveguide regime for a silica hollow - core microstructured optical fiber with a negative curvature of the core boundary in the spectral region > 35 μm. *Optics Express* **19**, 1441 (2011).

[123] Kolyadin, A. N. et al. Light transmission in negative curvature hollow core fiber in extremely high material loss region. *Optics Express* **21**, 9514 (2013).

[124] Yu, F., Wadsworth, W. J. & Knight, J. C. Low loss (34 dB/km) silica hollow core fiber for the 3 μm spectral region. *Optics InfoBase Conference Papers* **20**, 11153–11158 (2012).

[125] Uebel, P. et al. Broadband robustly single-mode hollow-core PCF by resonant filtering of higher-order modes. *Optics Letters* **41**, 1961 (2016).

[126] Marcatili, E. A. & Schmeltzer, R. A. Hollow Metallic and Dielectric Waveguides for Long Distance Optical Transmission and Lasers. *Bell System Technical Journal* **43**, 1783–1809 (1964).

[127] Brechet, F., Marcou, J., Pagnoux, D. & Roy, P. Complete Analysis of the Characteristics of Propagation into Photonic Crystal Fibers, by the Finite Element Method. *Optical Fiber Technology* **6**, 181–191 (2000).

[128] Cucinotta, A., Selleri, S., Vincetti, L. & Zoboli, M. Holey fiber analysis through the finite-element method. *IEEE Photonics Technology Letters* **14**, 1530–1532 (2002).

[129] Tomlinson, W. J., Stolen, R. H. & Shank, C. V. Compression of Optical Pulses Chirped By Self-Phase Modulation in Fibers. *Journal of Optical Society of America B* **1**, 139–149 (1984).

[130] Travers, J. C., Chang, W., Nold, J., Joly, N. Y. & St. J. Russell, P. Ultrafast nonlinear optics in gas-filled hollow-core photonic crystal fibers [Invited]. *Journal of the Optical Society of America B* **28**, A11 (2011).

[131] Chen, C.-M. & Kelley, P. L. Nonlinear pulse compression in optical fibers: scaling laws and numerical analysis. *Journal of the Optical Society of America B* **19**, 1961 (2002).

[132] Brée, C., Demircan, A. & Steinmeyer, G. Method for computing the nonlinear refractive index via Keldysh theory. *IEEE Journal of Quantum Electronics* **46**, 433–437 (2010).

[133] Zahedpour, S., Wahlstrand, J. K. & Milchberg, H. M. Measurement of the Nonlinear Refractive Index of Air Constituents at Mid-Infrared Wavelengths. *Optics Letters* **40**, 5794–5797 (2016).

[134] Börzsönyi, Á., Heiner, Z., Kovács, A. P., Kalashnikov, M. P. & Osvay, K. Measurement of pressure dependent nonlinear refractive index of inert gases. *Optics Express* **18**, 25847–25854 (2010).

[135] Sang, B. H. & Jeon, T.-I. Pressure-dependent refractive indices of gases by THz time-domain spectroscopy. *Optics Express* **24**, 29040 (2016).

[136] Cristiani, I., Tediosi, R., Tartara, L. & Degiorgio, V. Dispersive wave generation by solitons in microstructured optical fibers. *Optics Express* **12**, 124 (2004).

[137] Travers, J. C., Grigorova, T. F., Brahms, C. & Belli, F. High-energy pulse self-compression and ultraviolet generation through soliton dynamics in hollow capillary fibres. *Nature Photonics* **13**, 547–554 (2019).

[138] Köttig, F., Tani, F., Travers, J. C. & Russell, P. S. J. Generation of micro-J pulses in the deep UV at MHz repetition rates. *Optica* **4** (2017).

[139] Belli, F., Abdolvand, A., Chang, W., Travers, J. C. & Russell, P. S. J. Vacuum-ultraviolet to infrared supercontinuum in hydrogen-filled photonic crystal fiber. *Optica* **2**, 292–300 (2015).

[140] Quick, M. et al. Photoisomerization dynamics and pathways of trans - And cis -azobenzene in solution from broadband femtosecond spectroscopies and calculations. *Journal of Physical Chemistry B* **118**, 8756–8771 (2014).

[141] Ferreira, F., Chaves, A. J., Peres, N. M. & Ribeiro, R. M. Excitons in hexagonal boron nitride single-layer: A new platform for polaritonics in the ultraviolet. *Journal of the Optical Society of America B* **36**, 674–683 (2019).

[142] Cousin, S. L. et al. Attosecond streaking in the water window: A new regime of attosecond pulse characterization. *Physical Review X* **7**, 1–14 (2017).

[143] Hemmer, M. et al. 2-μm wavelength , high-energy Ho : YLF chirped-pulse amplifier for mid-infrared OPCPA. *Optics Letters* **40**, 451–454 (2015).

[144] Sanchez, D. et al. 7 μm, Ultrafast, Sub-Millijoule-Level Mid-Infrared Optical Parametric Chirped Pulse Amplifier Pumped At 2 μm. *Optica* **3**, 147 (2016).

[145] Heiner, Z., Petrov, V., Steinmeyer, G., J.Vrakking, M. J. & Mero, M. 100-kHz , dual-beam OPA delivering high-quality, 5-cycle angular-dispersion-compensated mid-infrared idler pulses at 3.1 µm. *Optics Express* **26**, 25793–25804 (2018).

[146] Cirmi, G. et al. Novel method for the angular chirp compensation of passively CEP-stable few-cycle pulses. *Optics Express* **28**, 3171 (2020).

[147] Kim, Y., Kim, Y. J., Kim, S. & Kim, S. W. Er-doped fiber comb with enhanced fceo S/N ratio using Tm: Ho-doped fiber. *Optics Express* **17**, 18606–18611 (2010).

[148] Glebov, L. et al. Volume-chirped Bragg gratings: monolithic components for stretching and compression of ultrashort laser pulses. *Optical Engineering* **53**, 051514 (2014).

[149] von Grafenstein, L., Bock, M., Steinmeyer, G., Griebner, U. & Elsaesser, T. Taming chaos: 16 mJ picosecond Ho: YLF regenerative amplifier with 0.7 kHz repetition rate. *Laser and Photonics Reviews* **10**, 123–130 (2016).

[150] von Grafenstein, L., Bock, M., Griebner, U. & Elsaesser, T. High-energy multi-kilohertz Ho-doped regenerative amplifiers around 2 µm. *Optics Express* **23**, 14744 (2015).

[151] Kroetz, P. et al. Overcoming bifurcation instability in high- repetition-rate Ho : YLF regenerative amplifiers. *Optics Letters* **40** (2015).

[152] Koen, W. et al. Compact fibre-laser-pumped Ho : YLF oscillator – amplifier system. *Applied Physics B: Lasers and Optics* **99**, 101–106 (2010).

[153] Walsh, B. M., Grew, G. W. & Barnes, N. P. Energy levels and intensity parameters of Ho^{3+} ions in $GdLiF_4$, $YLiF_4$ and $LuLiF_4$. *Journal of Physics Condensed Matter* **17**, 7643–7665 (2005).

[154] Yin, W. et al. $BaGa_2MQ_6$ (M = Si, Ge; Q = S, Se): A new series of promising IR nonlinear optical materials. *Dalton Transactions* **41**, 5653–5661 (2012).

[155] Badikov, V. V. et al. Crystal growth and characterization of new quaternary chalcogenide nonlinear crystals for the mid-IR: $BaGa_2GeS_6$ and $BaGa_2GeSe_6$. *Optical Materials Express* **6**, 2933 (2016).

[156] Obradors, X. et al. Progress towards all-chemical superconducting $YBa_2Cu_3O_7$-coated conductors. *Superconductor Science and Technology* **19** (2006).

[157] Saxena, A. K. *High-Temperature Superconductors*, vol. 76 (Springer, Berlin, Heidelberg, 2012).

[158] Cairns, G. F. et al. Temperature dependence of the mid-infrared dielectric function of YBCO in the a-b plane: A re-evaluation. *Physica C: Superconductivity and its Applications* **340**, 1–15 (2000).

[159] Farnan, G. A. et al. Dielectric function of YBCO in the mid-infrared: temperature and doping dependence at 3.392 μm. *Physica C: Superconductivity and its Applications* **341-348 (I**, 2273–2274 (2000).

[160] Reiss, H. R. The tunnelling model of laser-induced ionization and its failure at low frequencies. *Journal of Physics B: Atomic, Molecular and Optical Physics* **47** (2014).

[161] Franz, D. et al. All semiconductor enhanced high-harmonic generation from a single nano-structure. *Scientific Reports* **9**, 5663 (2019).

[162] Luu, T. T. & Wörner, H. J. Measurement of the Berry curvature of solids using high-harmonic spectroscopy. *Nature Communications* **9**, 1–6 (2018).

[163] Lanin, A. A., Stepanov, E. A., Fedotov, A. B. & Zheltikov, A. M. Mapping the electron band structure by intraband high-harmonic generation in solids. *Optica* **4**, 516–519 (2017).

[164] Vampa, G. et al. All-Optical Reconstruction of Crystal Band Structure. *Physical Review Letters* **115**, 193603 (2015).

[165] Pennetta, R., Enders, M. T., Frosz, M. H., Tani, F. & Russell, P. S. J. Fabrication and non-destructive characterization of tapered single-ring hollow-core photonic crystal fiber. *APL Photonics* **4** (2019).

[166] Schulte, J., Sartorius, T., Weitenberg, J. & Vernaleken, A. Nonlinear pulse compression in a multi-pass cell. *Optics Letters* **41**, 2–5 (2016).

[167] Beetar, J. E., Gholam-Mirzaei, S. & Chini, M. Spectral broadening and pulse compression of a 400 μJ, 20 W Yb:KGW laser using a multi-plate medium. *Applied Physics Letters* **112**, 0–5 (2018).

[168] Gröbmeyer, S. et al. Self-compression at 1 µm wavelength in all-bulk multi-pass geometry. *Applied Physics B: Lasers and Optics* **126**, 1–6 (2020).

[169] Anand, S., Verma, P., Jain, K. P. & Abbi, S. C. Temperature dependence of optical phonon lifetimes in ZnSe. *Physica B: Condensed Matter* **226**, 331–337 (1996).

[170] Othonos, A. Probing ultrafast carrier and phonon dynamics in semiconductors. *Journal of Applied Physics* **83**, 1789–1830 (1998).

[171] Huang, S. The study of optical characteristic of ZnSe nanocrystal. *Applied Physics B: Lasers and Optics* **84**, 323–326 (2006).

[172] Mandia, A. K., Patnaik, R., Muralidharan, B., Lee, S. C. & Bhattacharjee, S. Ab-initio semi-classical electronic transport in ZnSe: The role of inelastic scattering mechanisms. *Journal of Physics Condensed Matter* **31** (2019).

[173] Mehendale, M., Sivananthan, S. & Schroeder, W. A. Hot electron relaxation dynamics in ZnSe. *Applied Physics Letters* **71**, 1089–1091 (1997).